

RADC-TR-78-7
Final Technical Report
January 1978

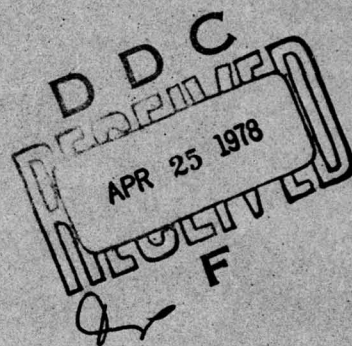
12



8

CHATANAKA MODEL OF THE HIGH-LATITUDE
IONOSPHERE FOR APPLICATION TO
HF PROPAGATION PREDICTION

SRI International



Approved for public release; distribution unlimited.

AD No. _____
DDC FILE COPY

ROME AIR DEVELOPMENT CENTER
AIR FORCE SYSTEMS COMMAND
GRIFFISS AIR FORCE BASE, NEW YORK 13441

This report has been reviewed by the RADC Information Office (OI) and is releasable to the National Technical Information Service (NTIS). At NTIS it will be releasable to the general public, including foreign nations.

APPROVED:

William F. Ring
WILLIAM F. RING
Contract Monitor
Electromagnetic Sciences Division

APPROVED:

Terence J. Elkins
TERENCE J. ELKINS, Acting Chief
Propagation Branch
Electromagnetic Sciences Division

APPROVED:

Allan C. Schell
ALLAN C. SCHELL, Acting Chief
Electromagnetic Sciences Division

FOR THE COMMANDER:

John P. Huss
JOHN P. HUSS
Acting Chief, Plans Office

UNCLASSIFIED

SECURITY CLASSIFICATION OF THIS PAGE (When Data Entered)

19 REPORT DOCUMENTATION PAGE

READ INSTRUCTIONS
BEFORE COMPLETING FORM

1. REPORT NUMBER
RADC-TR-78-7

2. GOVT ACCESSION NO.

3. RECIPIENT'S CATALOG NUMBER

4. TITLE (and Subtitle)

CHATANICA MODEL OF THE HIGH-LATITUDE
IONOSPHERE FOR APPLICATION TO HF PROPAGATION
PREDICTION

5. TYPE OF REPORT & PERIOD COVERED

Final Report

1 Jan

30 Sept 1977

6. PERFORMING ORG. REPORT NUMBER

SRI Project 6056

7. CONTRACT OR GRANT NUMBER(s)

15 F19628-77-C-0102 rev

9. PERFORMING ORGANIZATION NAME AND ADDRESS

SRI International
333 Ravenswood Avenue
Menlo Park, CA 94025

10. PROGRAM ELEMENT, PROJECT, TASK AREA & WORK UNIT NUMBERS

62702F

46001620

11. REPORT DATE

11 Jan 1978

17/16

13. NO. OF PAGES

154

14. MONITORING AGENCY NAME & ADDRESS (if diff. from Controlling Office)

Unclassified

12/158

15a. DECLASSIFICATION/DOWNGRADING SCHEDULE

N/A

16. DISTRIBUTION STATEMENT (of this report)

Approved for public release; distribution unlimited

DDC-120
APR 25 1978
REF ID: A6200
F

17. DISTRIBUTION STATEMENT (of the abstract entered in Block 20, if different from report)

18. SUPPLEMENTARY NOTES

19. KEY WORDS (Continue on reverse side if necessary and identify by block number)

Ionospheric modeling

Auroral absorption

HF propagation

Riometers

Auroral ionosphere

Magnetic indices

Electron density profiles

RADC-POLAR

20. ABSTRACT (Continue on reverse side if necessary and identify by block number)

Electron density measurements made with the incoherent-scatter radar at Chatanika, Alaska have been used to obtain a synoptic model of the high-latitude ionosphere. This Chatanika model is a modification of the RADC-POLAR model developed by Elkins and coworkers for use in raytracing codes for HF propagation prediction. Because the existing RADC model was derived from a larger and more geographically extensive data base than that used in this study, many of its features have been retained in the new model. The major modification that we

DD FORM 1 JAN 73 1473

EDITION OF 1 NOV 65 IS OBSOLETE

UNCLASSIFIED

SECURITY CLASSIFICATION OF THIS PAGE (When Data Entered)

410281

20 ABSTRACT (Continued)

made was an improved specification of the auroral E-layer and the altitude interval between the E and F regions. This region sometimes acts as a duct in which HF signals may travel for great distances without traversing the D region, where most absorption occurs.

The data used in this work consists of 21 sets, each of 24-hours duration, and comprising approximately 5,000 profiles. Data were selected to give a representative distribution with season and geomagnetic activity. An examination of the data showed that, as expected, the ionization could be attributed to two sources: solar photoionization and particle precipitation. The dayside F-region profile appears to be consistent with production by solar ionization. However, the daytime E-region profile is often observed to have a dense E layer that is evidently due to particle precipitation south of the dayside auroral oval. At night the auroral E-layer has spatial and temporal variations characteristic of diffuse and discrete auroral precipitation. Often the electron density decreases monotonically with altitude above the E layer with no indication of an F layer or valley.

From each of the electron density profiles we extracted the fundamental parameters needed to specify the auroral E layer and valley region. A statistical analysis of these parameters was made to determine their characteristic variation with solar-zenith angle and magnetic activity. Solar-zenith angle was chosen as a sorting parameter in order to combine diurnal and seasonal variations into a single index. We found that the profile parameters were only weakly correlated with the planetary geomagnetic index, K_p , and that a significantly stronger correlation exists with the local magnetic index, K . In order to retain K_p as the descriptor of magnetic activity, a relationship was found between the planetary index and the local K values at various latitudes and local times.

To demonstrate the compatibility of the new model with the RADC raytracing code, a number of rays were traced from a point in the northwestern U.S. toward Europe. Rays were launched at the same angles through the unmodified ionospheric model to illustrate the effect of differences between the two versions.

In addition to the model of the refracting regions, a model of auroral absorption was developed for possible incorporation into the RADC code at a later time. This model, developed from previously compiled riometer data, describes the variation of median auroral absorption as a function of corrected geomagnetic latitude, longitude, season, local time, solar activity, and magnetic activity.

EVALUATION

F19628-77-C-0102

1. This is the Final Report on the contract. It describes the analytical work performed to modify the RADC Polar Ionospheric Model on the basis of measurements made with the DNA Project 617 incoherent-scatter radar at Chathanika, Alaska. This radar had the unique capability of measuring the electron density profile in the upper E-region when a local minimum or "valley" is present.
2. The objective of this work was an improved specification of the auroral E-layer and the altitude interval between the E and F regions.
3. This work is valuable because of its application to ducted propagation studies. The altitude interval between the E and F regions sometimes acts as a duct in which High Frequency signals may travel for great distances without returning to earth. Ducted rays are less attenuated than normal modes because they make fewer traversals of the D region, where most of the absorption occurs.
4. The results will be used in ray-tracing calculations to determine probability of ducting for selected paths in the design of long range propagation experiments.

William F. Ring
WILLIAM F. RING
Contract Monitor
Propagation Branch
Electromagnetic Sciences Division

ACCESSION for	White Section <input checked="" type="checkbox"/>
NTIS	Buff Section <input type="checkbox"/>
DDC	<input type="checkbox"/>
UNANNOUNCED	<input type="checkbox"/>
JUSTIFICATION	
BY	
DISTRIBUTION/AVAILABILITY CODES	
MAIL and/or SPECIAL	

AF

CONTENTS

LIST OF ILLUSTRATIONS	5
LIST OF TABLES	9
ACKNOWLEDGEMENTS	10
SUMMARY	11
1. INTRODUCTION	15
2. IONOSPHERIC MEASUREMENTS WITH THE CHATANIKA RADAR	18
2.1 Electron Density Measurements	18
2.2 Data Used in This Study	20
3. MORPHOLOGY OF THE HIGH-LATITUDE IONOSPHERE	23
3.1 Latitudinal Variations Evident in Elevation-Scan Data .	23
3.1.1 Day-Sector Characteristics	25
3.1.2 Evening-Sector Characteristics	30
3.1.3 Midnight-Sector Characteristics	31
3.1.4 Morning-Sector Characteristics	34
3.1.5 Summary of Diurnal Variations Deduced from Elscan Data	36
3.2 Diurnal Variations Evident in Overhead Data	41
4. CHATANIKA MODEL OF THE HIGH-LATITUDE IONOSPHERE	49
4.1 Extraction of Profile Parameters from Chatanika Data .	49
4.2 Variation of Profile Parameters with Solar Zenith Angle and Geomagnetic Activity	51
4.3 Profile Shapes	60
4.4 Latitude and Local-Time Variations of Auroral-E	69
4.5 Comparison of Chatanika Data with Original and Modified Profile Predictions	73
5. SAMPLE RAYTRACINGS THROUGH ORIGINAL AND MODIFIED IONOSPHERES	76
5.1 Dayside Propagation Path	76
5.2 Nightside Propagation Path	79

6. AURORAL ABSORPTION MODEL	83
6.1 Background	83
6.2 Review of Existing Models	85
6.2.1 The Foppiano Model	85
6.2.2 The Hargreaves Model	88
6.2.3 The Basler Model	89
6.3 The SRI Model	90
6.3.1 Definition of Absorbing Regions	90
6.3.2 Conversion from Q_1 to A_m	92
6.3.3 The Magnitude of Absorption as a Function of K_p	94
6.4 Sample Calculations	94
7. CONCLUSIONS	104
APPENDICES	
A TEMPERATURE CORRECTIONS TO CHATANIKI MEASUREMENTS	107
B DIURNAL VARIATION OF HIGH-LATITUDE K FOR VARIOUS K_p RANGES	111
C DETAILED SPECIFICATION OF COMPUTER CODE FOR THE CHATANIKI MODEL	121
REFERENCES	153

ILLUSTRATIONS

2-1	Frequency Distribution of K_p for the Data Set Used in this Study and for the Years 1932 to 1971	22
3-1	College Magnetograms (Horizontal Component Only) Showing Magnetic Activity vs Time for the Three Elscan-Run Days	26
3-2	Contours of Equal Electron Density Measured by the Chatanika Radar Between 2323 UT and 2336 UT on 13 November 1976 (1323 to 1336 local standard time)	27
3-3	Electron Density Profiles Extracted at 40-km Intervals from the Contour Plot in Figure 3-2	28
3-4	Contour Map of Equal Electron Density Made from Chatanika Elevation-Scan Data Taken Around Local Sunset	30
3-5	Isodensity Contour Map of the Evening-Sector Auroral Ionosphere	32
3-6	Isodensity Contour Map of the Midnight-Sector Diffuse Aurora During Non-Substorm Conditions on 13 November 1976 .	33
3-7	Isodensity Contour Map of the Midnight-Sector Diffuse Aurora During Substorm Conditions on 13 November 1976	35
3-8	Isodensity Contour Map of the Morning-Sector Diffuse Aurora During a Recovery Period from Negative-Bay Activity on 13 November 1976	37
3-9	Isodensity Contour Map of the Morning-Sector Diffuse Aurora During a Period of Relatively Weak Magnetic Activity on 13 November 1976	38
3-10	Summary Plot of the 12-13 November 1976 24-Hour Elscan Run. See text for detailed description	39
3-11	College Magnetograms (horizontal component only) Showing Magnetic Activity vs Time for Three Selected 24-Hour Overhead Runs	43
3-12	Electron Density Profiles from ± 15 Minutes About the Hour for Three Overhead 24-Hour Runs	41
3-13	Solar-Zenith-Angle Dependence of the E and F ₁ Layers During Sunset on Two Summer Days	47
4-1	Correlation of the Maximum Electron Density of the Auroral E Layer with Varying Geomagnetic Activity for Solar Zenith Angles of 90-100°	52

4-2	Correlation of the Maximum Electron Density of the Auroral E Layer with Varying Geomagnetic Activity for Solar Zenith Angles $> 100^{\circ}$	53
4-3	Critical Frequency of the Auroral E-Layer, $f_o E_A$, as a Function of K for Various Solar Zenith Angles, χ	59
4-4	Height of the Combined Solar and Auroral E-Layers as a Function of K for Various Solar Zenith Angles, χ	60
4-5	Scatter Plots with Best-Fit Lines for the Valley-One Parameter, $f_o V_1/f_o F_2$, for Various Solar Zenith Angles, χ	61
4-6	Scatter Plots with Best-Fit Lines for Valley-Two Parameter, $f_o V_2/f_o F_2$, for Various Solar Zenith Angles, χ	62
4-7	Ratio of Minimum Plasma Frequency at Valley One to Critical Frequency of F2 Layer, $f_o V_1/f_o F_2$, as a Function of K for Various Solar Zenith Angles, χ	63
4-8	Ratio of Plasma Frequency at Valley-Two Minimums to Critical Frequency of F2 Layer, $f_o V_2/f_o F_2$, as a Function of K for Various Solar Zenith Angles, χ	63
4-9	Ratio of Valley-One Height Above the E-Layer to the Difference in Height Between E and F2 Layers as a Function of K for Various Solar Zenith Angles, χ	64
4-10	Ratio of Valley-Two Height Above the E-Layer to the Difference in Height Between E and F2 Layers as a Function of K for Various Solar Zenith Angles, χ	64
4-11	Comparison of Profiles Generated by the RADC and SRI Models with Actual Chatanika Measurements.	67
4-12	Variation of K with Corrected Geomagnetic Latitude and Corrected Geomagnetic Local Time for a K_p of 3.	70
4-13	Boundaries of the Auroral Oval at Geomagnetic Midnight as Defined in the RADC-POLAR Model and as Determined From ISIS-2 Data.	72
4-14	Comparison of Chatanika Data with Model Predictions on 17 March 1976	74
5-1	Polar View of Northern Hemisphere with Selected Propagation Path.	77
5-2	Ionospheric Contours of Local Plasma Frequency (MHz) Generated by the RADC Model for the Selected Propagation Path at 1800 UT, a Sunspot Number of 50, and a K_p of 2.	78
5-3	Ionospheric Contours of Local Plasma Frequency (MHz) Generated by the SRI Model for the Selected Propagation Path at 1800 UT, a Sunspot Number of 50, and a K_p of 2.	78
5-4	Propagation Path in Figure 5-1 Plotted in Coordinates of Corrected Geomagnetic Latitude and Local Time	80

A-1	Altitude Profiles of Ion and Electron Temperatures for Various Solar and Auroral Conditions.	109
A-2	Ratios of Actual and Uncorrected Electron Densities at Two Altitudes for Various Solar and Geophysical Conditions.	110
B-1	Variation of K with Corrected Geomagnetic Latitude and Corrected Geomagnetic Local Time for a K_p of 1.	116
B-2	Variation of K with Corrected Geomagnetic Latitude and Corrected Geomagnetic Local Time for a K_p of 2.	117
B-3	Variation of K with Corrected Geomagnetic Latitude and Corrected Geomagnetic Local Time for a K_p of 3.	118
B-4	Variation of K with Corrected Geomagnetic Latitude and Corrected Geomagnetic Local Time for a K_p of 4.	119
B-5	Variation of K with Corrected Geomagnetic Latitude and Corrected Geomagnetic Local Time for a K_p of 5.	120
C-1	Flowchart of the SRI Modifications to SUBPOLR, the Ionosphere Generator in RADC-POLAR.	123
C-2	Listing of Subroutines Used in SRI Modification of the RADC-POLAR Ionosphere Generator	124

TABLES

2-1 Chatanika Data Used in This Study.	21
3-1 Elevation-Scan Data Summary.	25
3-2 Overhead Data Summary.	42
4-1 Correlation of Ionospheric Parameters with K_p for Five Ranges of Solar Zenith Angle, χ	55
4-2 Correlation of Ionospheric Parameters with K for Five Ranges of Solar Zenith Angle, χ	56
4-3 Slopes and Intercepts for Linear Fits to Ionospheric Parameters for Five Ranges of Solar Zenith Angle, χ	57
6-1 Riometer Stations Used in the Hargreaves Model	88
B-1 Observatories Whose Data Are Used in the Compilation of K_p	113
B-2 Stations Used in Deriving the Temporal Relationship of K for a Given K_p	115

ACKNOWLEDGMENTS

We are grateful to Mr. William Ring and Dr. Kurt Toman of RADC for useful guidance and helpful suggestions concerning this work. We wish to thank Karin Woomer, Barbara Phillips, Dorothy Hendricks, and Noro Rudy for valuable assistance in the data analysis portion of this study.

Dr. John Kelly of SRI International and Dr. J. S. Murphree of the University of Calgary provided us with experimental data prior to its publication. We are also grateful to them for valuable discussions concerning this work. Magnetic data used in this study were obtained from the World Data Center (WDC-A), Boulder, CO.

SUMMARY

The ability to predict the propagation of HF radio waves along transauroral paths requires a model of the spatial distribution of electron density in the high-latitude ionosphere. An empirical mean model has been developed by Elkins and coworkers (Elkins and Rush, 1973) and is referred to as the RADC-POLAR model. This model has been used by RADC and others for predictive studies with three-dimensional raytracing programs.

An ionospheric region of particular interest for transauroral propagation is the altitude interval between the E and F regions. This region sometimes acts as a duct in which HF signals may travel for great distances without returning to earth. The presence of a "valley", or local minimum above the E layer, is favorable (but not essential) for ducted propagation. Rays that are ducted will be less attenuated than normal modes because they make fewer traversals of the D region, where most of the absorption occurs. Such propagation modes are especially important during magnetically disturbed periods, when auroral absorption can completely obliterate an HF signal.

The RADC-POLAR model is based primarily on ground-based and satellite-borne vertical-incidence ionosonde data that do not measure the density profile in the upper E-region when a valley is present. However, complete profiles of electron density, from the lower E region to well above the F-region peak, can be measured by an incoherent-scatter radar. The purpose of our study was to analyze measurements by the DNA Project 617 incoherent-scatter radar at Chatanika, Alaska, and to extract a synoptic model that describes the characteristic variations of ionization at auroral latitudes.

Because the existing RADC model was derived from a larger and more geographically extensive data base than that used in this study, many of its features have been retained in the new model. The major modification that we sought was an improved specification of the auroral E layer and the valley above it.

The data used in this work consisted of 21 sets, each of 24-hours duration, and comprising approximately 5,000 profiles. Data were selected to give a representative distribution with season and geomagnetic activity. Two types of data were used: elevation scans in the magnetic meridian plane, and near-vertical measurements over Chatanika. When the radar is operated in an elevation-scan mode, it measures the distribution of ionization in both altitude and latitude with a spatial resolution of 10 km over a horizontal extent of more than 600 km. Two days of such data were examined in order to obtain a qualitative description of the diurnal morphology of the high-latitude ionosphere. The remainder of the data consisted of electron density profiles in the region nearly overhead of Chatanika.

An examination of the elevation-scan data showed that, as expected, the ionization could be attributed to two sources: solar photoionization and particle precipitation. The dayside F-region profile appears to be consistent with production by solar ionization. However, the daytime E-region profile is often observed to have a dense E layer that is evidently due to particle precipitation south of the dayside auroral oval. At night the auroral E-layer has spatial and temporal variations characteristic of diffuse and discrete auroral precipitation. Often the electron density decreases monotonically with altitude above the E layer with no indication of an F layer or valley.

From each of the electron density profiles we extracted the fundamental parameters used in the RADC-POLAR model to derive the model profiles. Among these parameters are the height and maximum density of the auroral-E layer, the height and minimum density in the valley (if present) above the E-region peak, and the height, density, and semi-thickness of the F1 and F2 layers. A statistical analysis of these

parameters was made to determine their characteristic variation with solar zenith angle and magnetic activity. Solar zenith angle was chosen as a sorting parameter in order to combine diurnal and seasonal variations into a single index.

The results of this statistical analysis were used to modify the RADC-POLAR model. The modifications were made so as to be compatible with the present predictive model, which defines auroral features as functions of the planetary geomagnetic index K_p . We found that the profile parameters were only weakly correlated with K_p and that a significantly stronger correlation exists with the local magnetic index, K . Since we wanted to retain K_p as the descriptor of magnetic activity, a relationship was sought between the planetary index and the local K values at various latitudes and local times. A meaningful relationship was derived from geomagnetic data obtained over an entire year at 16 high-latitude stations. Incorporation of this relationship into the model increased the spatial and temporal structure within the auroral oval. Other modifications that were made to the RADC-POLAR model include the addition of four new profile shapes, an increase in the size of the nightside oval, the provision for particle-produced ionization on the dayside south of the auroral oval, and a reduction in the electron density of the midlatitude auroral E-layer.

Our analysis is similar to that used in the development of the RADC-POLAR model, in that both produce statistical mean models. We did not model small-scale (<100 km) structures or phenomena that were transient on a time-scale smaller than the 3-hour K_p index. As a result the features in our model are characteristic of persistent, widespread phenomena, such as the diffuse aurora and the dayside "drizzle" zones. Features such as auroral arcs, the diffuse aurora "boundary feature," and auroral substorms are not included. However, the use of a local K that varies with latitude and local time for a specified K_p did result in an auroral ionospheric model with more structure than that in the original model and, presumably, a more realistic one.

To demonstrate the compatibility of the new model with the RADC raytracing code, a number of rays were traced from a point in the northwestern U.S. toward Europe. Rays were launched at the same angles through the unmodified ionospheric model to illustrate the effect of differences between the two versions.

In addition to the model of the refracting regions, a model of auroral absorption was developed for possible incorporation into the RADC code at a later time. This model, developed from previously compiled riometer data, describes the variation of median auroral absorption as a function of corrected geomagnetic latitude, longitude, season, local time, solar activity, and magnetic activity.

The primary end product of our work is the modified ionospheric model. The major components of it are listed in Appendix C, and a complete operating program is being sent to RADC separate from this report.

1. INTRODUCTION

The ability to predict the propagation of HF radio waves along transauroral paths requires a model of the spatial distribution of electron density in the high-latitude ionosphere. For this purpose, Elkins and coworkers (Elkins and Rush, 1973) developed a model referred to as the RADC-1976-POLAR ionosphere. This report describes modifications to that model recommended by SRI on the basis of measurements made with the incoherent-scatter radar at Chathanika, Alaska.

An ionospheric feature of particular interest for transauroral propagation is the altitude interval between the E and F regions. This region sometimes acts as a duct in which HF signals may travel for great distances without returning to earth. Ducted signals will be relatively unattenuated because they make fewer traversals of the D region, where most of the absorption occurs. Such modes are especially important during magnetically disturbed periods, when auroral absorption can completely obliterate an HF signal as it traverses the disturbed D region.

The RADC-POLAR model is based primarily on ionosonde data (both ground-based and satellite-borne) that do not measure the density profile in the upper E region when a local minimum, or "valley", is present. In order to determine accurately the electron density there, it is necessary to use rocket-borne instrumentation or an incoherent-scatter radar. The purpose of this study is to analyze measurements by the incoherent-scatter radar at Chathanika, Alaska, so as to describe the characteristic variation of electron density at auroral latitudes.

The data used in this study consisted of 21 sets, each of 24-hours duration, and comprising approximately 5,000 electron density profiles. Data were selected to give a representative distribution of season and magnetic activity. Two types of data were used. Data in an elevation

scan mode provided information about the distribution of electron density with both altitude and latitude. These data were examined in order to obtain a qualitative description of the morphology of the high-latitude ionosphere. The remainder of the data (approximately 90% of the total) were measurements of electron density profiles restricted to the region nearly overhead of Chatanika.

From each of the electron density profiles we extracted the parameters required in the RADC-POLAR model to specify the high-latitude ionosphere. A statistical analysis of these parameters was made to determine their characteristic variation with solar zenith angle and magnetic activity. The results of this analysis were used to modify the RADC-POLAR model.

As demonstrations of the use of the modified ionospheric model, raytracing calculations were made along a particular propagation path. Raytracings were also made through the unmodified ionospheric model as illustrations of the effect of differences between the two versions.

In addition to the model of ionospheric electron density, we also developed a model of auroral absorption. Previously compiled riometer data were used to synthesize a description of the variation of auroral absorption with latitude, local time, and magnetic activity.

The report is organized in the following way. Section 2 describes the Chatanika radar and its measurements of electron density. Then we specify the data base used in this study and the rationale for its selection. In Section 3 representative examples of these data are shown, together with a description of the morphology of the high-latitude ionosphere. The extraction of profile parameters and their statistical variations are presented in Section 4. There we also explain the modifications that were made to the RADC-POLAR model, and then compare the predictions of the models to actual Chatanika data. Examples of raytracings through the model ionospheres are presented in Section 5. The auroral absorption model is described in Section 6 and the conclusions

of our study are given in Section 7. Appendices A through C describe temperature corrections for Chatanika electron density measurements, the relationship between K_p and local K , and the actual modifications to the RADC-POLAR software.

2. IONOSPHERIC MEASUREMENTS WITH THE CHATANIKA RADAR

The electron density profiles used in this study are based on measurements made with the Defense Nuclear Agency Project 617 incoherent-scatter radar at Chatanika, Alaska. This radar, generally referred to as simply the Chatanika radar, has been operated in Alaska by SRI since June 1971 and is the only incoherent-scatter radar at a high latitude. The geographical location of the radar is 65.1°N , 145.5°W , corresponding to a geomagnetic location of 64.9°N , 103.3°W and an L of 5.7.

The radar transmits a high-power (typically 3.5 MW) pulse of UHF (1290 MHz) electromagnetic radiation and the backscattered signal from the ionosphere is analyzed for both amplitude and frequency distribution. This information is then used to compute the electron density, electron and ion temperature, plasma drift, and other derivable parameters such as the ionospheric electric field, conductivity, current, and neutral wind. The Chatanika radar and associated data-analysis techniques have been described in a number of publications (Leadabrand et al., 1972; Baron, 1974, 1977; Wickwar, 1975). In this report we will describe only the techniques used to measure the spatial variation of electron density and the Chatanika data set used in this study.

2.1 Electron Density Measurements

Incoherent scatter is basically a technique for measuring ionospheric electron concentrations and other parameters by using a ground-based radar facility. Electrons in the ionosphere, when excited by a UHF radio wave, will backscatter a small amount of energy. The amount of energy scattered is proportional to the radar cross section of a single electron and the number of electrons present in the scattering volume (defined by the radar beam and the transmitted pulse length). By measuring the back-scattered power, one is able to calculate the electron number density.

The electron density is normally computed by assuming that the electron cross section is equal to the classical Thomson cross section. This result is generally not exact because the radar cross section of the electrons is not a constant; due to plasma interactions it is a function of the electron and ion kinetic temperatures, and to a smaller extent, a function of the ratio of the Debye length to the operating wavelength (Evans, 1969). The effect of neglecting this correction factor that accounts for plasma interactions is to always underestimate the true electron density. This correction factor is generally negligible in the E-region (< 150 km altitude). At higher altitudes the correction often can be a factor of 2 or more. However, because the correction factor is generally slowly varying with altitude there is only a small distortion in the shape of the electron density profile in the upper E and lower F region. The effect of the plasma correction factor is discussed in more detail in Appendix A.

Measurements of E- and F-region electron densities at Chatanika are normally done using short (40 to 67 μ s) transmitted pulses with 192 receiver range gates. The pulse length results in a spatial range resolution of 6 to 10 km. These data are processed with signal integration periods of 1 s or more, the choice being dependent on the magnitude of the electron densities and the dynamic character of the medium.

Because of its altitude resolution of 6 to 10 km, the Chatanika radar is unable to detect structures of smaller scale size that may be responsible for sporadic E. Although sporadic E is important to HF propagation, we made no attempt to include it in the model.

The Chatanika radar has a high-gain antenna with a 3-dB beamwidth of 0.5° . As a result, when the antenna is held stationary the horizontal spatial resolution in the E region is approximately 1 km. Because the antenna is fully steerable, a variety of antenna operating modes are employed. In order to obtain vector estimates of plasma drift, measurements are made at several pointing directions. Generally, the radar

is pointed at some elevation, typically 60° to 70° , and then is either scanned in azimuth or sequentially pointed to three separate azimuths. About six minutes are required for each cycle. For the purpose of this study, measurements in this mode are referred to as overhead data because the horizontal separation from Chatanika is less than 100 km.

An alternative mode of operation is to scan the radar mechanically in elevation with the azimuth fixed in the geomagnetic meridian (Vondrak and Baron, 1976). Such a scan results in the determination of the latitudinal variation of measured quantities. The elevation-scan data used in this study were slow scans from the northern horizon to the southern horizon, covering a range in geomagnetic latitude of 62° to 68° in the E region and 56° to 73° in the F region. Each scan required approximately 15 minutes, and a 15-s integration time was used for each density measurement.

2.2 Data Used in This Study

This study is based on the analysis of 21 data sets. Each data set covers an interval of approximately 24 hours, so that each represents a continuous measurement at all local times. Two complete days of elevation-scan data were used. Because they were the only existing 24-hour runs of elevation-scan data at the time the study began, the description of auroral morphology in Section 3 is supplemented by a 10-hour run on 19 February 1976. In addition, 19 runs in the overhead mode were used. Because the radar sensitivity and data quality have been continually upgraded in recent years, data sets were chosen from the time interval of 1974 to 1977. The data are listed in Table 2-1 according to year and season. A primary criterion used in data selection was to have data representative of all seasons and levels of magnetic activity. As can be seen in Table 2-1, seven data sets are for summer, five data sets are for winter, and nine data sets are for equinox (including spring and fall). The distribution, with respect to magnetic activity, of the data selected for this study is shown in Figure 2-1. K_p is an index of the amount of global magnetic activity during a 3-hour

Table 2-1

CHATANIKA DATA USED IN THIS STUDY

Season	1974		1975		1976	
	Date	Time, UT	Date	Time, UT	Date	Time, UT
Spring	13 Feb	0430 - 1930	12 Mar	0400 - 2500	17 Mar	0030 - 2410
	20 Mar	0000 - 2400				
					14 Apr	0030 - 2350
Summer			15 Apr	0130 - 1100		
			14 May	0230 - 2400	12 May	0000 - 2330
					23 Jun	0000 - 2400
					14 Jul	0000 - 2400
Fall			17 Jul	0820 - 2400	11 Aug	0000 - 2330
			13 Aug	0000 - 2400		
Winter			17 Sep	0000 - 2350	20 Oct	0010 - 2400
			15 Oct	0500 - 2450		
			17 Dec	0140 - 2500	17 Nov	0730 - 2410
					22 Dec	0020 - 2350
					13 Nov*	0000 - 2400
					17 Dec*	0000 - 2400

*Elevation-scan data

interval. For comparison, also indicated in Figure 2-1 is the occurrence frequency distribution of K_p during the period of 1932 to 1971 as given by Cage and Zawalick (1972). It can be seen that the data selected for this study have been chosen to represent reasonably well the distribution normally occurring. As a result we would expect that the model based on these data would have the minimum statistical error for conditions occurring most frequently.

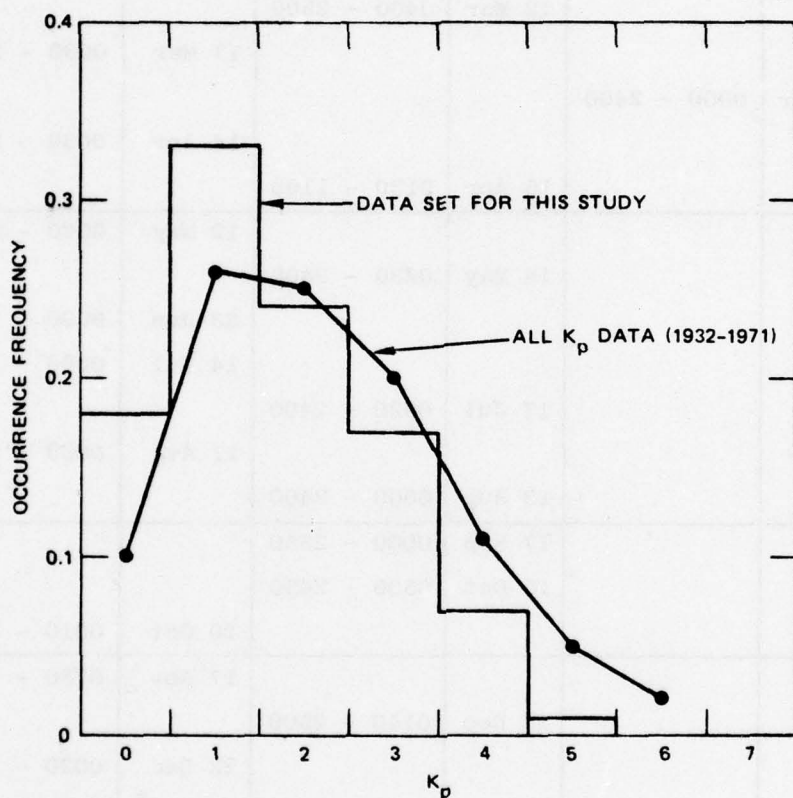


FIGURE 2-1 FREQUENCY DISTRIBUTION OF K_p FOR THE DATA SET USED IN THIS STUDY AND FOR THE YEARS 1932 TO 1971

3. MORPHOLOGY OF THE HIGH-LATITUDE IONOSPHERE

In this section we describe the morphology of the high-latitude ionosphere on the basis of Chatanika incoherent-scatter radar data. Elevation-scan (or elscan) data, which contain electron-density-profile information as a function of both latitude and local time, are used to identify major features of the auroral ionosphere and to detect any latitudinal gradients in ionization. Because the elscan data base is so limited, we supplement it with overhead radar measurements that we used to examine seasonal and diurnal variations.

The characteristics of the auroral E region are clearly evident in the data presented here. Examination of the data indicated that the auroral (particle produced) F layer is not as predictable as the auroral E region. With the data base available for this study, a substantial F_2 layer was found to be present at night only infrequently. The solar-controlled F layer dominated during the day. Consequently, our understanding of the occurrence of a valley region in the dark sector is limited by the unpredictable nature of the particle-produced auroral F_2 layer.

It should again be noted that the electron densities presented here have not been corrected for either the temperature ratio or the Debye-length parameter. The net result is always to underestimate the true electron density, particularly in the F region. The effects of neglecting the altitude-dependent correction factor are discussed in Appendix A.

3.1 Latitudinal Variations Evident in Elevation-Scan Data

Elscan data are ideal for use as a basis of constructing a morphological description of the auroral ionosphere. They can be used to construct contour maps of electron density in coordinates of altitude and latitude, which immediately reveal various latitudinal boundaries in

auroral ionospheric structure. In the E region, these boundaries include those of the discrete and diffuse aurora. These boundaries can be related to any F-region feature, such as the trough region. In addition to their use in locating latitudinal boundaries, the contour maps may be used to extract any latitudinal gradients that may exist in the peak electron density and its altitude. By collecting elscan data continuously over a 24-hour period, variations in the above characteristics can be determined as a function of local time and magnetic activity.

A description of high-latitude morphology from these data has two principal limitations. First, an elscan with the Chatanika radar intersects the E-region ionosphere from 62° to 68° geomagnetic latitude, or a latitudinal extent of 6° . Consequently, we can characterize the aurora only when it is located within the scanned region. Second, the morphological description presented in this section is based on only three data sets, two of which were continuous 24-hour runs. Clearly, much more data must be examined under a variety of conditions before all the major features can be identified.

The elscan data used to construct the preliminary model are summarized in Table 3-1. They consist of two continuous 24-hour runs, each beginning and ending near local noon (2200 UT), and a "partial" run that started in the afternoon and ended shortly after local midnight (1000 UT). All except the December 1976 data set were taken during moderately active geomagnetic conditions (i.e., the K_p index averaged a value of 4 during the entire data-gathering period).

The local geomagnetic conditions that prevailed during the three days of interest can be inferred from the horizontal perturbation (H) component of the geomagnetic field measured at College, Alaska, as shown in Figure 3-1. The magnitude of the perturbations can be estimated from the magnetograms by measuring the deviation of the traces from the horizontal line that represents the ambient level of the geomagnetic field.

Table 3-1
ELEVATION SCAN DATA SUMMARY

Date (UT)	Start Time (UT)	Stop Time (UT)	ΣK_p
12-13 Nov 1976	2230	2230	33
16-17 Dec 1976	2200	2200*	17+
19 Feb 1976	0030	1045	31-

* Not in elscan mode from 0950 to 1120 UT

A qualitative feeling for the differing degrees of magnetic activity during the three days can be seen by comparing the magnetograms in Figure 3-1. The December magnetogram is virtually a straight line, indicating essentially no magnetic activity until around 1500 UT when a 200- γ negative bay occurred. In contrast, the November magnetogram shows continuous activity throughout the 24-hour period shown, with nearly 100- γ positive bay activity from 2300 to 0600 UT, and a major negative bay ($\sim 1300 \gamma$) starting around 1030 UT. The February magnetogram shows conditions that are somewhat less disturbed than those shown in the November magnetogram. There was virtually no positive-bay activity until 0500 UT. The largest negative-bay activity, which commenced around 1200 UT, was weaker than the major bay in the November magnetogram and occurred after 1045 UT, the end of Chatanika radar data collection.

In the following subsections, we discuss characteristics of the elscan data from four different time sectors: day, evening, midnight, and morning. Each time sector, as defined here, can be thought of as a time period (of about 6 hours duration) centered approximately around 1200, 1800, 0000, and 0600 magnetic local times (MLT).

3.1.1 Day-Sector Characteristics

Day-sector characteristics of electron density variations with altitude and latitude are illustrated in Figure 3-2. The contour plot

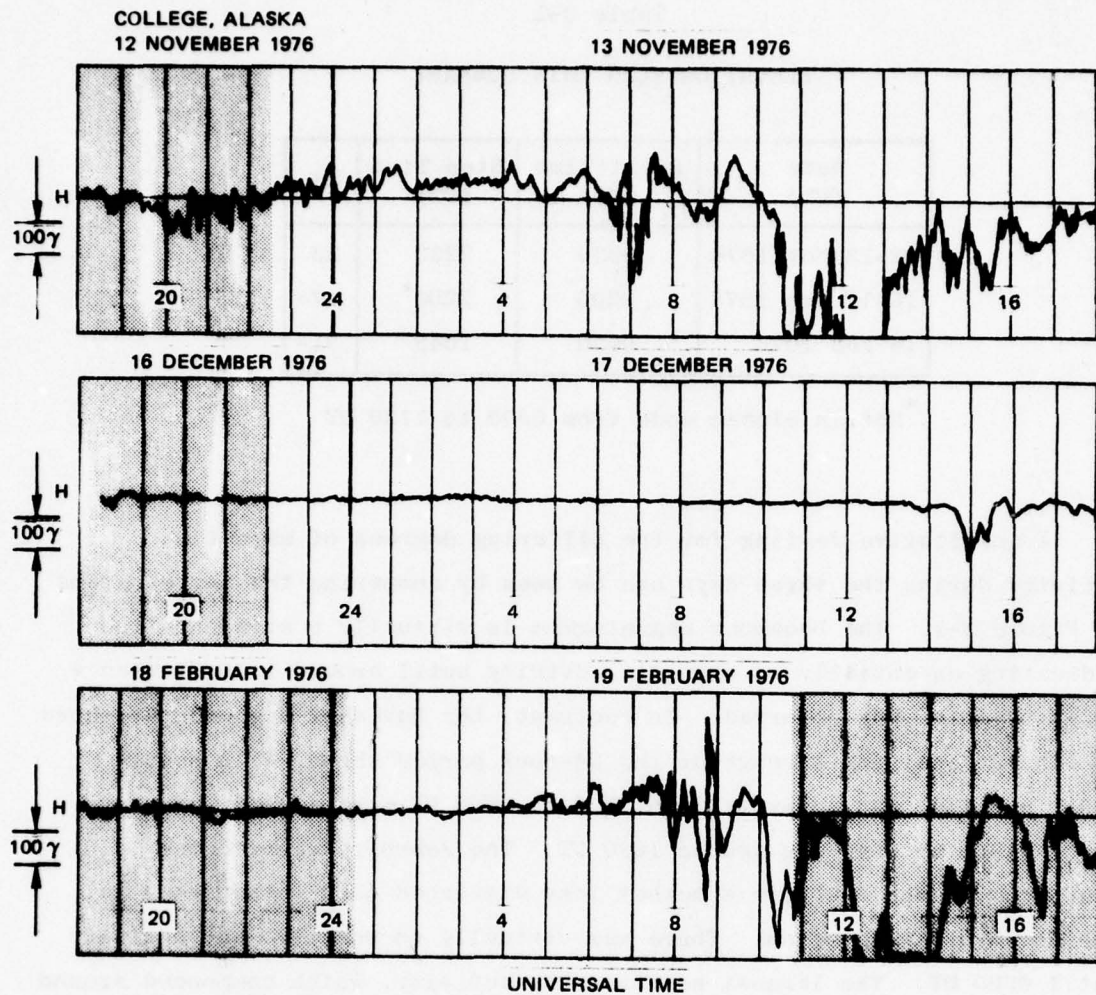


FIGURE 3-1 COLLEGE MAGNETOGRAMS (horizontal component only) SHOWING MAGNETIC ACTIVITY vs TIME FOR THE THREE ELSCAN-RUN DAYS. The unshaded portions of the magnetograms correspond to times when elevation-scan data were collected.

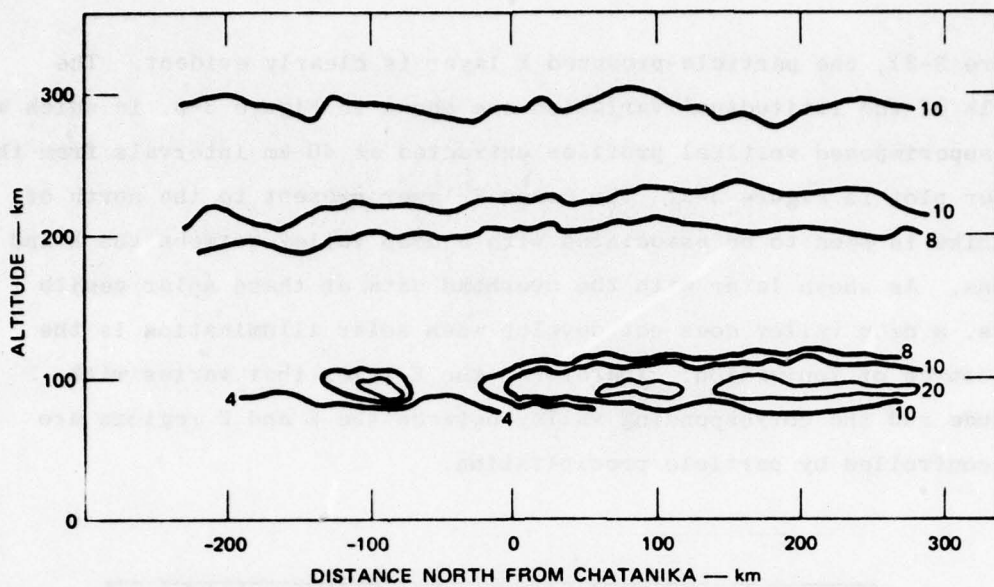


FIGURE 3-2 CONTOURS OF EQUAL ELECTRON DENSITY MEASURED BY THE CHATANICA RADAR BETWEEN 2323 UT AND 2336 UT ON 13 NOVEMBER 1976 (1323 to 1336 local standard time). Contours are in units of $10^4/\text{cm}^3$.

was constructed from elscan data collected around magnetic noon on 13 November 1976 when the solar zenith angle over Chatanika was 86° . The geomagnetic K_p index was 4+.

Under quiet geomagnetic conditions, the day sector is primarily characterized by an electron density distribution that is controlled by solar radiation. As is well known, and as illustrated in Figure 3-2, under these conditions the ionosphere is vertically stratified (except around sunset and sunrise) with a deterministic electron density profile that is closely related to the solar zenith angle. In Section 3.2, the solar control of the electron density profile will be discussed in detail using overhead data.

When there is geomagnetic activity, an E layer produced by particle precipitation often develops. The extent to which the solar-produced electron density profile is modified by the precipitation source depends on the prevailing solar zenith angle. In the example shown

(Figure 3-2), the particle-produced E layer is clearly evident. The details of the latitudinal variation are shown in Figure 3-3, in which we have superimposed vertical profiles extracted at 40-km intervals from the contour plot in Figure 3-2. The dense E layer present to the north of Chatanika is seen to be associated with a deep valley between the E and F regions. As shown later with the overhead data at these solar zenith angles, a deep valley does not develop when solar illumination is the only source of ionization. Therefore, the E layer that varies with latitude and the corresponding valley between the E and F regions are both controlled by particle precipitation.

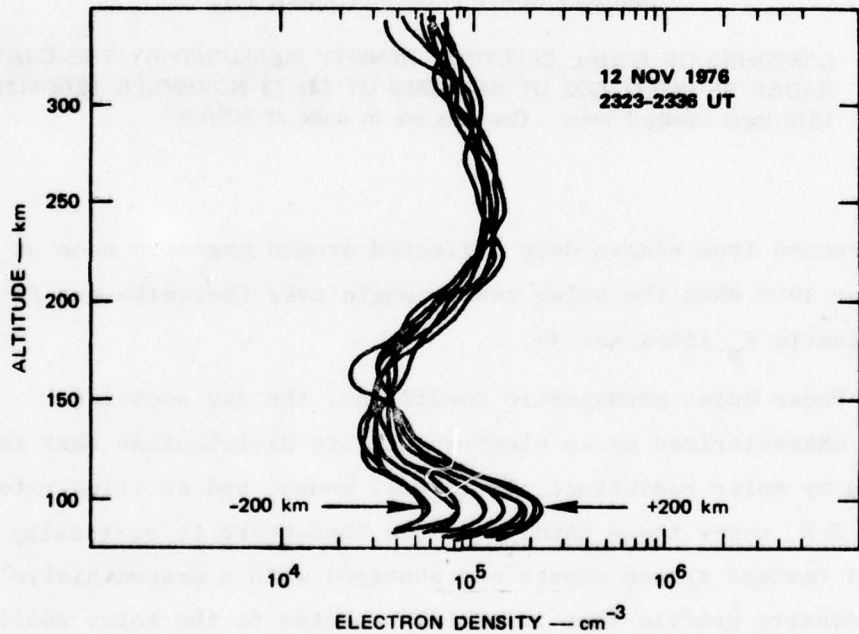
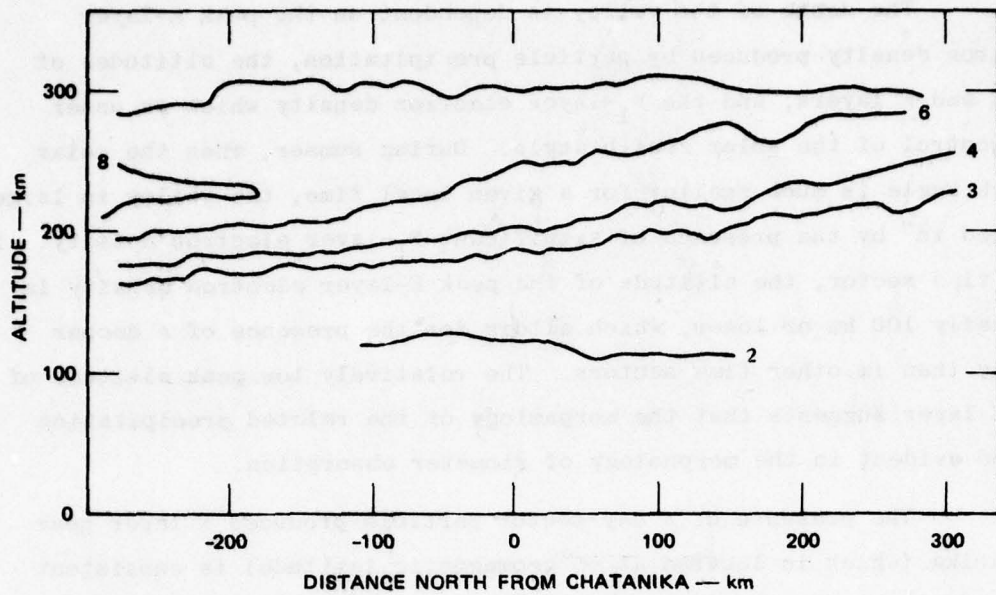


FIGURE 3-3 ELECTRON DENSITY PROFILES EXTRACTED AT 40-km INTERVALS FROM THE CONTOUR PLOT IN FIGURE 3-2

The depth of the valley is dependent on the peak E-layer electron density produced by particle precipitation, the altitudes of the E and F layers, and the F_1 -layer electron density which is under the control of the solar zenith angle. During summer, when the solar zenith angle is much smaller for a given local time, the valley is largely "filled in" by the presence of significant F_1 -layer electron density. In this time sector, the altitude of the peak E-layer electron density is typically 100 km or lower, which allows for the presence of a deeper valley than in other time sectors. The relatively low peak altitude of the E layer suggests that the morphology of the related precipitation may be evident in the morphology of riometer absorption.

The presence of a day-sector particle-produced E layer near Chatanika (which is located at 65° geomagnetic latitude) is consistent with the findings of other workers. Piddington (1965) and Hartz and Brice (1967) organized a large body of data related to particle precipitation and concluded that there are two zones of auroral particle precipitation. One essentially coincides with the auroral oval that contains the visual aurora and is far poleward of Chatanika during the day. The other is a ring of precipitation centered at 65° geomagnetic latitude, independent of local time. Hartz and Brice (1967) found that the occurrence maximum for the second zone (their "drizzle" zone) was around 0800 MLT. The "drizzle zone" precipitation has also been reported from all-sky-camera observations (Davis, 1962) and ISIS-2 scanning photometer observations (Lui et al., 1973). It is responsible for one of the characteristic diurnal maxima in auroral absorption, as discussed in Section 6.

The only occasion when large latitudinal gradients are observed in the dayside F region is at sunset and sunrise. Data taken during an elevation scan at local sunset at Chatanika are shown in Figure 3-4. At this time the sun has set in the north but is still illuminating the F region at more southerly latitudes. The effects of sunset are very apparent. In the north the maximum electron density has decreased and the isodensity contours are tilted upward as the lower F-region erodes



19 FEB 1976
0221-0236 UT

FIGURE 3-4 CONTOUR MAP OF EQUAL ELECTRON DENSITY MADE FROM CHATANICA ELEVATION-SCAN DATA TAKEN AROUND LOCAL SUNSET. A sunlit F region is seen to the south of Chatanika while the post-sunset decay of the F region is evident to the north.

due to faster recombination at lower altitudes. In the south the sun is still illuminating the ionosphere and the F-region is horizontally stratified similar to the sunlit ionosphere shown in Figure 3-2.

3.1.2 Evening-Sector Characteristics

A contour plot of electron density representative of the evening sector is shown in Figure 3-5. The data set was taken around 1930 ML on 19 February 1976 when the solar zenith angle at Chatanika was 117°. Since the solar-controlled E layer is negligible for solar zenith angles greater than 90° (see Watt, 1973; and next section), the electron density distribution shown in Figure 3-5 is due solely to particle precipitation. The geomagnetic K_p index was 4.

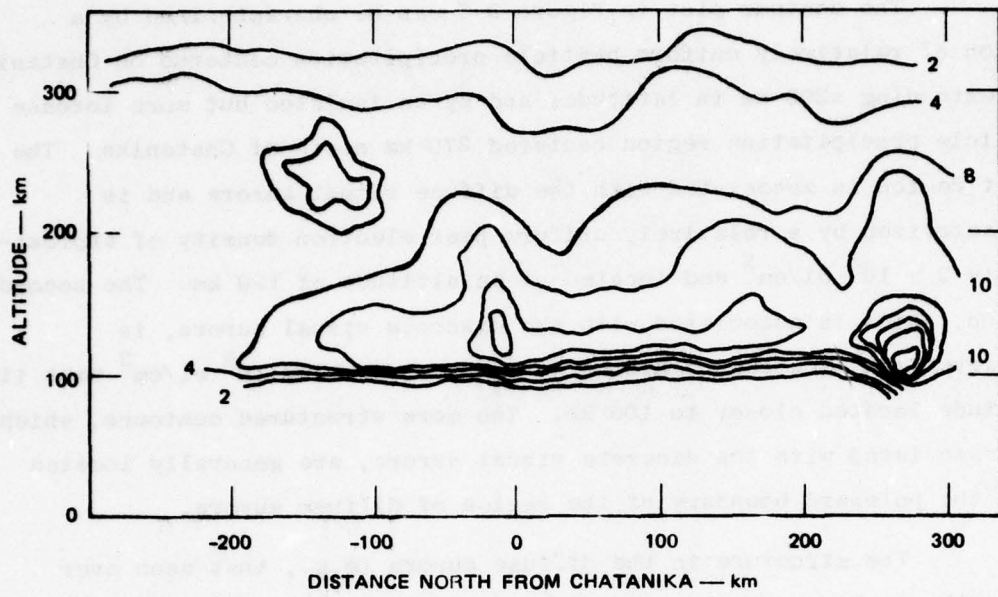
The contour plot in Figure 3-5 can be characterized by a region of relatively uniform particle precipitation centered on Chatanika and extending ± 200 km in latitude, and by an isolated but more intense particle precipitation region centered 270 km north of Chatanika. The first region is associated with the diffuse visual aurora and is characterized by a relatively uniform peak electron density of approximately 2×10^5 el/cm³ and located at an altitude of 120 km. The second region, which is associated with the discrete visual aurora, is characterized by a peak electron density approaching 10^6 el/cm³ with its altitude located closer to 105 km. The more structured contours, which are associated with the discrete visual aurora, are generally located near the poleward boundary of the region of diffuse aurora.

The structure in the diffuse aurora (e.g., that seen over Chatanika in Figure 3-5) is probably related to substorm activity. During less disturbed periods, the topside of the E layer is often very uniform, similar in character to that shown in Figure 3-2.

The F-region electron densities in Figure 3-5 are much smaller than those in the auroral E layer. This feature appears to be representative of the evening sector, as well as the remaining dark sector (see following sections). The decrease in electron density with altitude is usually monotonic so that no valley is present. The only conspicuous evening F-region feature is an enhancement occasionally found at the equatorial edge of the diffuse aurora. Such an enhancement is visible in Figure 3-5 at a distance of 150 km south of Chatanika. This enhancement, referred to as the "boundary feature," is generally transient in nature, persisting for typically 30 minutes.

3.1.3 Midnight-Sector Characteristics

The characteristics of the latitudinal distribution of electron density in the midnight sector are not unlike those seen in the evening sector. The latitudinal distribution is, however, much more complex and dynamic in nature, a behavior directly related to substorm effects. In the evening sector, virtually the only substorm effects are those that



19 FEB 1976
0857-0712 UT

FIGURE 3-5 ISODENSITY CONTOUR MAP OF THE EVENING-SECTOR AURORAL IONOSPHERE. The auroral E layer over Chatanika corresponds to the diffuse aurora, and the localized structure at 270 km north of Chatanika corresponds to the discrete aurora. The F-region boundary feature is seen near the equatorward boundary of the diffuse aurora.

propagate from the midnight sector, behind the westward-traveling surge. These effects are usually contained along the poleward boundary of the diffuse aurora. In the midnight sector, the diffuse aurora appears to be directly related to the substorm process that originates there.

A contour plot illustrating the E-layer electron density distribution with latitude in the midnight sector is shown in Figure 3-6. The data were collected around 2230 MLT on 13 November 1976, when the solar zenith angle was 132° . Referring to Figure 3-1, we see that the magnetic H component had just returned to the quiescent level from positive-bay activity. While these data should not be interpreted as data representative of quiet times, they may be interpreted as representative of non-substorm conditions.

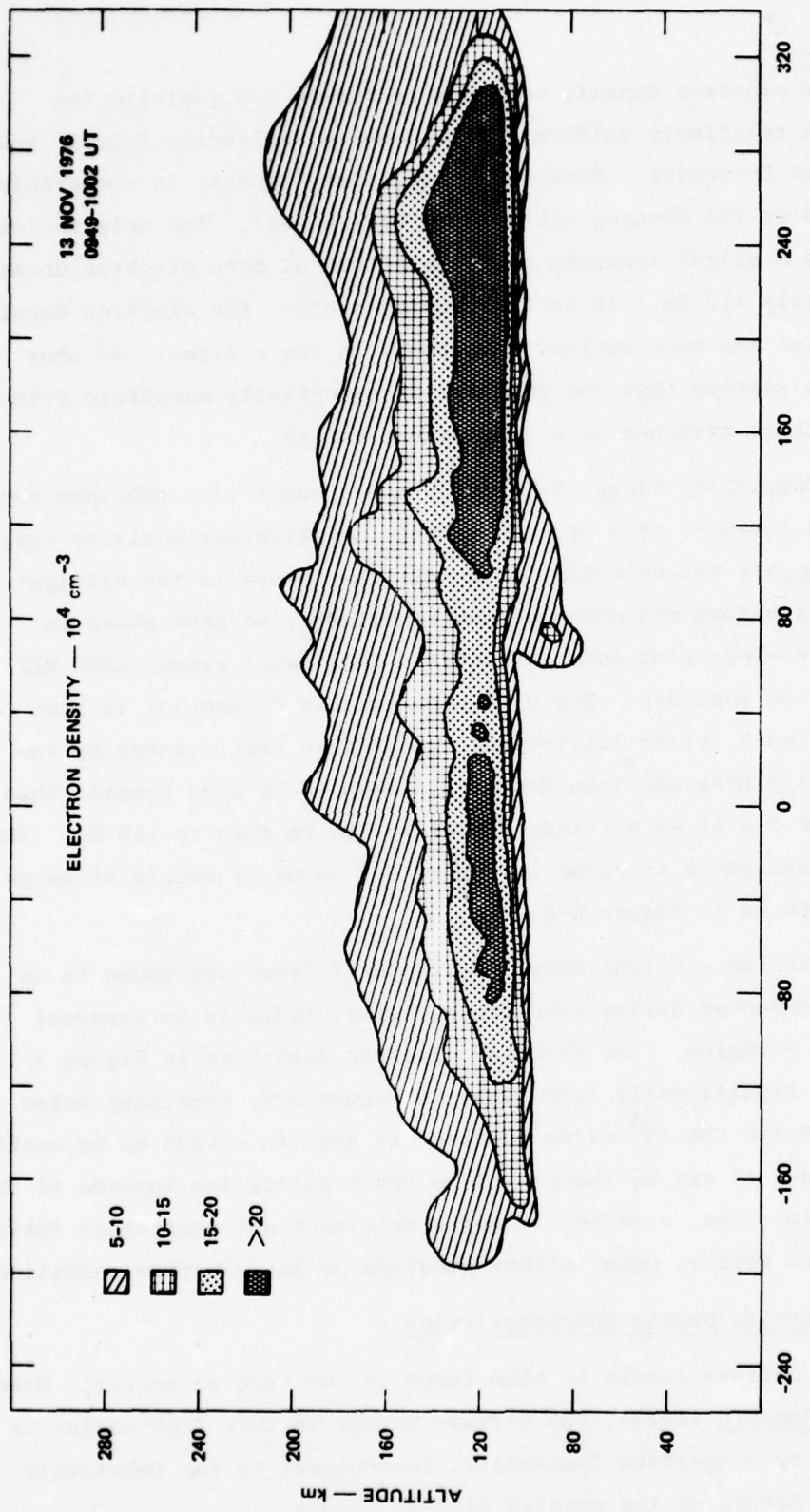


FIGURE 3-6 ISODENSITY CONTOUR MAP OF THE MIDNIGHT-SECTOR DIFFUSE AURORA DURING NON-SUBSTORM CONDITIONS ON 13 NOVEMBER 1976

The electron density contours in Figure 3-6 indicate the presence of a relatively uniform diffuse aurora, extending from 1° south to 3° north of Chathanika. Peak E-layer electron density is comparable to that found in the evening sector (see Figure 3-5). The only noticeable difference is a slight lowering of the altitude of peak electron density to approximately 115 km. As in the evening sector, the electron densities in the F region are much smaller than those in the E layer. We show later in this section that the decrease is essentially monotonic with altitude, with no evidence of a significant valley.

Referring to Figure 3-1, we note the onset of a substorm around 1030 UT on 13 November 1976 with continuous negative-bay activity thereafter. To compare the behavior of the diffuse aurora in the midnight sector under substorm and non-substorm conditions, we have shown in Figure 3-7 a contour plot constructed from data taken around 2330 MLT (1100 UT) on the same day. The diffuse aurora in Figure 3-7 is seen to extend over a much larger latitudinal extent than that scanned by the radar (6). The peak electron density is seen to be much greater than that in Figure 3-6 at an altitude closer to 100 km than to 115 km. The base of the ionosphere is found in Figure 3-7 to be at nearly 80 km as compared to 100 km in Figure 3-6.

While the electron densities in the E layer are found to be considerably enhanced during substorm activity, there is no apparent change in the F region. The F-region electron densities in Figure 3-7 do not differ significantly from those in Figure 3-6, remaining below 10^5 el/cm^3 . While the 10^5 el/cm^3 contour is seen to extend up to nearly 230 km altitude, it may be thought of as representing the topside of the E layer. In any case, a valley is not a prominent nor persistent feature in the midnight sector, under either substorm or non-substorm conditions.

3.1.4 Morning-Sector Characteristics

The diffuse aurora is also found in the morning sector. However, according to Akasofu (1977), the diffuse aurora in this time sector is characterized by nonuniform luminosity, in contrast to the relatively structureless nature of the evening diffuse aurora.

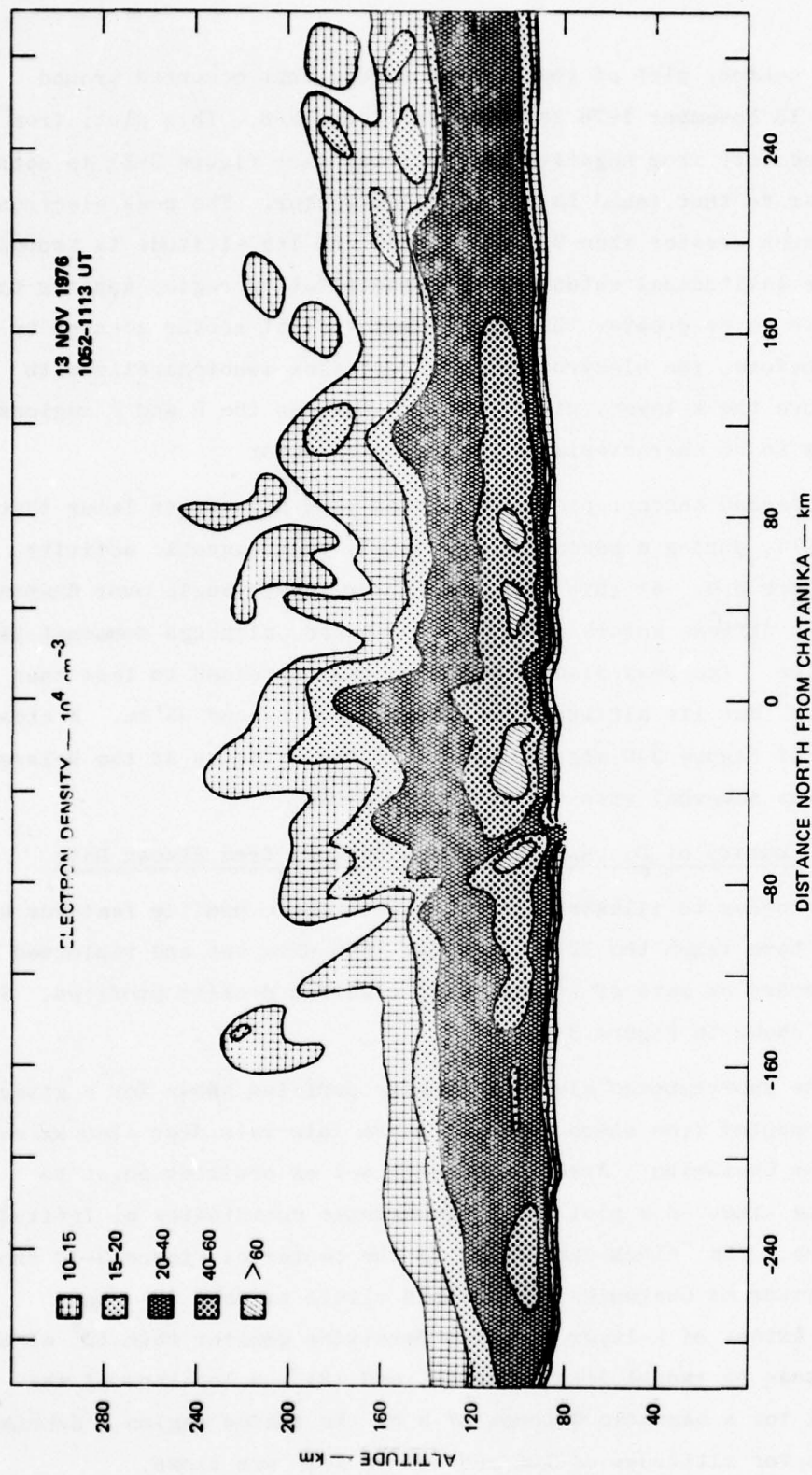


FIGURE 3-7 ISODENSITY CONTOUR MAP OF THE MIDNIGHT-SECTOR DIFFUSE AURORA DURING SUBSTORM CONDITIONS ON 13 NOVEMBER 1976

A contour plot of the diffuse aurora that occurred around 0320 MLT on 13 November 1976 is shown in Figure 3-8. This plot, from a period of recovery from negative-bay activity (see Figure 3-1), is seen to be similar to that found in the midnight sector. The peak electron density is much greater than 2×10^5 el/cm³ and its altitude is around 100 km. The latitudinal extent of the precipitation region appears to be comparable to or greater than the 6° latitudinal sector scanned by the radar. As before, the electron density decreases monotonically with altitude above the E layer, with no valley between the E and F regions. This appears to be characteristic of the dark sector.

A second contour plot constructed from data taken later that day (0555 MLT), during a period of relatively weak magnetic activity, is shown in Figure 3-9. At this time, the solar zenith angle over Chatanika was 95°. The diffuse aurora is still widespread, although somewhat patchy over Chatanika. The peak electron density has decreased to less than 2×10^5 el/cm³ but its altitude has decreased to around 95 km. A close examination of Figure 3-9 also reveals that the altitude of the E-layer peak increases somewhat with decreasing latitude.

3.1.5 Summary of Diurnal Variations Deduced from Elscan Data

In order to illustrate the characteristic profile features more clearly, we have taken the 12-13 November 1976 data set and replotted selected elscans as sets of superimposed electron density profiles. The results are shown in Figure 3-10.

The superimposed electron density profiles shown for a given time were computed from elscan data at 40-km intervals over ± 240 km extent centered over Chatanika. Arrows from each set of profiles point to corresponding times on a plot using geomagnetic coordinates of latitude vs local time. The "clock dial" plot in the center of Figure 3-10 shows (1) the latitude of Chatanika by a dashed circle at 65°, (2) the latitudinal extent of E-layer electron densities greater than 10^5 el/cm³ for each elscan by radial line segments, and (3) the location of the auroral oval for a magnetic Q index of 5 by the shaded region. Sunrise-sunset lines for altitudes of 100 and 300 km also are shown.

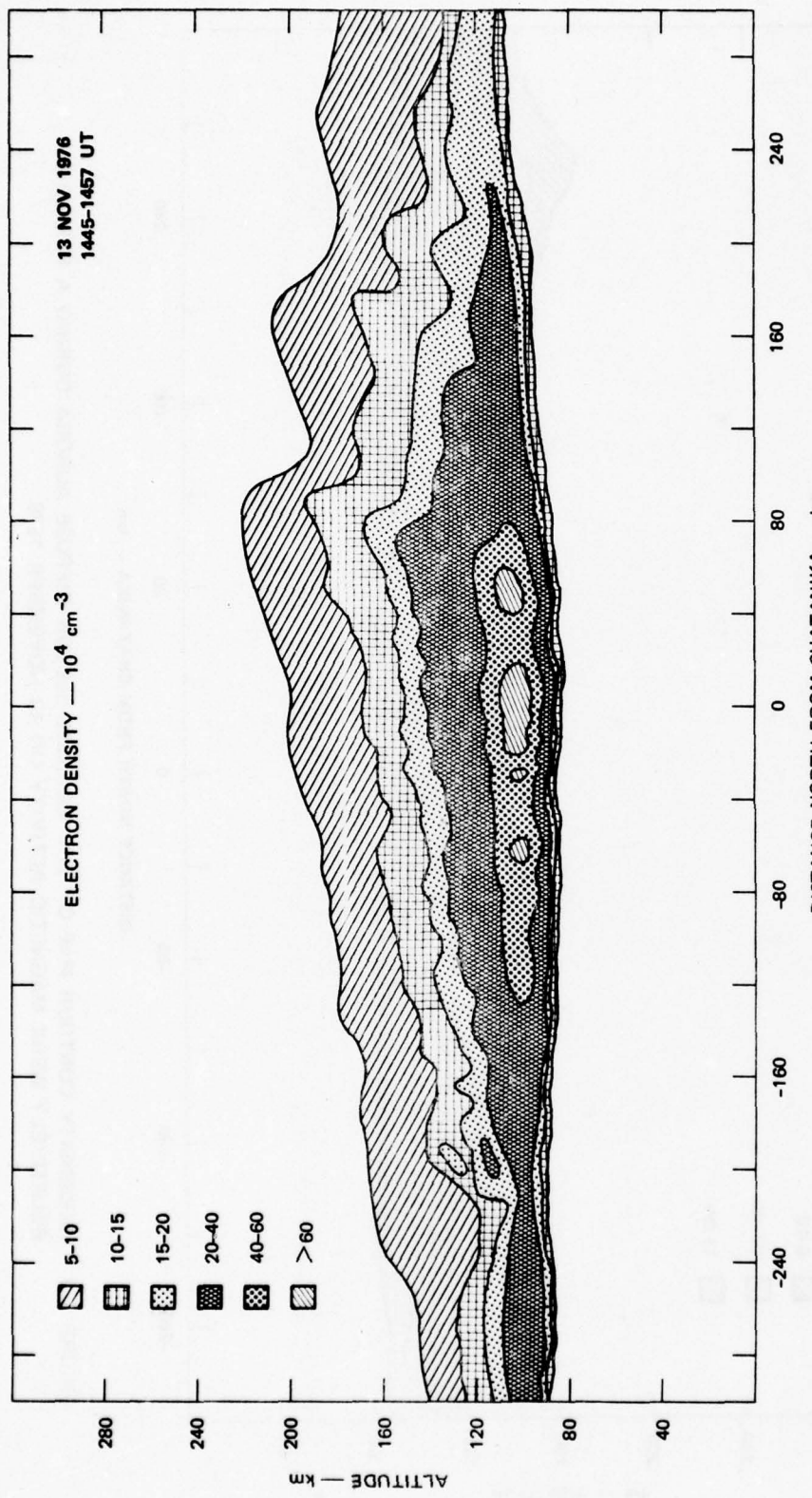


FIGURE 3-8 ISODENSITY CONTOUR MAP OF THE MORNING-SECTOR DIFFUSE AURORA DURING A RECOVERY PERIOD FROM NEGATIVE-BAY ACTIVITY ON 13 NOVEMBER 1976

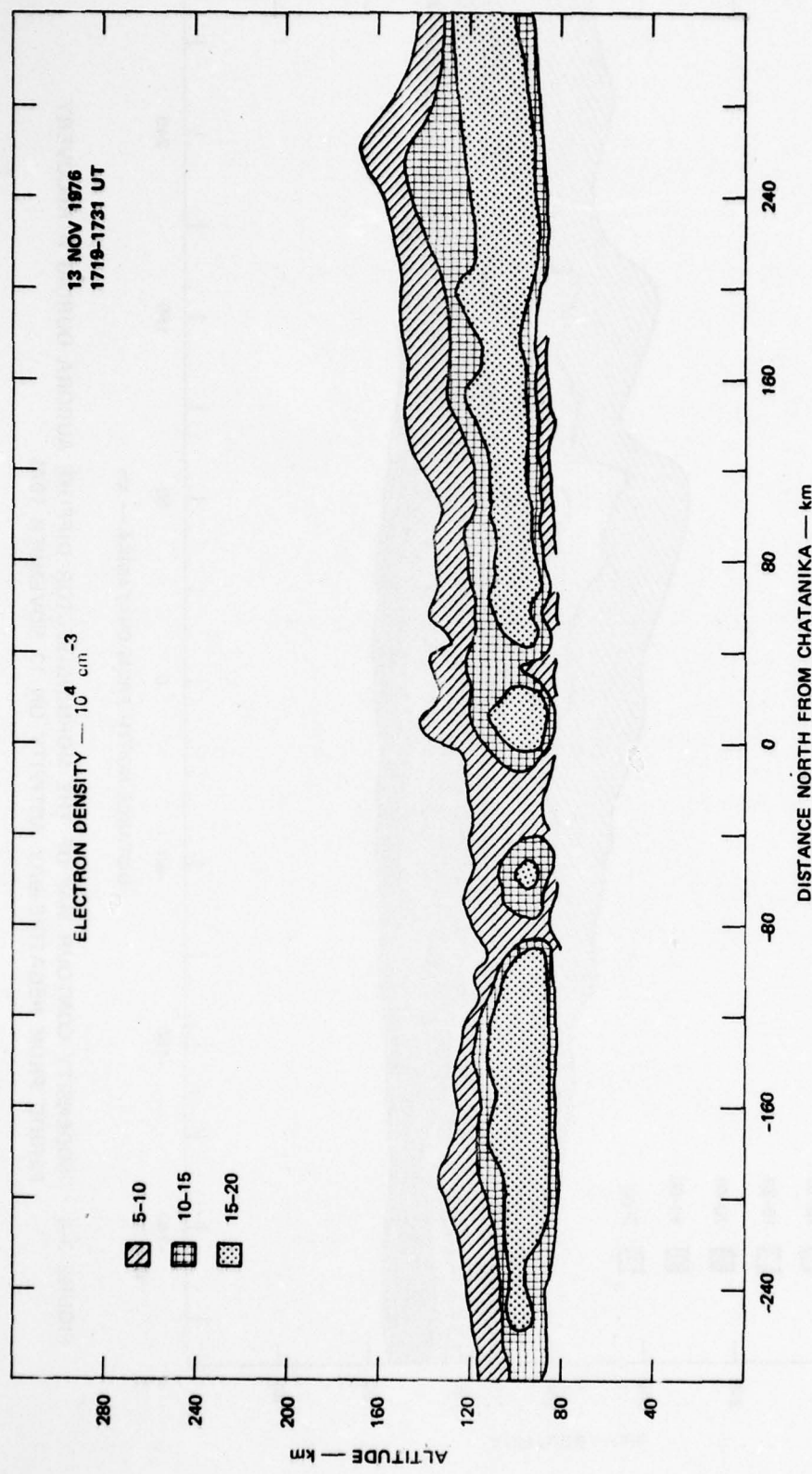


FIGURE 3-9 ISODENSITY CONTOUR MAP OF THE MORNING-SECTOR DIFFUSE AURORA DURING A PERIOD OF RELATIVELY WEAK MAGNETIC ACTIVITY ON 13 NOVEMBER 1976

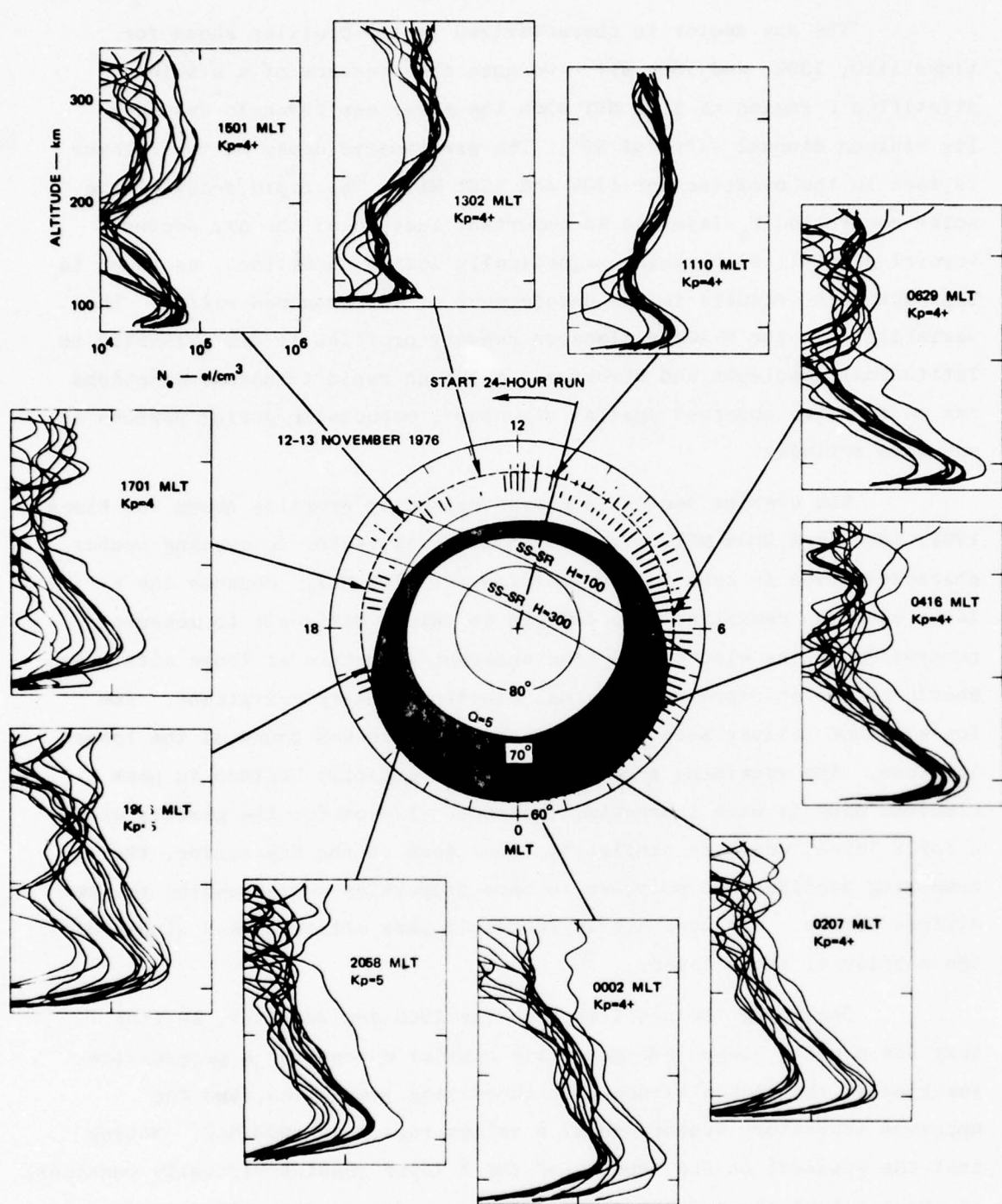


FIGURE 3-10 SUMMARY PLOT OF THE 12-13 NOVEMBER 1976 24-HOUR ELSCAN RUN.
See text for detailed description.

The day sector is characterized by the profiles shown for times 1110, 1302, and 1501 MLT. We note the presence of a stable stratified F region at 1110 MLT when the solar zenith angle was near its minimum diurnal value of 83° . The progressive decay of the F layer is seen in the profiles for 1302 and 1501 MLT. The rapid decay of the solar-controlled F_1 layer is an important feature of the day sector. Auroral precipitation during magnetically active conditions, as shown in this data set, results in the development of a pronounced valley. The variability in the E-layer electron density profiles is due primarily to latitudinal gradients and structure, although rapid temporal variations can confuse the observed spatial structure, especially during periods of substorm activity.

The evening sector is characterized by profiles shown for times 1701, 1906, and 2058 MLT. Transition from day sector to evening sector characteristics is seen in the profiles for 1701 MLT. Because the F-layer electron densities have decayed to values difficult to measure accurately in the elscan mode, the apparent structure at those altitudes should not be interpreted as actual electron density variations. The low-altitude E layer seen in one of the profiles was found at the lowest latitude. The remaining profiles show a progressive buildup in peak electron density with increasing latitude. Except for the profile with a low E layer, which is similar to those seen in the day sector, the remaining profiles can be shown to have properties corresponding to the diffuse aurora. All have nearly identical peak altitudes and slopes of the topside of the E layer.

Examining the profiles from the 1906 and 2058 MLT, we find that the profile shapes are generally similar except for a progressive lowering of the peak altitude with increasing local time, and the apparent transitory appearance of a valley region at 1906 MLT. Noting that the gradient on the topside of the E layer remains virtually constant, it appears that the existence of a valley region is directly dependent on the development of a significant F_2 layer. If the electron density profiles above the E layer observed around 1906 MLT are due to particle precipitation, the incoming particles may have a non-monotonic energy spectrum.

The midnight-sector characteristics, illustrated by the profiles for 0002 MLT, do not appear to differ much from the profiles from the evening sector. There is a tendency for the topside slope to flatten around 200 km altitude, suggesting some enhancement in the F region. However, examination of the other elscans did not reveal a persistent F layer. The two profiles with the greatest peak electron densities occurred at the two extremes (north and south) of the latitudinal scan. Both appear to be associated with discrete visual aurora.

The morning-sector characteristics are illustrated by profiles from 0207, 0416, and 0629 MLT. Perhaps the most apparent feature in the profiles from this sector is the relatively large peak electron density of the E layer with steeper topside slope than in other time sectors. As mentioned previously, the E-layer peak altitude is much lower than that in the evening and midnight sectors. Another characteristic of the morning E layer is the lowering of the peak altitude with decreasing latitude, as seen in the profiles from 0207 MLT. Again, there is an absence of a persistent F layer, and therefore no valley region. The appearance of a valley is seen in the 0629 MLT profiles with the development of a sunlit F_2 layer.

3.2 Diurnal Variations Evident in Overhead Data

The elevation-scan data shown in the preceding section are all from the winter season. In this section we will assess the deterministic characteristics of the solar-controlled electron density profile by showing overhead data from other seasons.

We have selected three 24-hour runs as examples. These data sets are summarized in Table 3-2. The data sets were selected primarily because of the relatively quiet magnetic conditions that prevailed over each 24-hour period. Quiet conditions were desired so that solar control of the ionospheric layers could be determined with a minimum amount of contamination by particle precipitation.

Table 3-2
OVERHEAD DATA SUMMARY

Date (UT)	Start Time (UT)	Stop Time (UT)	ΣK_p
23 June 1976	0100	2400	8+
17 December 1975	0200	2400	16-
17 March 1976	0100	2400	27-

Figure 3-11 shows the magnetograms of the horizontal component of the geomagnetic field as measured at College during the three days of interest. We note that the magnetic perturbations on summer and winter days are comparable, and very similar to that presented in the previous section for the 17 December 1976 elscan data set. The magnetogram for the equinox example (17 March 1976) is seen to be more active than the other two, and similar to the magnetic conditions that existed during the 19 February 1976 elscan data set (see Figure 3-1).

The electron density profiles from the three 24-hour runs are presented in Figure 3-12. Each row contains approximately one-half of the entire data set for that day. For each hour, six individual profiles are superimposed. Each represents a five-minute average taken within 15 minutes of the hour. The solar zenith angle and K_p index for each hour are also shown. In collecting the data, the radar was operated in a three-position discrete-azimuth scan with a fixed elevation angle of 76.5° . Therefore, some of the variability in the slopes of the superimposed profiles is due to horizontal gradients and structure in the ionosphere.

Let us consider first the behavior of the summer ionosphere above Chatanika over a 24-hour period. On 23 June 1976, the solar zenith angle was always less than 91° . Therefore, the F_2 region was always sunlit. The profiles, starting at 0100 UT (1500 LT), are seen to have a very regular shape which persists until 0500 UT when the effects of

COLLEGE, ALASKA
22 JUNE 1976

23 JUNE 1976

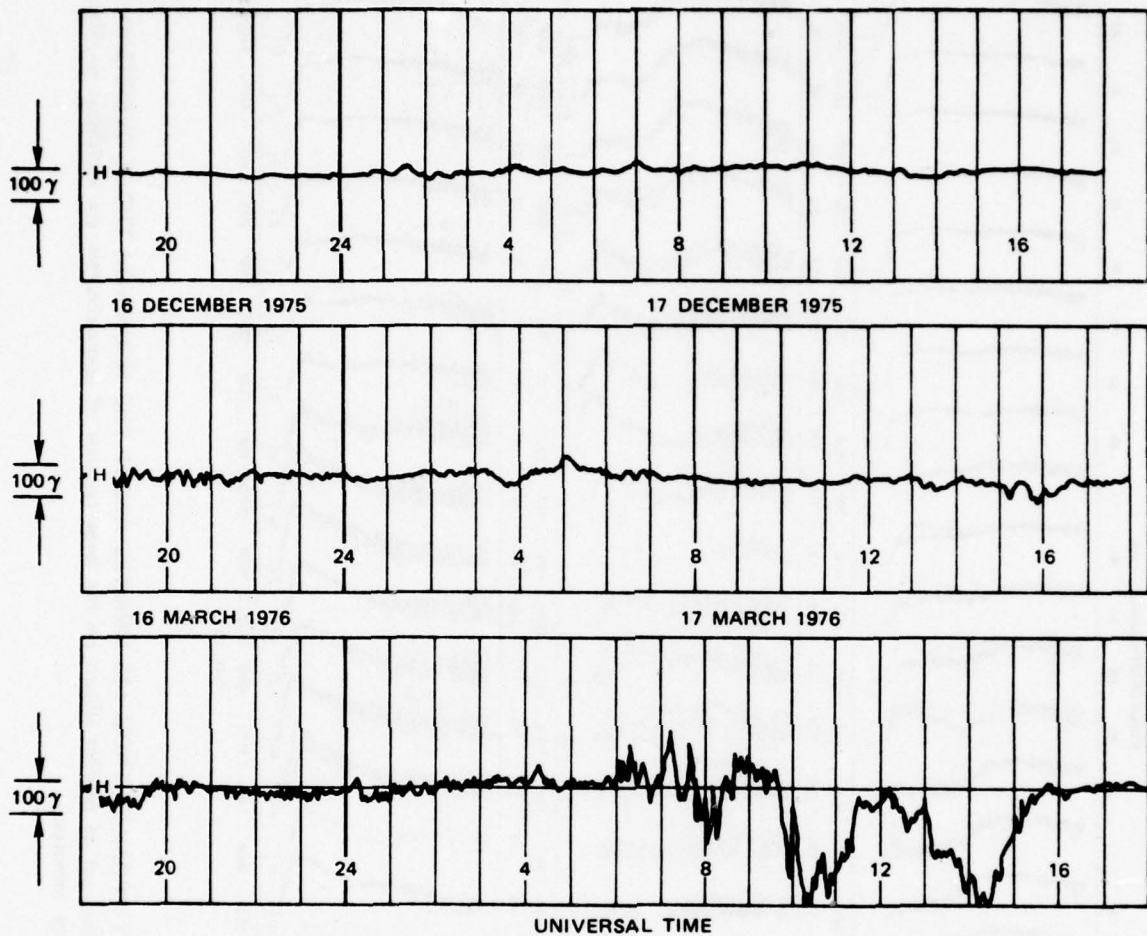


FIGURE 3-11 COLLEGE MAGNETOGRAMS (horizontal component only) SHOWING MAGNETIC ACTIVITY vs TIME FOR THREE SELECTED 24-HOUR OVERHEAD RUNS

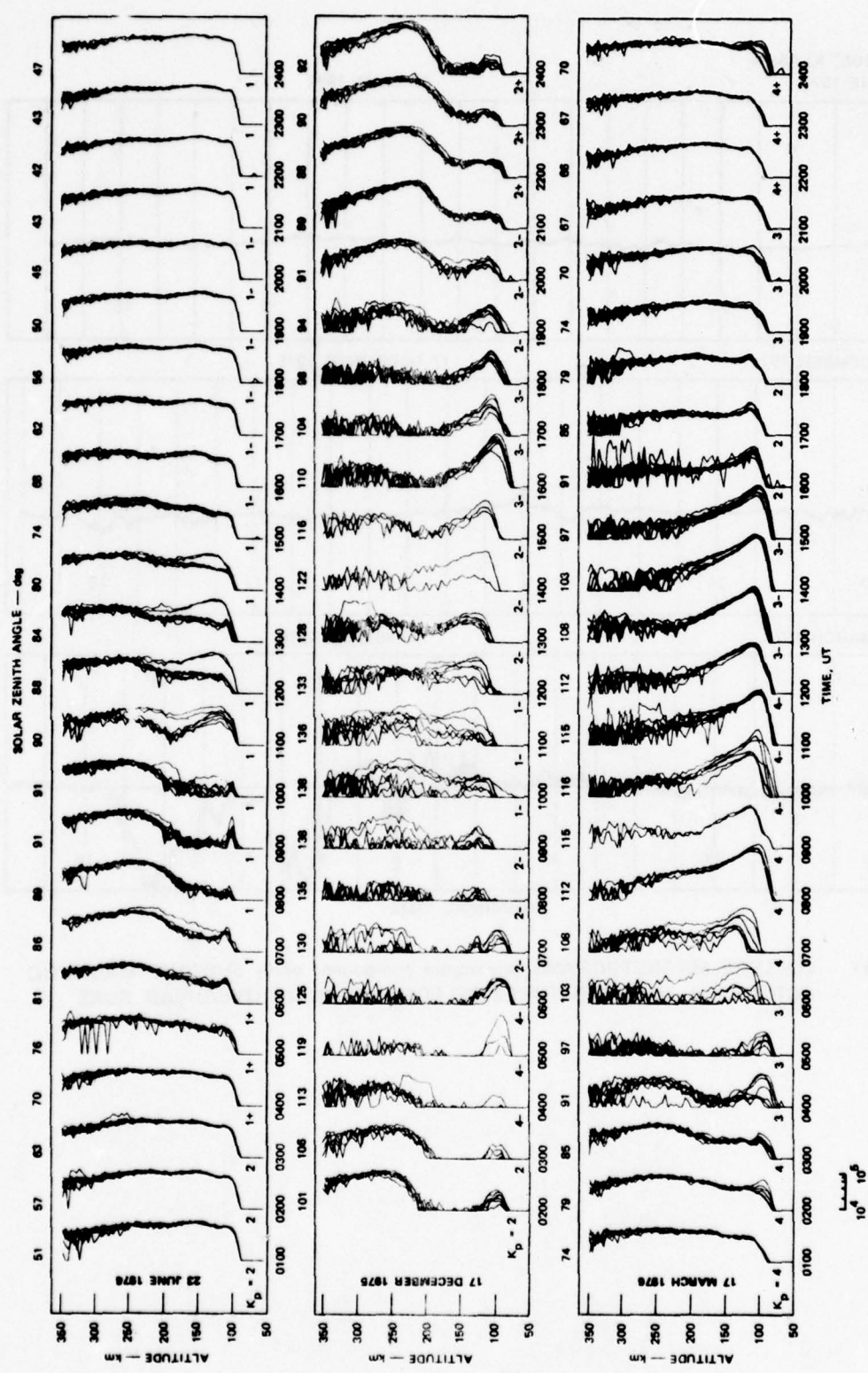


FIGURE 3-12 ELECTRON DENSITY PROFILES FROM ± 15 MINUTES ABOUT THE HOUR FOR THREE OVERHEAD 24-HOUR RUNS. Each set of profiles shown on the hour consists of approximately six individual profiles, each averaged over five minutes.

sunset in the E and F_1 region began. The decay of the two ionospheric layers is complete by 1000 UT. In the local midnight and early-morning sectors, we see the only evidence of a particle-produced E layer. A valley appears only around 1100 UT when the solar zenith angle is greatest (and hence, corresponds to a time when the F_1 electron density is minimum). From 1200 UT on, we see the sunrise effects in the E and F_1 regions. The period between 1200 and 1400 UT contains nighttime profiles without an auroral E layer slightly south of Chatanika, and profiles with a superimposed auroral E layer slightly north of Chatanika. This indicates that the equatorward boundary of the diffuse aurora was centered over Chatanika. By 1500 UT, the diffuse aurora had moved poleward and we see electron density profiles controlled by solar illumination. The profiles from 1600 UT to 2400 UT are essentially replicas of the first profile shown at 0100 UT.

We can now compare the diurnal variations of a quiet summer ionosphere to those of a quiet winter ionosphere, shown in the second row of Figure 3-12. The winter profiles around 0200 UT display a well behaved F_2 layer and a low-altitude auroral E layer. If we scan the summer and winter profiles (first and second rows in Figure 3-12) for similar F-layer shapes, we find that the solar zenith angles are similar. The major difference is a slightly larger peak F_2 -layer electron density during the winter. The winter auroral E layer is similar to that seen at the same local time and season under more disturbed magnetic conditions (see Figure 3-10). The decay of the F_2 layer with increasing solar zenith angle is seen to occur between 0300 and 0500 UT. There is evidence in the profiles around 0700 UT that a measurable F_2 layer, one that is not solar-controlled, can occasionally appear. But as we found in the previous section (and through examination of all the overhead data), it is not a persistent nor reliable feature of the nighttime ionosphere.

At 0800 UT, a weak auroral E layer is seen at an altitude that is measurably higher than that of the E layer seen during the previous hour. The higher-altitude E layer seen between 0800 and 1300 UT is the evening

and midnight diffuse aurora. The characteristic lowering of the peak altitude of the auroral E layer in the morning sector is seen between 1400 and 1600 MT.

The sunrise effects can be seen between 1800 and 2000 UT. Because of the large zenith angles, the E and F_1 layers never develop fully. Instead, they form a ledge of constant electron density up to the F_2 layer. The F_2 layer profiles between 2000 and 2400 UT are similar to the profile around 0900 UT in the first row, except for a slightly steeper topside slope. Variability in the topside slope may be due to temperature effects in the incoherent-scatter data, which have not been corrected for in these results.

Finally, we examine the profiles shown in the third row in Figure 3-12, taken during an equinoctial period, under more disturbed magnetic conditions. The sunset behavior seen in the summer ionosphere is again evident in this data set, except that it occurs at an earlier local time (but at similar solar zenith angles). The low-altitude auroral E layer is also evident from 0200 to 0600 UT, when the evening diffuse aurora entered the Chatanika radar beam. In this data set, there is very little evidence of even a transient F_2 layer in the dark sector. The dark sector is dominated by the diffuse aurora (i.e., the auroral E layer). The sunrise effect in the E region is masked by the presence of the particle-produced E layer. However, the stable solar-controlled ionosphere is evident after 1900 UT.

From the above discussion, it is clear that the quiet high-latitude electron density profile is controlled by the solar zenith angle. This control is most clearly seen during sunset and sunrise. Electron density profiles that illustrate the decay of the E and F_1 layers, from two summer days, are shown in Figure 3-13. For solar zenith angles less than, say, 70°, the electron density is characterized by a nearly flat profile with evidence of an E layer at 105 km, an F_1 layer at 150 km, and an F_2 layer around 250 km. Peak electron densities for all three layers are of the order of 10^5 el/cm^3 . (We should note again that these profiles have not been corrected for the electron-to-ion temperature ratio, T_e/T_i .) The decay

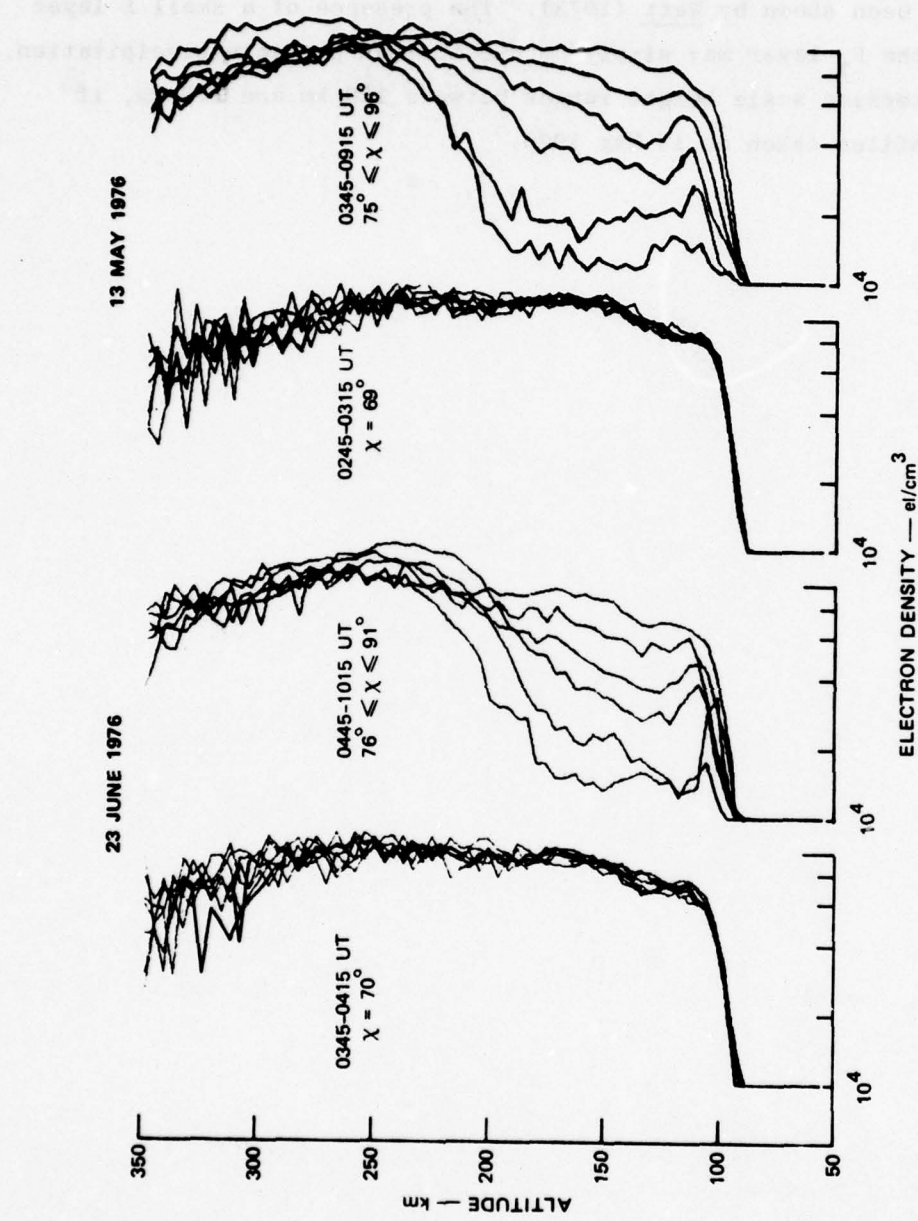


FIGURE 3-13 SOLAR-ZENITH-ANGLE DEPENDENCE OF THE E AND F₁ LAYERS DURING SUNSET ON TWO SUMMER DAYS

of the E and F_1 layers during sunset is seen to occur as the solar zenith angle increase from 75° to 96° . Such a systematic decrease in the density at 120 km has been shown by Watt (1973). The presence of a small E layer greater than the F_1 layer may simply be due to weak particle precipitation. Finally, the topside scale height ranges between 123 km and 196 km, if we use the profiles taken on 13 May 1976.

4. CHATANIKA MODEL OF THE HIGH-LATITUDE IONOSPHERE

In this section we describe the development of the ionospheric model derived from the Chatanika data. This model is basically the RADC-POLAR model with an improved specification of the auroral E layer and the valley region above it.

Like the RADC-POLAR model, our modified version has an empirical basis. Each of the Chatanika profiles used in this study was fitted parametrically. The derived parameters were then statistically related to variations in solar zenith angle and geomagnetic activity.

The first part of this section describes the parametric fitting. Next we discuss the correlation of the parameters with solar and geomagnetic variations and the types of profiles constructed in the model from the parameters. This is followed by a discussion of the latitude and local-time variation in the auroral-E layer specified in the model. Finally we compare old and new profile predictions with Chatanika data on a specific day.

4.1 Extraction of Profile Parameters from Chatanika Data

The ionosphere generator in the RADC-POLAR model employs eight parameters to generate electron density profiles throughout the E, F_1 , and F_2 regions at a particular point in space and time. These parameters are: height of maximum electron density of the E, F_1 , and F_2 layers; critical frequency of the three layers; and semi-thickness of the E and F_2 layers.

In the development of the RADC-POLAR model, extensive data sets were used in determining the morphology of the eight parameters. In particular, the F-layer specification in that model is more accurate than could be derived from the Chatanika data base used in this study. Therefore, we retained the parameters of the F_2 layer. Our aim in modifying the model was to preserve its major predictions and morphology

while introducing a more realistic profile shape and improved auroral E parameters.

We have added four new parameters to define potential valleys in the region between the E and F layers. If a single minimum is present, it is referred to as valley one. If an F_1 layer is present, the minimum between the E and F_1 layers is referred to as valley one, and the minimum between the F_1 and F_2 layers is referred to as valley two. The four new valley parameters are:

- (1) $f_o V_1 / f_o F_2$, the ratio of the plasma frequency of valley one to the critical frequency of the F_2 layer.
- (2) $f_o V_2 / f_o F_2$, the ratio of the plasma frequency of valley two to the critical frequency of the F_2 layer.
- (3) $(HV_1 - HE) / (HF_2 - HE)$, the height above the E layer of valley one, measured as a fraction of the separation between the F_2 layer and the E layer.
- (4) $(HV_2 - HE) / (HF_2 - HE)$, a similar height specification for valley two.

It should be noted that we have loosely used the term " F_1 layer" to represent any local maximum between the E and F_2 layers; this layer is not necessarily the conventional solar-produced F_1 layer. The four valley parameters are used in conjunction with the original eight parameters to produce realistic profiles that more nearly resemble those found in the Chatanika data.

Each Chatanika profile consists of electron density measurements at 5-km altitude intervals. The profiles from the overhead data were computed from integration times equal to either the dwell time at each position or the azimuthal scan time (typically 5 or 6 minutes). For the elevation-scan data we extracted from each contour the vertical profile overhead at Chatanika. From each profile, 12 parameters (8 original and 4 valley) were determined. Since the number of profiles was quite large, a method for finding the parameters was needed that would be fast, efficient and consistent. A computer program was developed that found

the 12 parameters automatically. Improvements were made on this program as the data processing was done, so that all of the data were not processed identically. However, before the final statistics were derived from the parameter values, all of the data were checked and poorly fitted values were eliminated. The final data base was a consistent set of parameters that were then used to determine the morphology of the fitting parameters.

4.2 Variation of Profile Parameters with Solar Zenith Angle and Geomagnetic Activity

The morphology of the parameters has been investigated in terms of magnetic activity and solar illumination, the phenomena that produce the largest effects in the auroral ionosphere. The two categories represent two different physical phenomena: (1) the changes in electron density associated with magnetic activity generally caused by auroral particle precipitation, and (2) the changes related to solar photoionization.

As an index for sorting the solar effects we chose solar zenith angle, which allowed us to combine both diurnal and seasonal changes into one index. The data were grouped into five categories of solar zenith angle: $x < 60^\circ$, $60^\circ < x < 80^\circ$, $80^\circ < x < 90^\circ$, $90^\circ < x < 100^\circ$, and $x > 100^\circ$.

As an index for magnetic effects it was desirable to use K_p , since that parameter is readily available and is in general use in predictive programs. K_p is a planetary geomagnetic activity index and is derived from 12 midlatitude magnetic observatories. We used K_p as a first try at predicting the changes in electron density as a function of magnetic activity. However, we suspected that the correlation might be improved by using a high-latitude magnetic index rather than a planetary one. We chose the local magnetic index at College, Alaska, located approximately 30 km from Chatanika.

Scatter plots of parameter values as a function of K_p and as a function of K were prepared. Figures 4-1 and 4-2 show such scatter plots for one of the parameters--maximum electron density of the auroral E layer--for the two largest solar-z zenith-angle categories. This parameter

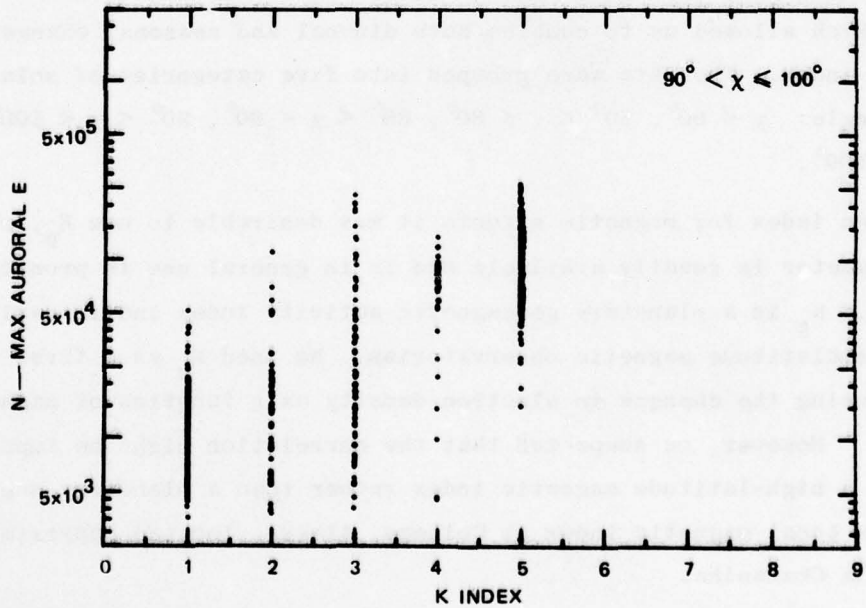
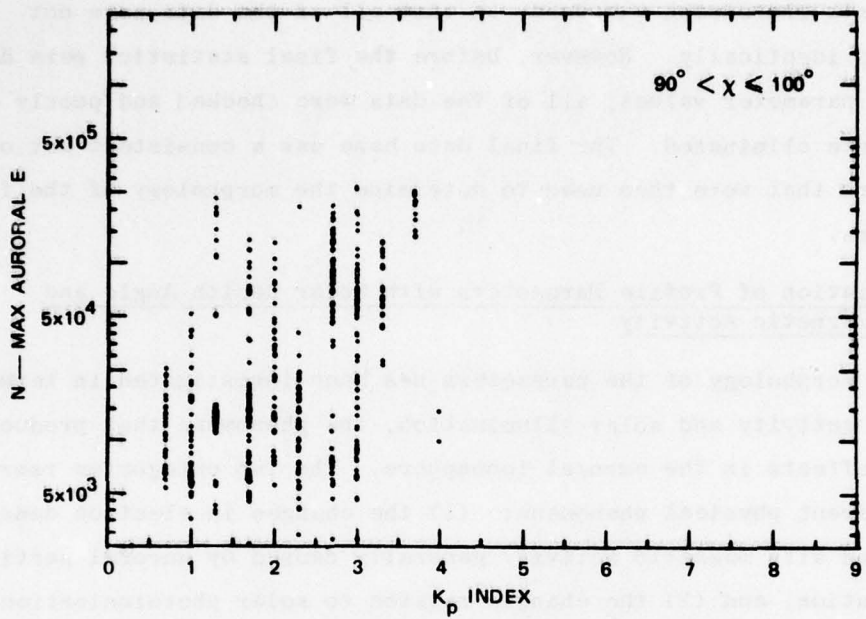


FIGURE 4-1 CORRELATION OF THE MAXIMUM ELECTRON DENSITY OF THE AURORAL E LAYER WITH VARYING GEOMAGNETIC ACTIVITY FOR SOLAR ZENITH ANGLES OF $90-100^\circ$. The geomagnetic indices used are K_p (upper plot) and K (lower plot).

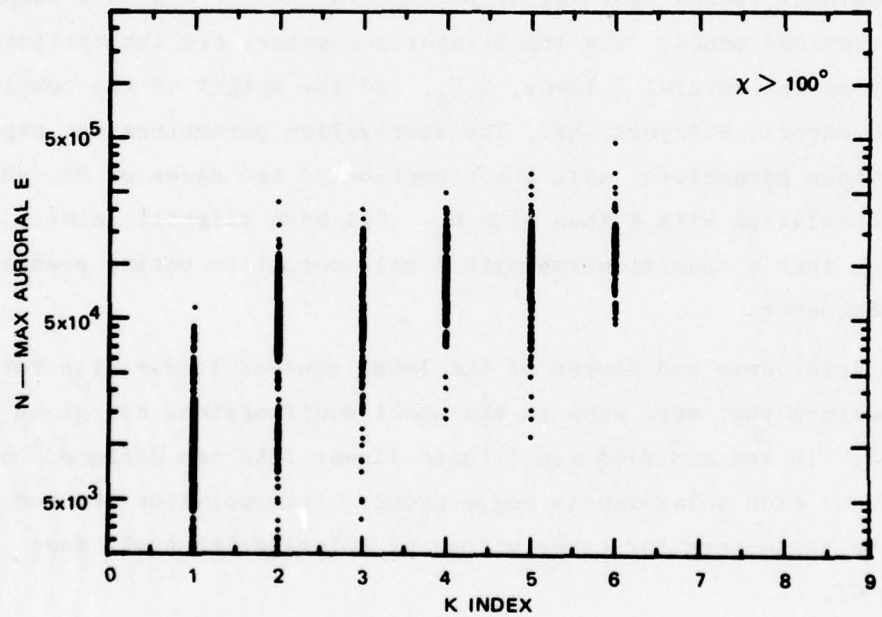
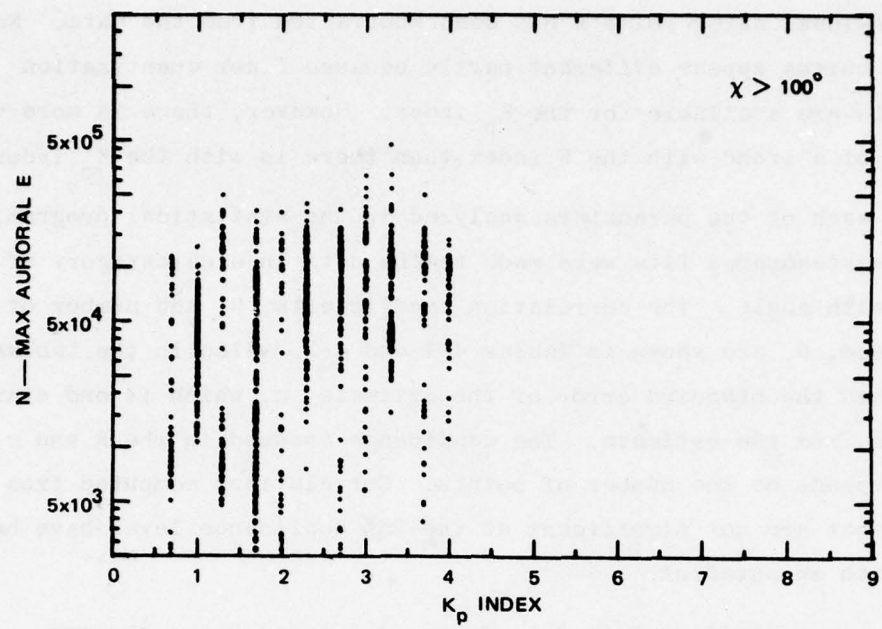


FIGURE 4-2 CORRELATION OF THE MAXIMUM ELECTRON DENSITY OF THE AURORAL E LAYER WITH VARYING GEOMAGNETIC ACTIVITY FOR SOLAR ZENITH ANGLES $> 100^\circ$. The geomagnetic indices used are K_p (upper plot) and K (lower plot).

is the residual after solar E has been subtracted from the data. Note that the curves appear different partly because finer quantization increments are available for the K_p index. However, there is more visual evidence of a trend with the K index than there is with the K_p index.

For each of the parameters analyzed in the statistical program, linear least-squares fits were made to the data in each category of solar zenith angle. The correlation coefficients, R, and number of points used, N, are shown in Tables 4-1 and 4-2. Also in the tables we have listed the standard error of the estimate, σ , which is one standard deviation from the estimate. The confidence assumed in the R and σ values depends on the number of points. Correlations computed from small samples that are not significant at the 95% confidence level have been marked with an asterisk.

The six parameters listed in Tables 4-1 and 4-2 are the two E-layer parameters and four valley parameters that have been incorporated into the revised model. The two E-layer parameters are the critical frequency of the auroral E layer, f_{oA} , and the height of the combined solar and auroral E layers, HE. The four valley parameters are explained above. These parameters, with the exception of two cases of HE, show a higher correlation with K than with K_p . All have slightly lower σ 's, indicating that a specification with K will result in better predictions of the parameter.

The intercepts and slopes of the least-squares linear fits for the six parameters that were used in the model modifications are given in Table 4-3. In the modified model these linear fits are assigned to the average χ of each solar-zenith angle group. Interpolation is used to obtain the parameters for other values of solar-zenith angle (see Appendix C).

The first parameter used in the revised model is the critical frequency of the auroral E-layer. The RADC code predicts the auroral E-layer and the solar E-layer separately and combines them afterward in subroutine ECOMB. The critical frequency of the solar E predicted in the RADC model was subtracted from the data, and predictions were

Table 4-1
CORRELATION OF IONOSPHERIC PARAMETERS WITH K_p FOR FIVE RANGES OF SOLAR-ZENITH ANGLE, χ

Parameter	$\chi < 60$			$60 < \chi < 80$			$80 < \chi < 90$			$90 < \chi < 100$			$\chi > 100$		
	R	σ	N	R	σ	N	R	σ	N	R	σ	N	R	σ	N
f_o^{EA}	0.076*	0.494	106	0.127	1.12	154	0.387	1.23	223	0.459	1.28	473	0.361	1.33	881
HE	-0.125	2.67	447	-0.296	4.90	646	-0.0437	6.67	370	0.0386	8.91	473	-0.0682	9.21	881
$\frac{FV_1}{F_o^2}$	-0.0212*	0.215	31	0.267	0.210	132	0.191	0.225	201	0.353	0.244	263	0.315	0.416	335
$\frac{FV_2}{F_o^2}$	-0.159*	0.239	13	0.264	0.185	35	0.153*	0.159	45	0.399	0.228	210	0.172	0.219	429
$\frac{HV_1 - HE}{HF_2 - HE}$	-0.530	0.178	31	0.203	0.180	132	0.117	0.167	201	0.429	0.125	263	0.190	0.160	335
$\frac{HV_2 - HE}{HF_2 - HE}$	-0.356*	0.0987	13	-0.297*	0.110	35	0.0560*	0.139	45	0.326	0.156	210	0.214	0.165	429

*The correlation between the parameter and K_p is insignificant at the 95% confidence level.

Table 4-2
CORRELATION OF IONOSPHERIC PARAMETERS WITH K FOR FIVE RANGES OF SOLAR-ZENITH ANGLE, χ

Parameter	$\chi < 60$			$60 < \chi < 80$			$80 < \chi < 90$			$90 < \chi < 100$			$\chi > 100$		
	R	σ	N	R	σ	N	R	σ	N	R	σ	N	R	σ	N
$f_o E_A$	0.222	0.483	106	0.421	1.02	154	0.693	0.965	223	0.749	0.953	473	0.730	0.975	881
HE	-0.195	2.64	447	-0.151	5.07	646	-0.0509	6.67	370	0.133	8.84	473	-0.0529	9.22	881
$\frac{FV_1}{f_o F_2}$	0.308*	0.204	31	0.500	0.188	132	0.583	0.186	201	0.619	0.204	263	0.479	0.385	335
$\frac{FV_2}{f_o F_2}$	-0.018*	0.242	13	0.408	0.176	35	0.310	0.153	45	0.622	0.195	210	0.477	0.196	429
$\frac{HV_1 - HE}{HF_2 - HE}$	-0.593	0.169	31	0.433	0.165	132	0.446	0.151	201	0.627	0.108	263	0.411	0.149	335
$\frac{HV_2 - HE}{HF_2 - HE}$	-0.372*	0.098	13	-0.259*	0.111	35	0.217*	0.136	45	0.526	0.141	210	0.321	0.160	429

* The correlation between the parameters and K is insignificant at the 95% confidence level.

Table 4-3

SLOPES AND INTERCEPTS FOR LINEAR FITS TO IONOSPHERIC
PARAMETERS FOR FIVE RANGES OF SOLAR ZENITH ANGLE, χ

Parameter	0 < $\bar{\chi}$ < 60			60 < χ < 80			80 < χ < 90			90 < χ < 100			χ > 100		
	Intercept	Slope	I	S	I	S	I	S	I	S	I	S	I	S	
$f_o F_A$	1.68	0.0850	1.67	0.377	0.887	0.623	0.477	0.737	0.899	0.625					
H_e	116	-0.541	116	-0.681	117	-0.261	114	0.737	118	-0.292					
$\frac{HV_1 - HE}{HF_2 - HE}$	0.591	-0.115	0.0552	0.0699	0.163	0.0648	0.206	0.0580	0.347	0.0421					
$\frac{HV_2 - HE}{HF_2 - HE}$	0.795	-0.0307	0.694	-0.0196	0.606	0.0195	0.372	0.0553	0.538	0.0329					
$fV \frac{1}{f_o F_2}$	0.914	0.0614	0.577	0.0957	0.460	0.115	0.302	0.108	0.440	0.132					
$fV \frac{2}{f_o F_2}$	0.742	-0.00333	0.666	0.0516	0.755	0.0321	0.297	0.0981	0.474	0.0644					

made on the residual, using the method in ECOMB. Figure 4-3 shows the results of linear fits of $f_o E_A$ versus K for various solar-zenith-angle ranges. The curves are labeled with the average solar zenith angle for each group. We see that magnetic dependence on K increases with solar zenith angle. For $\chi < 60^\circ$, $f_o E_A$ is nearly flat; for $60^\circ < \chi < 80^\circ$, the curve steepens; and for $\chi > 80^\circ$ there is a very strong dependence on K .

The second parameter that we predict is the height, HE , of the combined solar and auroral-E layers. We first tried to predict the height of the auroral component alone by subtracting out the predicted solar layer height. This was unsatisfactory because the solar-E height prediction was unreasonably high in some cases, ranging up to 160 km. Reasonable values were obtained for HE , but they were not highly correlated with K (see Table 4-2). As shown in Figure 4-4, only a slight altitude variation was found in the parametric analysis. We see that the height of the E layer generally decreases slightly with increasing K and increasing solar zenith angle, except for the solar-zenith-angle group $90^\circ < \chi < 100^\circ$, which shows the opposite trend.

All of the valley parameters are predicted in the form of ratios scaled to the $f_o F_2$ or HF_2 , which were presumed to be well predicted in the RADC code. (An exception, evident in Figure 5-5, is the occasional occurrence of unrealistically low altitudes of HF_2). We chose to relate the valley parameters to $f_o F_2$ rather than to $f_o E$ because the correlation coefficient with K was higher. In addition, because the Chatanika data were not temperature-corrected, accuracy is improved if valley ratios are scaled to the F region rather than the E region. This effect is discussed in Appendix A. Figure 4-5 shows the scatter plots of ratios for the critical frequency of valley one with the best-fit lines plotted on the graph for the two largest solar-zenith-angle groups. Figure 4-6 shows the corresponding scatter plots for valley two.

Figure 4-7 shows depth of valley one (relative to $f_o F_2$) as a function of K for various solar zenith angles. Here there appears to be a definite trend for the deepest valleys to occur at low K values and large solar zenith angles. Apparently, for high K values the F_1 region

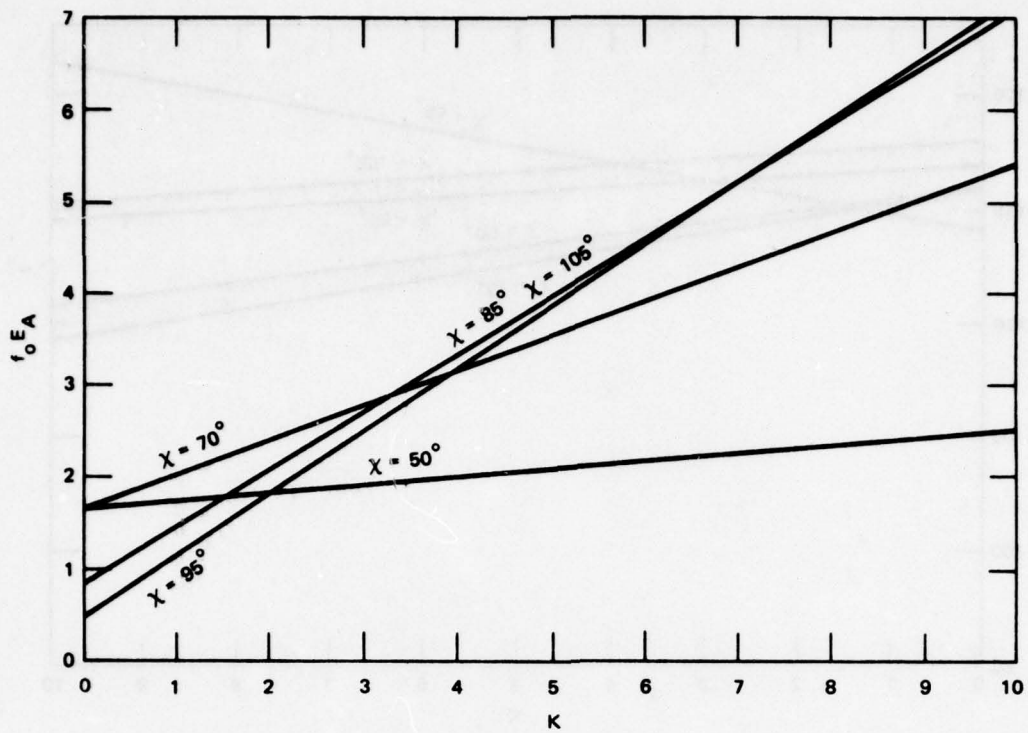


FIGURE 4-3 CRITICAL FREQUENCY OF THE AURORAL E-LAYER, f_0E_A , AS A FUNCTION OF K FOR VARIOUS SOLAR ZENITH ANGLES, χ

is filled in by particle-produced topside E. The depth of valley two as a function of K for various solar zenith angles is shown in Figure 4-8. Here a similar trend occurs, but the χ dependence is not as definite, and for $\chi < 60^\circ$ there is no dependence on K.

Figure 4-9 shows the height parameter of valley one as a function of K for various solar zenith angles, χ . All curves show a tendency for the valley to increase in altitude as K increases ($\chi < 60^\circ$), as one might expect from an increase in precipitation. The only exception is the line for $\chi < 60^\circ$, which is based on a small data set and was not statistically significant.

Figure 4-10 shows the height ratio of valley two as a function of K for various solar zenith angles, χ . These curves seem to have a somewhat consistent trend, with the height of the valley decreasing as a function of K for small solar zenith angles and gradually switching to an

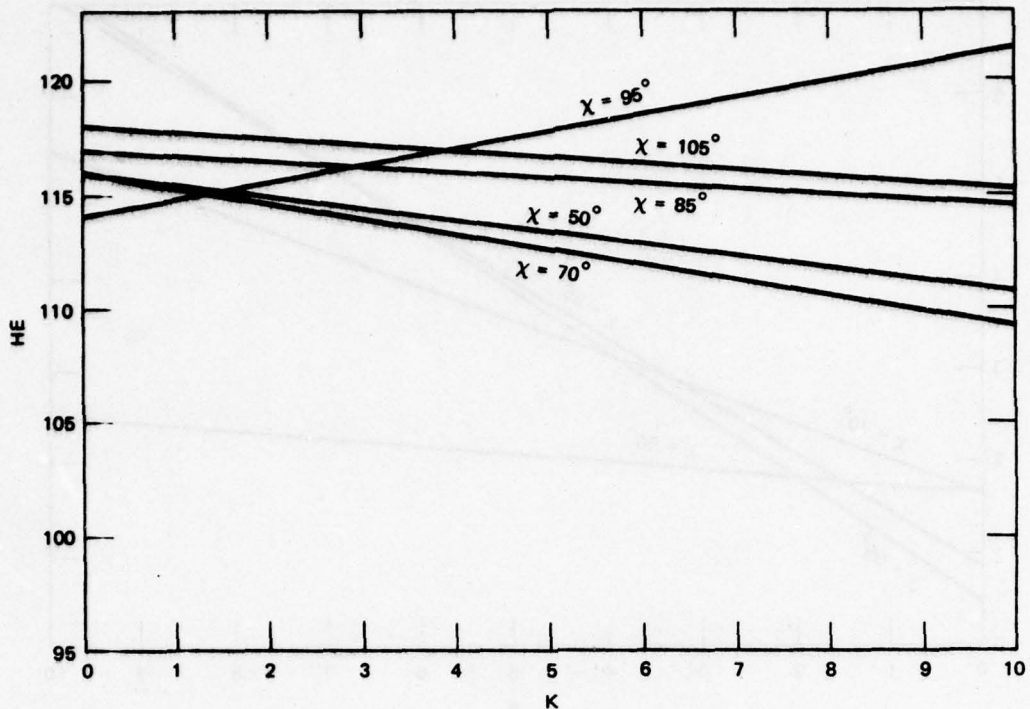


FIGURE 4-4 HEIGHT OF THE COMBINED SOLAR AND AURORAL E-LAYERS AS A FUNCTION OF K FOR VARIOUS SOLAR ZENITH ANGLES, χ

increasing height of the valley as a function of K for large solar zenith angles.

4.3 Profile Shapes

The version of the RADC-POLAR model that is the basis for the current modification provided four types of profiles. These four types were generated from the eight ionospheric parameters that were predicted as functions of the particular time, location, and magnetic activity. The eight parameters are height and maximum electron density of the E, F_1 , and F_2 layers, and semi-thickness of the E and F_2 layers.

In order to simulate the electron density profiles that are found in the auroral region we found it necessary to add four new profile types to the four that existed originally. The main change in profile

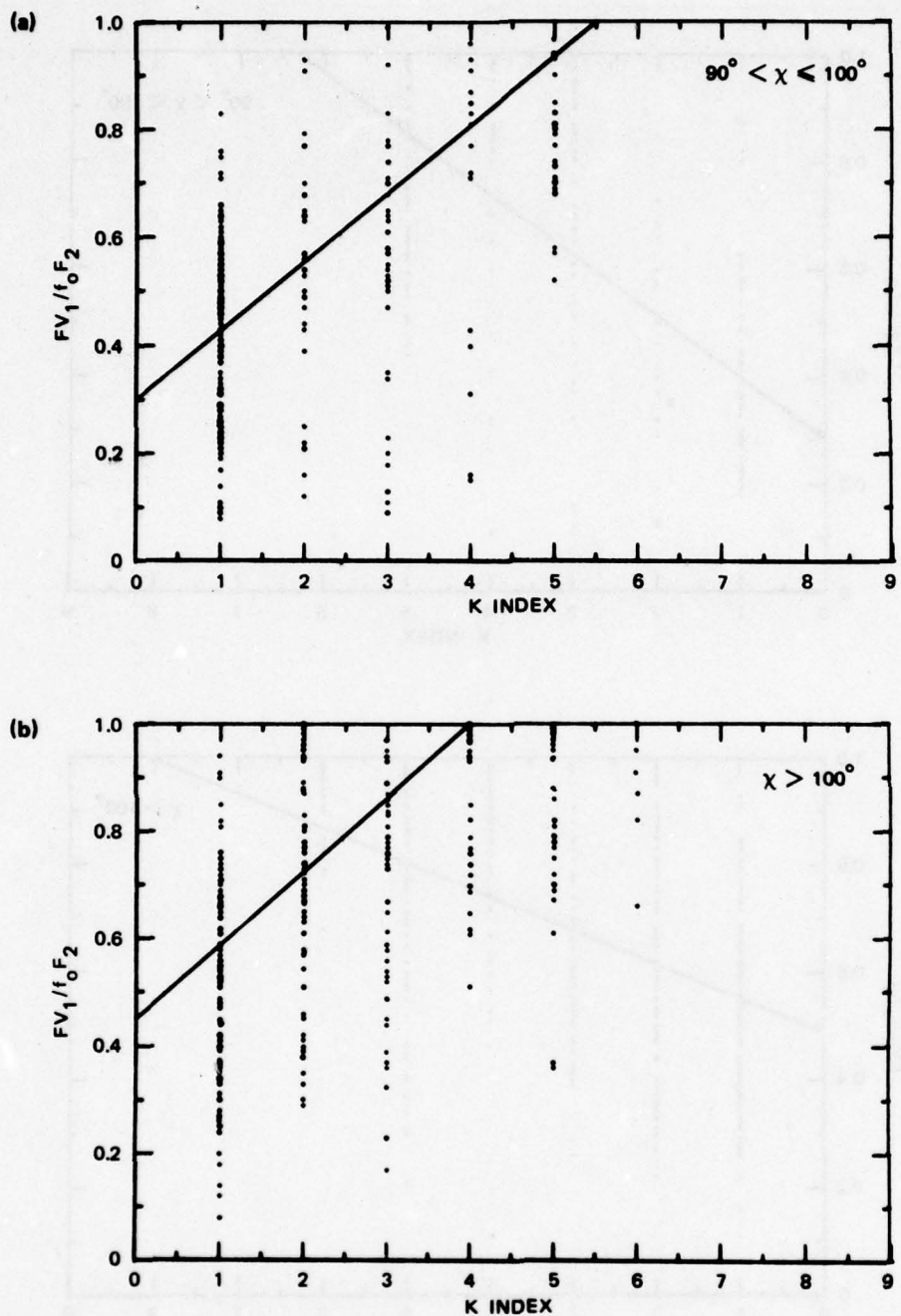


FIGURE 4-5 SCATTER PLOTS WITH BEST-FIT LINES FOR THE VALLEY-ONE PARAMETER, f_0V_1/f_0F_2 , FOR VARIOUS SOLAR ZENITH ANGLES, x

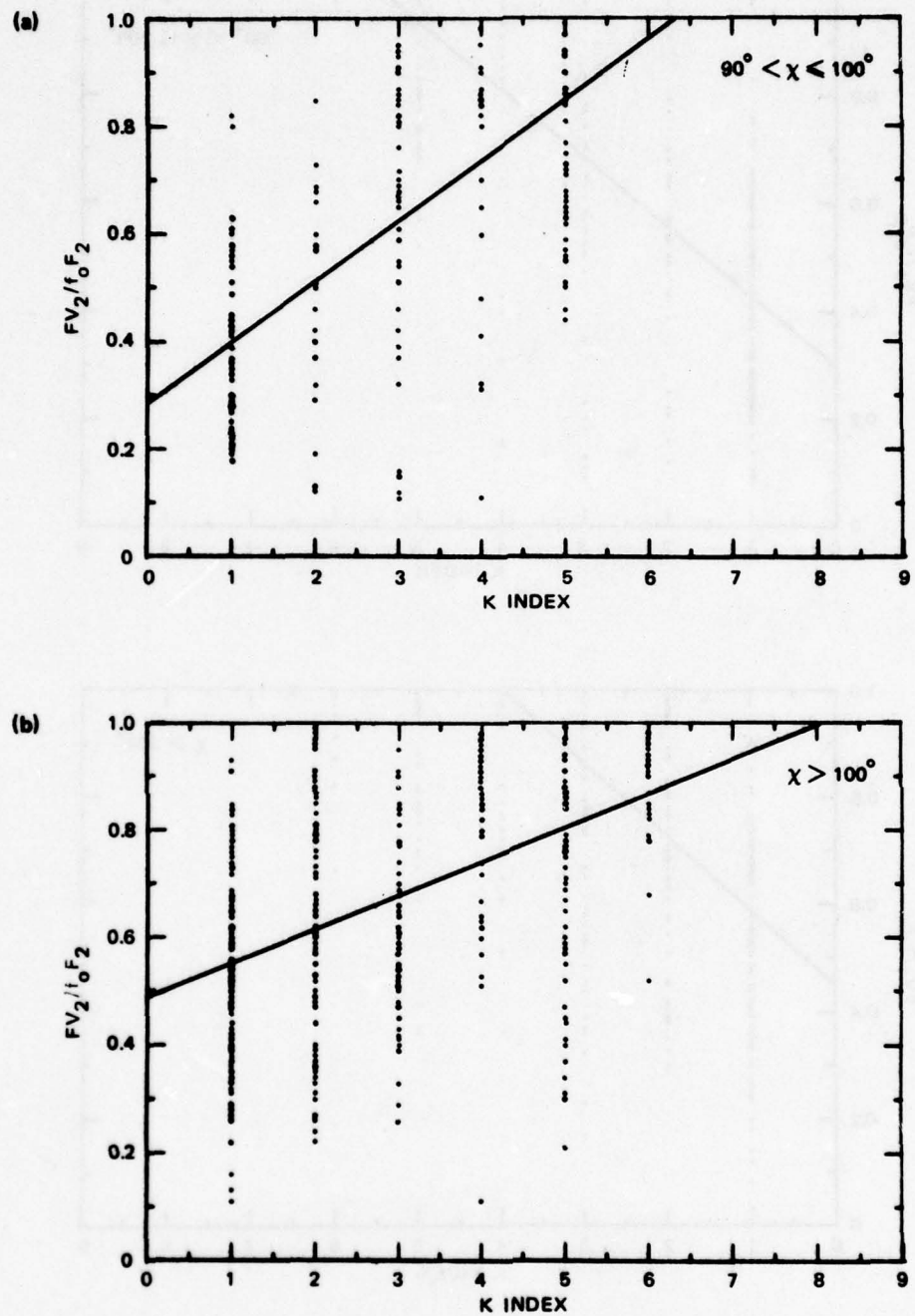


FIGURE 4-6 SCATTER PLOTS WITH BEST-FIT LINES FOR VALLEY-TWO PARAMETER,
 $f_0 V_2/f_0 F_2$, FOR VARIOUS SOLAR ZENITH ANGLES, x

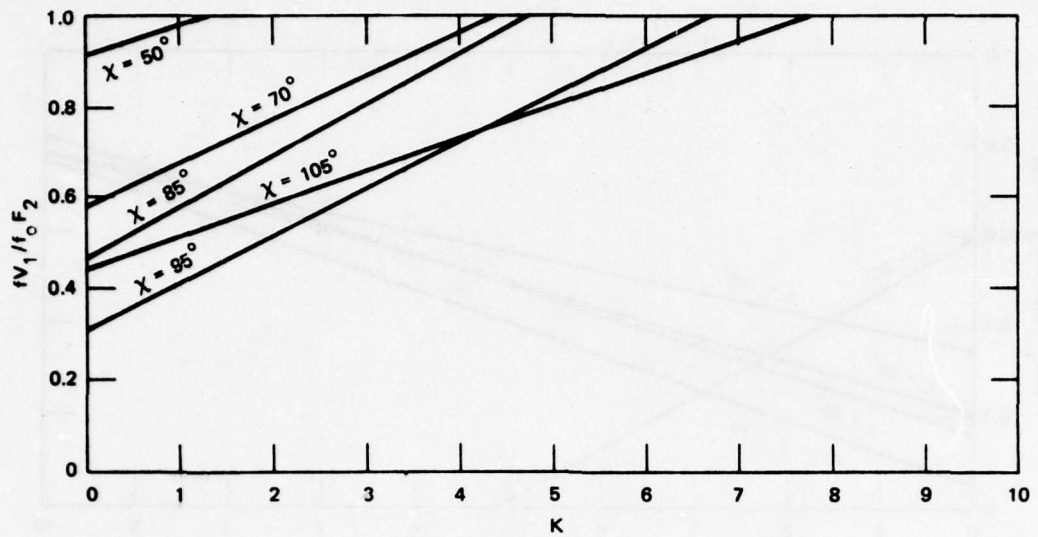


FIGURE 4-7 RATIO OF MINIMUM PLASMA FREQUENCY AT VALLEY ONE TO CRITICAL FREQUENCY OF F_2 LAYER, f_0V_1/f_0F_2 , AS A FUNCTION OF K FOR VARIOUS SOLAR ZENITH ANGLES, X

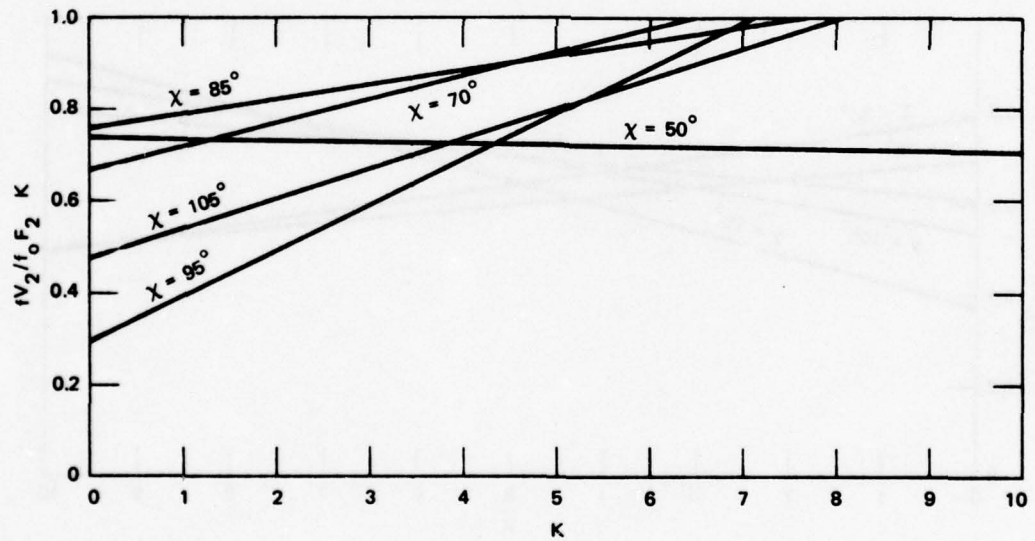


FIGURE 4-8 RATIO OF PLASMA FREQUENCY AT VALLEY-TWO MINIMUMS TO CRITICAL FREQUENCY OF F_2 LAYER, f_0V_2/f_0F_2 , AS A FUNCTION OF K FOR VARIOUS SOLAR ZENITH ANGLES, X

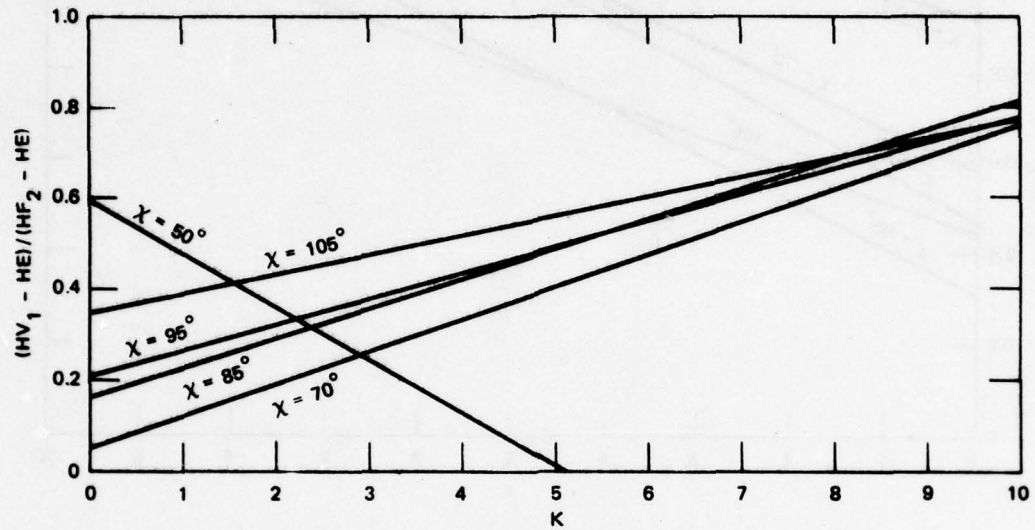


FIGURE 4-9 RATIO OF VALLEY-ONE HEIGHT ABOVE THE E-LAYER TO THE DIFFERENCE IN HEIGHT BETWEEN E AND F_2 LAYERS AS A FUNCTION OF K FOR VARIOUS SOLAR ZENITH ANGLES, χ

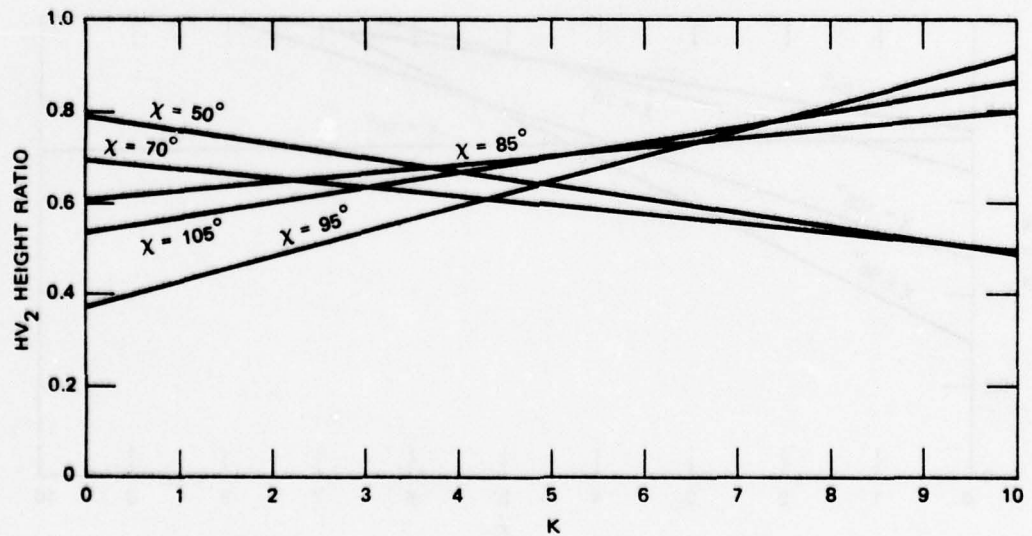


FIGURE 4-10 RATIO OF VALLEY-TWO HEIGHT ABOVE THE E-LAYER TO THE DIFFERENCE IN HEIGHT BETWEEN E AND F_2 LAYERS AS A FUNCTION OF K FOR VARIOUS SOLAR ZENITH ANGLES, χ

shapes are those having a dense auroral E-layer. These have been modified to look more like the profiles observed at Chatanika. Two of the new profiles exhibit valleys between the E and F_1 layer, or the E and F_2 layer. The other two represent an exponential-type electron density distribution without a valley that occurs when an F_1 layer is present or when only an F_2 layer is present.

The four profile types in the original code were:

(1) A Single F_2 -Layer Profile

This type of profile is a standard type that occurs at night in midlatitudes. A parabolic layer is used to represent it. Use of this profile remains unchanged.

(2) A Two-Layer (E and F_2) Profile

When $f_o E$ is less than $f_o F_2$, this profile is a fairly good representation of a daytime midlatitude ionosphere without an F_1 layer. However, when $f_o E$ is greater than $f_o F_2$, this profile type does not represent the data well. In this case, we have substituted an auroral two-layer profile (type 7). The RADC layer-generator PROF3 is still used for $f_o E < f_o F_2$.

(3) A Two-Layer Profile With a Valley

This profile can be used only when $f_o E$ is less than $f_o F_2$. In many cases it is a good representation of a profile with a valley. The depth of the valley is defined in the RADC layer-generator PROF3 according to the relative density of the E and F_2 layers. To avoid conflicting valley occurrence patterns, we omit this profile in the region where the depths of the valleys are being predicted.

(4) A Three-Layer Profile Without Valleys

When $f_o E < f_o F_1 < f_o F_2$, this profile is a good representation of a midlatitude daytime profile with an F_1 layer. It also represents well the profile with $f_o F_1 > f_o E$ and $f_o F_1 > f_o F_2$,

a situation that occurs frequently in the auroral zone. For cases when $f_o F_1 < f_o E$ in the auroral zone this profile is a poor representation. We have substituted an auroral three-layer profile (type 8) for cases of this type. For a type 4 we have added the feature that if a valley occurs between the E and F_1 or between the F_1 and F_2 layers, it will be represented. The RADC layer-generator PROF3 is then used for this profile.

The four auroral profile types that have been added are:

(5) An Auroral Two-Layer Profile With a Valley

This profile occurs when the solar E is less dense than the F_2 layer but a particle-produced auroral E layer is present. The shape of this profile above the F maximum is generally exponential up to the valley minimum in these cases. The new profile routine uses a combination of exponential for the E layer, and Chapman for the F_2 layer, to generate the profiles, with the valley depth and height matched as closely as possible. Figure 4-11(a) shows a profile of this type. The plus signs are actual data points; the dashed line is a smoothed version of the data points. Parameters found from the data were supplied to the RADC profile routine to generate the dotted-line profile and also to the new profile routine to generate the solid-line profile; thus the SRI and RADC profiles are forced to agree at the layer peaks.

(6) An Auroral Three-Layer Profile With a Valley Between the E and F_1 and Possibly Between the F_1 and F_2

This profile will occur when the solar E is less dense than the F_1 layer and an auroral enhancement of the electron density is present in the E region. Figure 4-11(b) shows a profile of this type. There is no pronounced F_1 layer, but the layer is visible with shallow valleys below and above

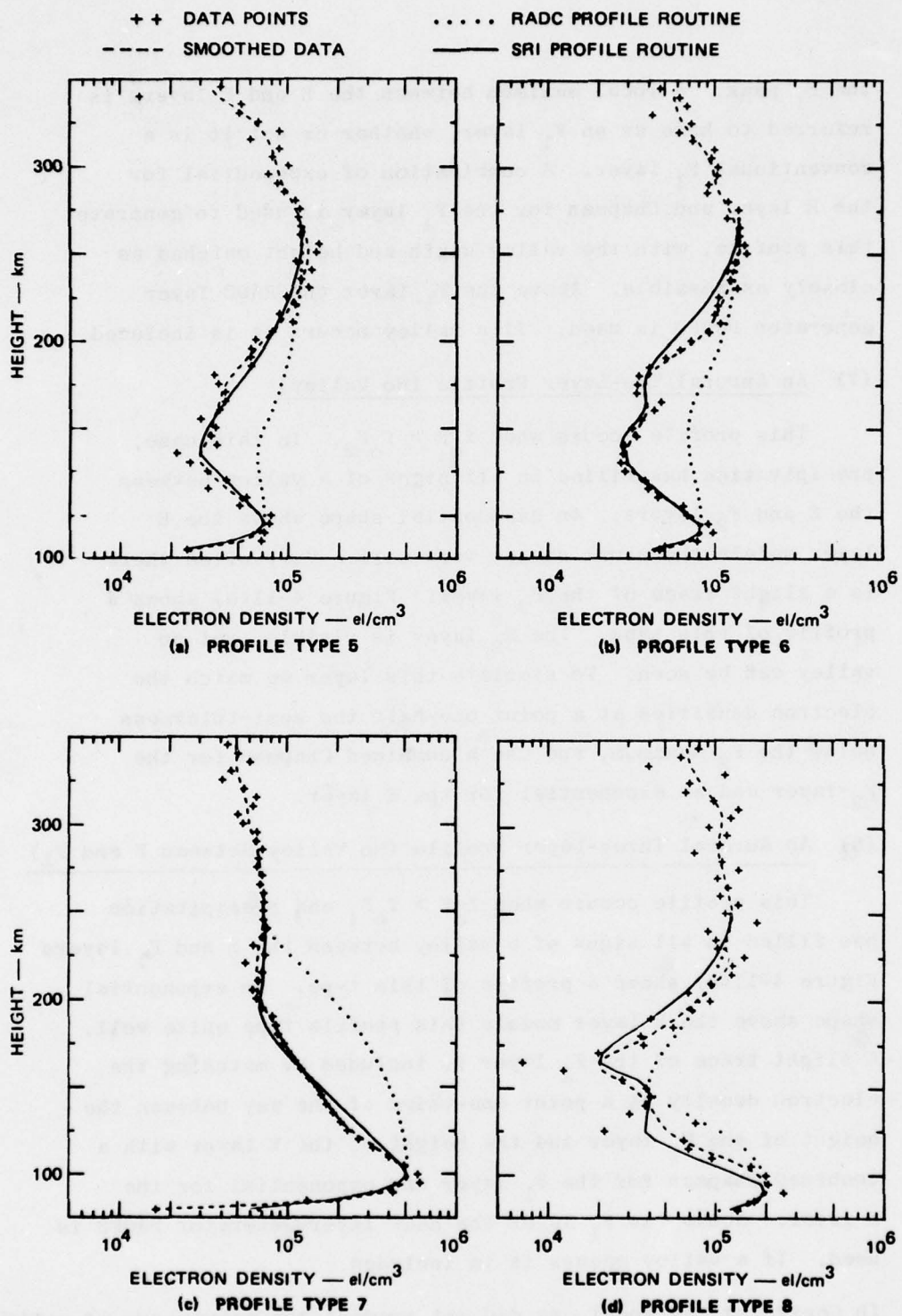


FIGURE 4-11 COMPARISON OF PROFILES GENERATED BY THE RADC AND SRI MODELS WITH ACTUAL CHATANIKA MEASUREMENTS. (a) Type 5; (b) Type 6; (c) Type 7; (d) Type 8.

the F_1 peak. A local maximum between the E and F layers is referred to here as an F_1 layer, whether or not it is a conventional F_1 layer. A combination of exponential for the E layer and Chapman for the F_1 layer is used to generate this profile, with the valley depth and height matched as closely as possible. Above the F_1 layer the RADC layer generator PROF3 is used. If a valley occurs it is included.

(7) An Auroral Two-Layer Profile (No Valley)

This profile occurs when $f_o E > f_o F_2$. In this case, precipitation has filled in all signs of a valley between the E and F_2 layers. An exponential shape above the E layer models the usual shapes very well. Very often there is a slight trace of the F_2 layer. Figure 4-11(c) shows a profile of this type. The F_2 layer is visible, yet no valley can be seen. To simulate this layer we match the electron densities at a point one-half the semi-thickness below the F_2 maximum, and use a combined Chapman for the F_2 -layer and an exponential for the E layer.

(8) An Auroral Three-Layer Profile (No Valley Between E and F_1)

This profile occurs when $f_o E > f_o F_1$ and precipitation has filled in all signs of a valley between the E and F_1 layers. Figure 4-11(d) shows a profile of this type. An exponential shape above the E layer models this profile type quite well. A slight trace of the F_1 layer is included by matching the electron density at a point one-third of the way between the height of the F_1 layer and the height of the E layer with a combined Chapman for the F_1 layer and exponential for the E layer. Above the F_1 layer the RADC layer-generator PROF3 is used. If a valley occurs it is included.

In designing the model, we did not predict the occurrence of valleys directly. Instead, we assumed that if a valley is present, its parameters are defined by the x and K dependence computed from the data base of all

profiles containing valleys. A model profile is constructed from the RADC F-region parameters, the predicted E-region parameters, and the valley parameters. This profile is automatically subjected to a number of tests to determine whether such a valley is consistent with the E- and F-region parameters. Since the potential existence of a valley depends strongly on the height increment between the E and F layers, an abnormally low predicted height of the F region was responsible for the elimination of valleys in several cases. (For example, notice that the F-region height is less than 200 km at the right end of the contour in Figure 5-5).

4.4 Latitude and Local-Time Variations of Auroral-E

As indicated in Section 4.2, the statistical parameters extracted from the Chatanika data that were used to generate the ionospheric profiles were better correlated with K than they were with K_p . However, for several reasons we still wished to retain K_p as the index of geomagnetic activity. First, K_p is a planetary index that is readily available. Also, a predictive model based solely on K would require measurements of the local magnetic variation over the entire high-latitude auroral region. Finally, the present predictive models generally use K_p , and we preferred to have our model compatible with them.

In order to retain K_p , we needed to establish a correlation between K_p and the local magnetic index K at high-latitudes. This was accomplished by the analysis of one year of magnetic data from 16 high-latitude sites. To illustrate the results we show in Figure 4-12 the K variation with latitude and local time for a K_p value of 3. Diurnal and latitudinal variations, including a feature reminiscent of the night-side auroral oval, are readily apparent in the figure. The method used and the results obtained for other values of K_p are discussed in detail in Appendix B.

The establishment of a relationship between K and K_p allowed us to retain K_p as the index of magnetic activity. In addition, it resulted in the incorporation into the model an auroral oval with both latitudinal and local time variations. A major shortcoming of the RADC-POLAR model

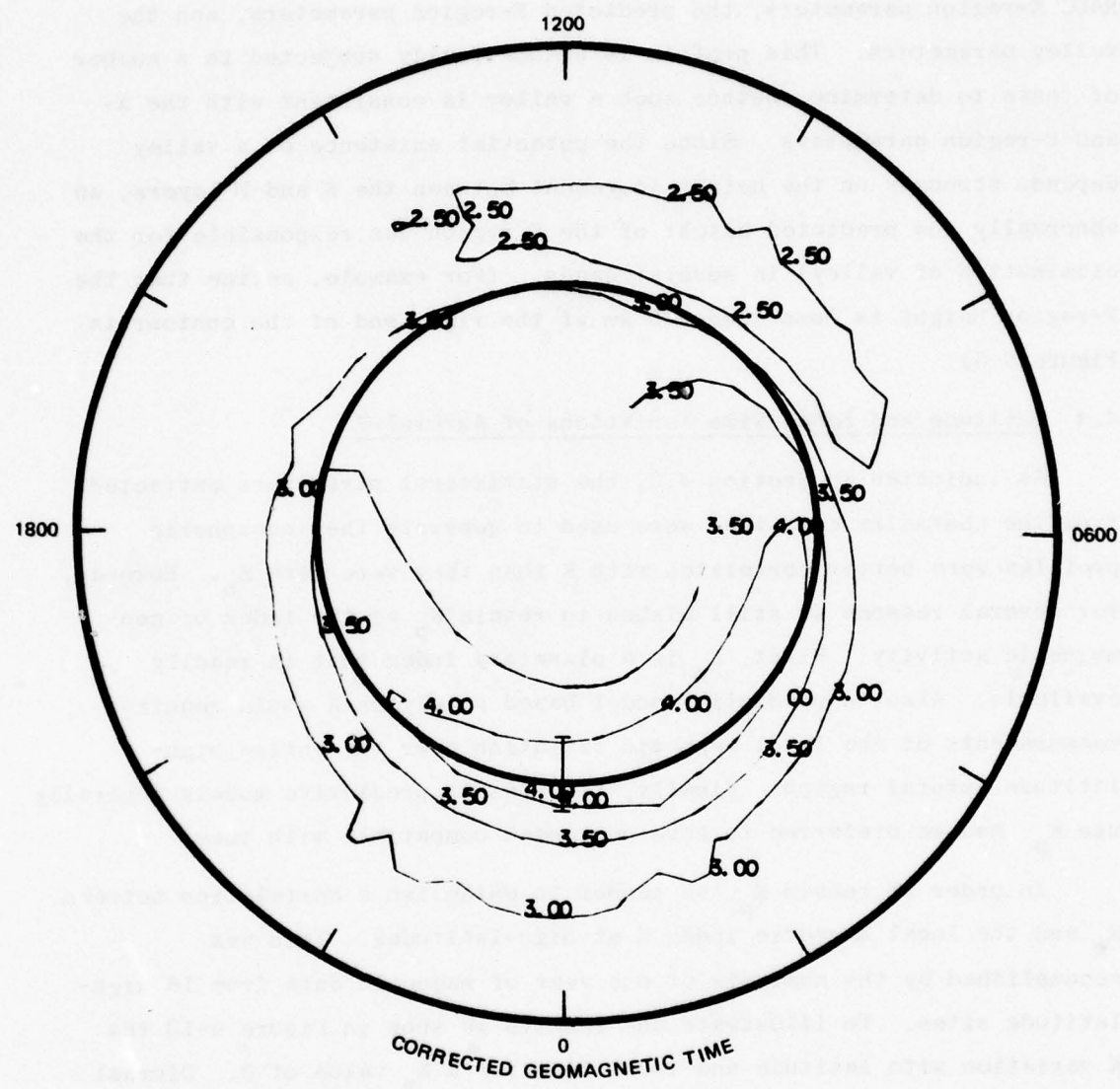


FIGURE 4-12 VARIATION OF K WITH CORRECTED GEOMAGNETIC LATITUDE AND CORRECTED GEOMAGNETIC LOCAL TIME FOR A K_p OF 3

is that for a specified value of K_p it predicts an auroral E that is homogeneous in both latitude and local time throughout the oval. If we assume that electron-density profiles at high latitudes have a correlation with K_p similar to that found in the Chatanika data, we can use the K_p -versus- K_p distributions to extend our results to the whole auroral zone. The results obtained do represent a realistic auroral morphology. Thus, the modified auroral E layer is an improvement because it varies with magnetic activity, corrected geomagnetic time, corrected geomagnetic latitude, and solar zenith angle.

The location of the auroral oval has been modified slightly from that specified in the RADC-POLAR model. The boundaries of the predicted nightside auroral oval were compared with recent measurements by the ISIS-2 auroral scanning photometer (Murphree and Anger, 1977). As shown in Figure 4-13, the equatorward oval boundaries were found to be in reasonably close agreement. However, the poleward boundary of the auroral oval in the RADC model moves equatorward with increasing K_p . Although the poleward oval boundary is not as well defined in experimental data, the observations do indicate a poleward expansion with increasing magnetic activity (Akasofu, 1977). The poleward boundary of the photometric oval (Murphree and Anger, 1977; Murphree, private communication, 1977) and the 40-keV electron-trapping boundary (Page and Shaw, 1972) are indicated in Figure 4-13. We decided to retain the equatorward boundary specified in the RADC model and fix the nightside poleward boundary at a corrected geomagnetic latitude of 72° . The general decrease of K_p with increasing latitude provides a taper to the poleward edge of the auroral oval through the corresponding reduction in electron density of the auroral E layer.

On the dayside we kept the present RADC specification of the auroral oval (dayside cusp) because that region generally is outside the Chatanika field of view. However, we chose to include a dayside auroral E to the south that is specified by the K_p distribution obtained in our analysis. As discussed in Section 3, precipitation is observed at Chatanika south of the dayside oval. Data south of the auroral oval

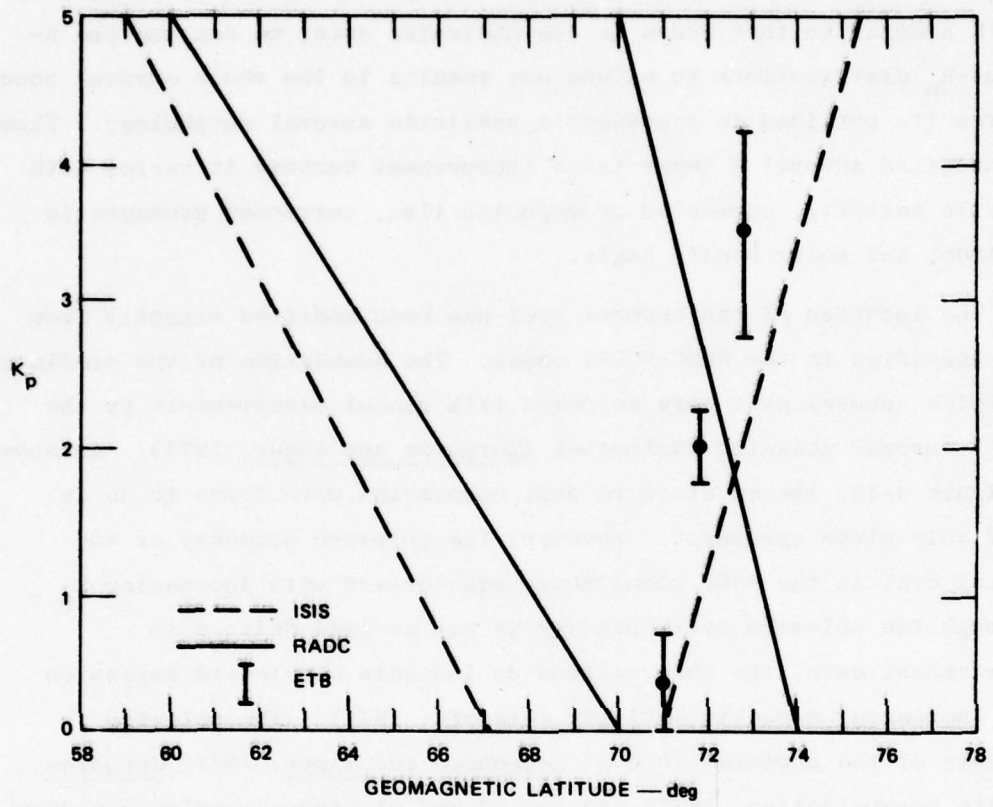


FIGURE 4-13 BOUNDARIES OF THE AURORAL OVAL AT GEOMAGNETIC MIDNIGHT AS DEFINED IN THE RADC-POLAR MODEL AND AS DETERMINED FROM ISIS-2 DATA. The dashed lines indicate linear fits to ISIS observations (Murphree and Anger, 1977; Murphree, private communication, 1977) and the solid lines indicate the RADC boundaries. Also indicated is the 40-keV electron trapping boundary (ETB) determined from ESRO 1 observations (Page and Shaw, 1972).

on the dayside were included in the Chatanika data base; therefore, we feel that our estimates for this region are reasonable. On the dayside we predict values of auroral E south to 51° corrected geomagnetic latitude using the spatial, magnetic, and solar parameters described above. South of 51° corrected geomagnetic latitude on the dayside we use 1.5 MHz for the auroral E layer.

Unrealistically high values of $f_o E_A$ were predicted in the RADC-POLAR model (Version dated 2-3-77) at all latitudes south of the auroral oval. A constant value of 3 MHz was assigned to the auroral E-layer in this region. We introduce more realistic values by assuming that south of the auroral oval on the nightside there will be no auroral activity; a critical frequency of 1.5 MHz has been assigned to the auroral E-layer there.

The auroral E layer in the polar-cap region remains unchanged because we had no data that could be used to modify the RADC predictions.

4.5 Comparison of Chatanika Data with Original and Modified Profile Predictions

In this subsection we compare measured Chatanika profiles with predictions from both the RADC-POLAR ionosphere and the revised model. Because the ionospheric models are statistical mean models, one cannot expect predictions for an arbitrary specific day to agree with actual observations. The comparison is made simply to illustrate specific examples of profiles generated by the models and to show similarities and differences between them and actual instantaneous measurements of the ionospheric profiles.

Chatanika data from 17 March 1976 are shown in Figure 4-14, with predictions from the RADC-POLAR model and the SRI modification of it. The dashed line indicates the measured profile, the dotted line indicates the RADC profile, and the solid line indicates the SRI modification. It should be recalled that both models use the same F_2 -region parameters. The measured profiles have not been corrected for temperature effects (see Appendix A). However, estimated corrections at three altitudes are indicated in the figure.

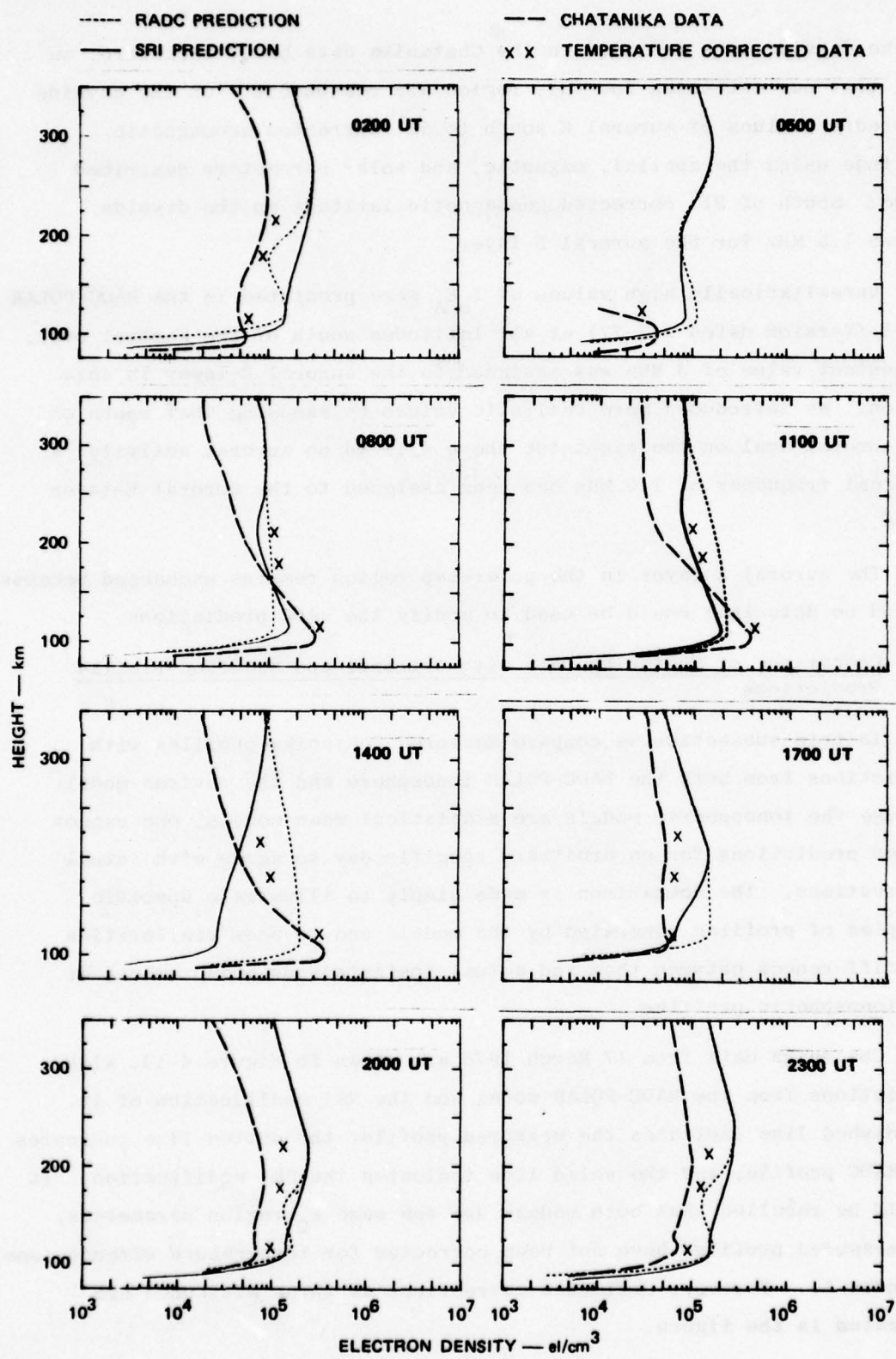


FIGURE 4-14 COMPARISON OF CHATANICA DATA WITH MODEL PREDICTIONS
ON 17 MARCH 1976

- The uncorrected critical frequency of the F_2 layer as measured is generally less than predicted. A temperature correction results in a better agreement.
- The predicted F_2 layer critical frequency is much too large at 0500 UT. Apparently Chatanika was in the trough at that time.
- The midnight-sector (1100 UT) predicted critical frequency of the auroral E-layer is smaller than actually occurred.
- At 1400 UT the southern edge of the auroral oval was predicted to be north of Chatanika, whereas Chatanika was actually in the auroral oval at this time.
- Predicted daytime densities for the auroral E layer are greater than observed (e.g., 0200, 2000 and 2300 UT).

Improvements in the profiles are seen in:

- The shape of the profiles having an $f_o F_2 > f_o E$ is improved. Valleys were not predicted by the SRI model and they did not occur.
- The shape of the profiles having an $f_o E > f_o F_2$ is improved. At 0800 UT and 1100 UT the shape directly above the E layer, although not perfect, is more like the actual profile.

5. SAMPLE RAYTRACINGS THROUGH ORIGINAL AND MODIFIED IONOSPHERES

In order to demonstrate the usability of our modifications to the RADC-POLAR ionosphere, we computed ray trajectories along long-range propagation paths in both versions. Ray trajectories were computed with a three-dimensional raytracing program provided by RADC (Toman and Miller, 1977a,b). Trajectories were computed for ordinary-mode electromagnetic waves. The particular propagation path chosen was one that extended from the western United States toward Europe, as shown in Figure 5-1. Computations were made for two times on 15 April for a moderate level of solar activity. The first time was across the dayside auroral ionosphere and the second was across the nightside auroral ionosphere.

5.1 Dayside Propagation Path

The ionospheric contours of local plasma frequency derived from the RADC-POLAR model are shown in Figure 5-2. The model was sampled at distance increments of 400 km along the surface of the earth for the time 1800 UT, a sunspot number of 50, and a K_p of 2. A conspicuous feature in the ionospheric contour is the dayside auroral E layer centered at a distance of 3500 km with an enhanced F region above it. Ray trajectories were computed for a transmitted frequency of 20 MHz and initial elevation angles of 0° to 12° , in 2° increments. Trajectories are shown only for a single hop to the earth's surface; no ducting occurred on subsequent hops. It can be seen that the wave launched at a 10° elevation angle is ducted to great distance.

The ionospheric contours generated by the modified ionospheric model for the same time and solar/geophysical conditions are shown in Figure 5-3. The F-region contours are similar except for the addition of a deep valley at a distance of about 6400 km. The E-region critical

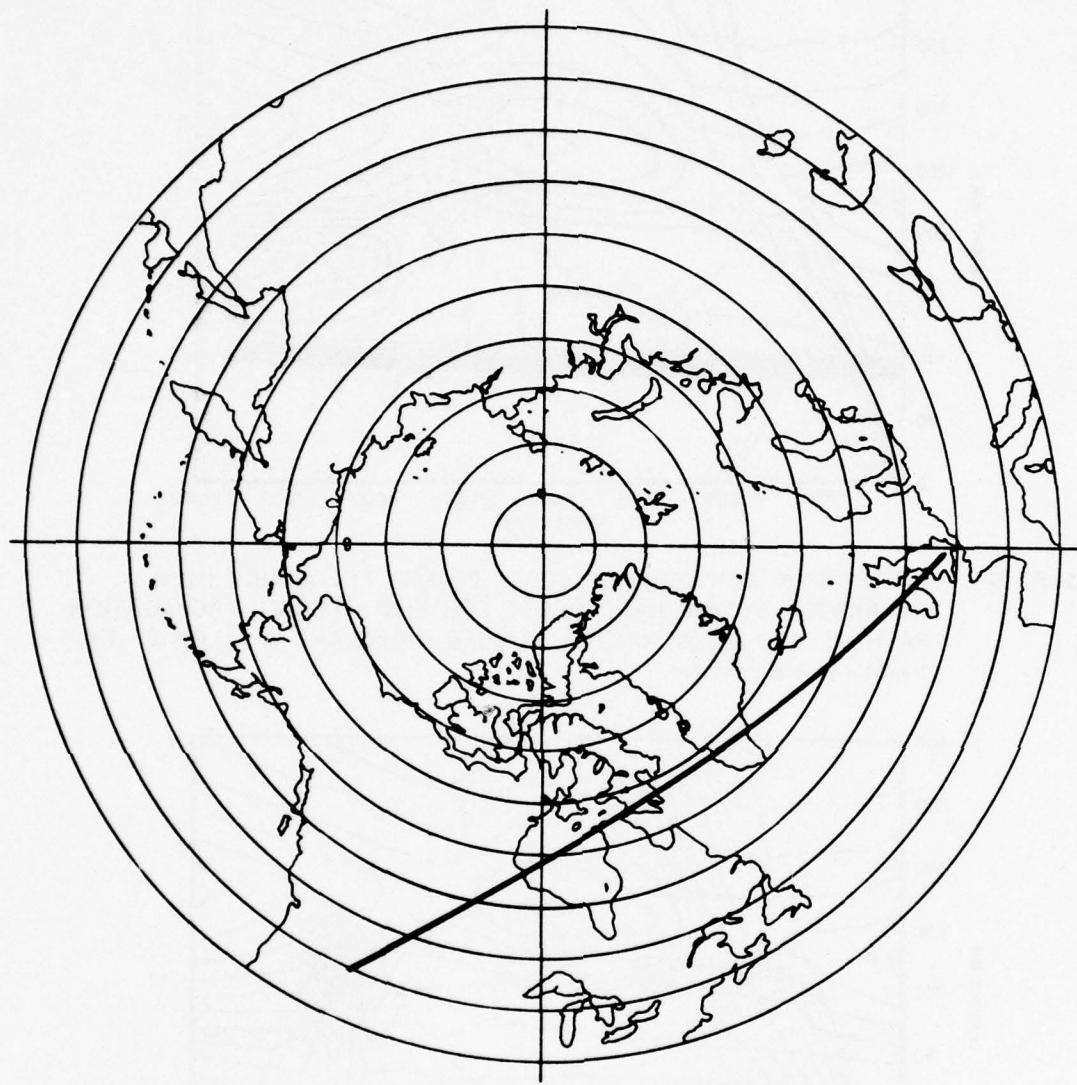


FIGURE 5-1 POLAR VIEW OF NORTHERN HEMISPHERE WITH SELECTED PROPAGATION PATH

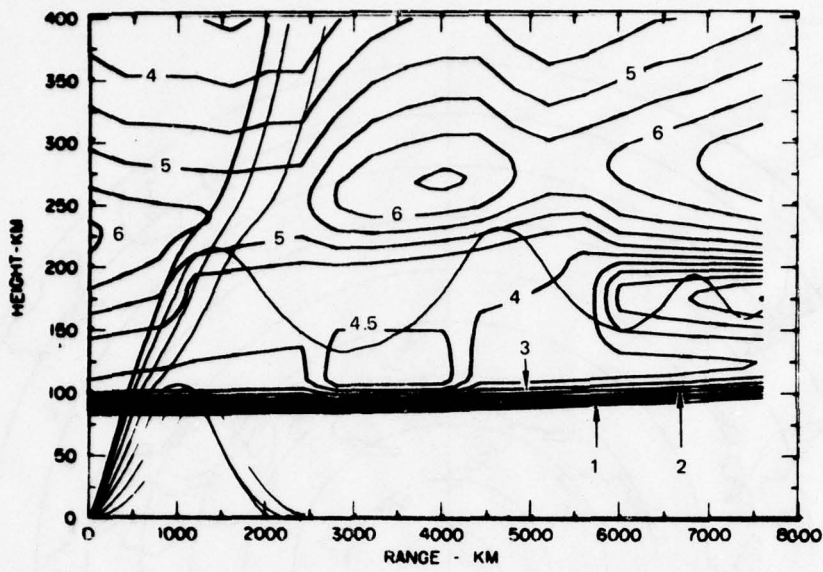


FIGURE 5-2 IONOSPHERIC CONTOURS OF LOCAL PLASMA FREQUENCY (MHz) GENERATED BY THE RADC MODEL FOR THE SELECTED PROPAGATION PATH AT 1800 UT, A SUNSPOT NUMBER OF 50, AND A K_p OF 2. Ray trajectories are indicated.

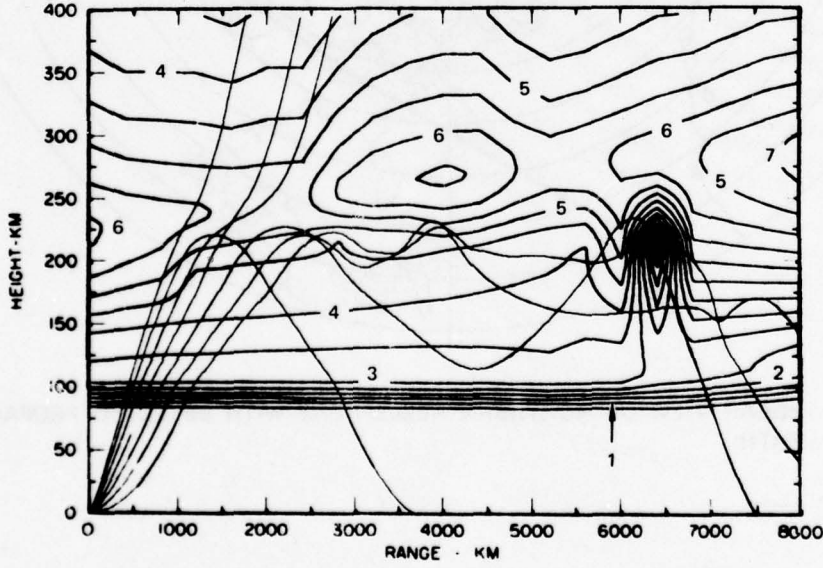


FIGURE 5-3 IONOSPHERIC CONTOURS OF LOCAL PLASMA FREQUENCY (MHz) GENERATED BY THE SRI MODEL FOR THE SELECTED PROPAGATION PATH AT 1800 UT, A SUNSPOT NUMBER OF 50, AND A K_p OF 2. Ray trajectories are indicated.

frequencies are slightly smaller, and the feature at 3500 km distance is absent. Surprisingly, these differences result in the propagation of most of the rays to greater distances.

5.2 Nightside Propagation Path

In order to illustrate the transauroral propagation in the evening sector, rays were traced at 0600 UT on the same date for two values of K_p . The location of the great-circle path and auroral oval are indicated in the plot of geomagnetic local time vs latitude shown in Figure 5-4.

Ionospheric contours for a K_p of 2 are shown in Figure 5-5 and 5-6. In the original ionospheric model all rays are reflected. In the modified model the rays have apogees at higher altitudes because of the reduced value for the nighttime midlatitude auroral E. The lower-elevation rays then reflect off the topside auroral E layer before penetrating over the polar cap. The ray that ends abruptly at ~ 6000 km was deviated outside the azimuthal sector modeled (2° on each side of the great-circle of the great-circle plane).

The ray trajectories for the same conditions except for a K_p of 4 are shown in Figures 5-7 and 5-8. The increased K_p has resulted in a wider and more dense nighttime auroral E layer. Once again the rays in the original ionospheric model are simply reflected. In the modified ionospheric model the rays launched at higher elevation angles are ducted before penetrating.

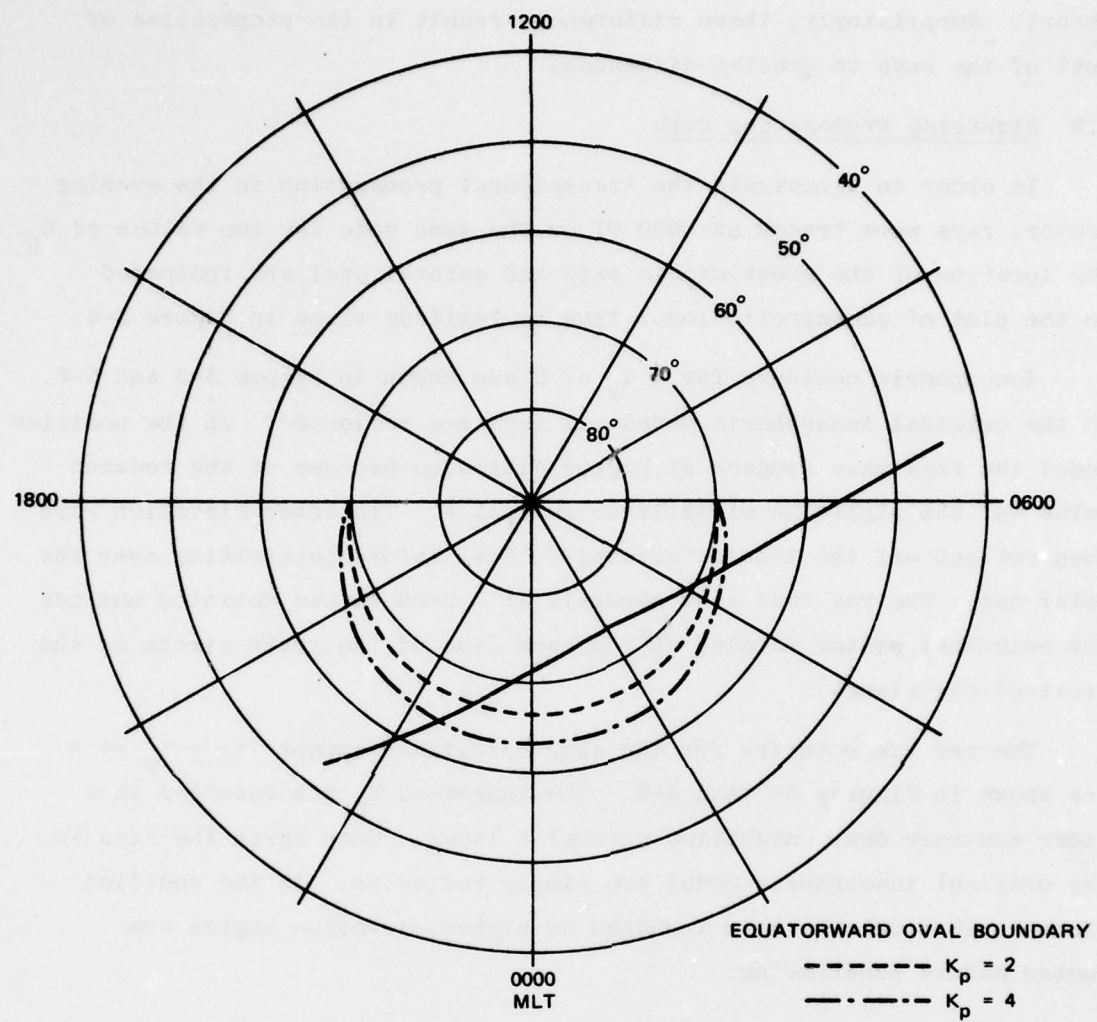


FIGURE 5-4 PROPAGATION PATH IN FIGURE 5-1 PLOTTED IN COORDINATES OF CORRECTED GEOMAGNETIC LATITUDE AND LOCAL TIME

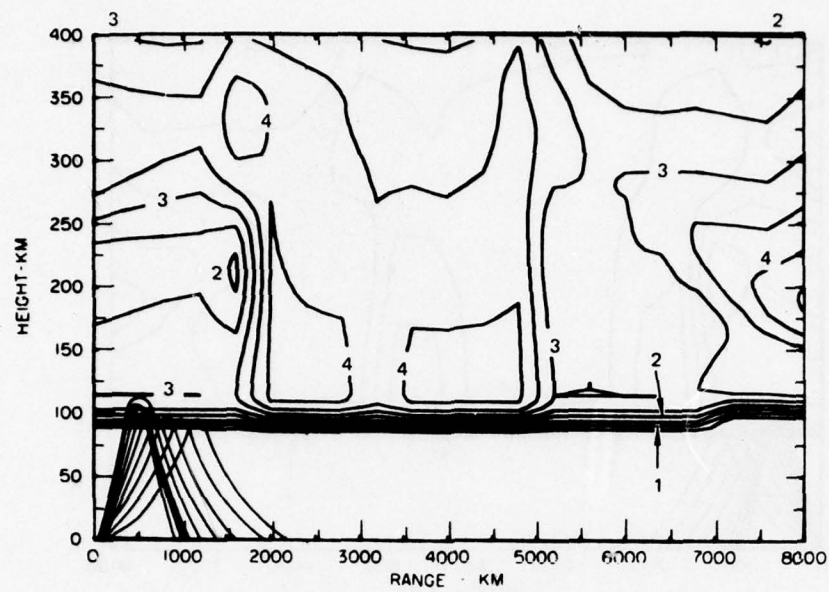


FIGURE 5-5 IONOSPHERIC CONTOURS OF LOCAL PLASMA FREQUENCY (MHz) GENERATED BY THE RADC MODEL FOR THE SELECTED PROPAGATION PATH AT 0600 UT, A SUNSPOT NUMBER OF 50, AND A K_p OF 2. Ray trajectories are indicated.

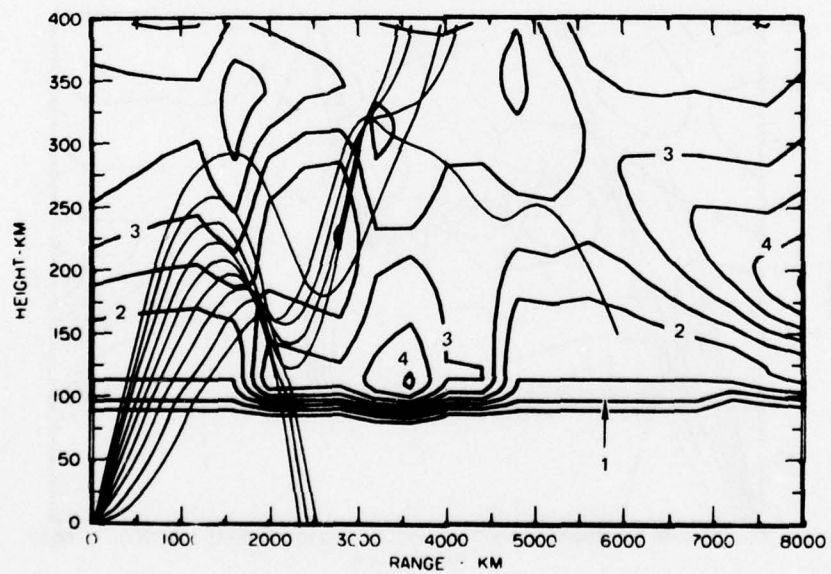


FIGURE 5-6 IONOSPHERIC CONTOURS OF LOCAL PLASMA FREQUENCY (MHz) GENERATED BY THE SRI MODEL FOR THE SELECTED PROPAGATION PATH AT 0600 UT, A SUNSPOT NUMBER OF 50, AND A K_p OF 2. Ray trajectories are indicated.

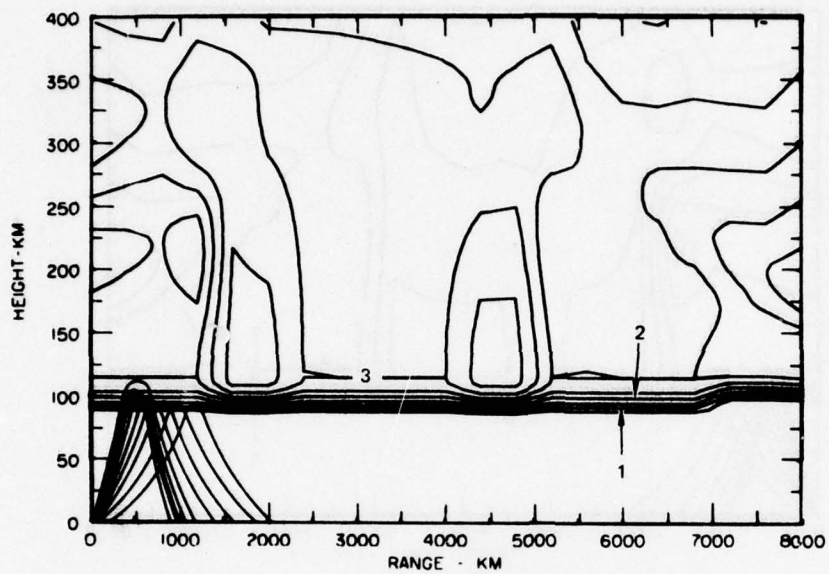


FIGURE 5-7 IONOSPHERIC CONTOURS OF LOCAL PLASMA FREQUENCY (MHz) GENERATED BY THE RADC MODEL FOR THE SELECTED PROPAGATION PATH AT 0600 UT, A SUNSPOT NUMBER OF 50, AND A K_p OF 4. Ray trajectories are indicated.

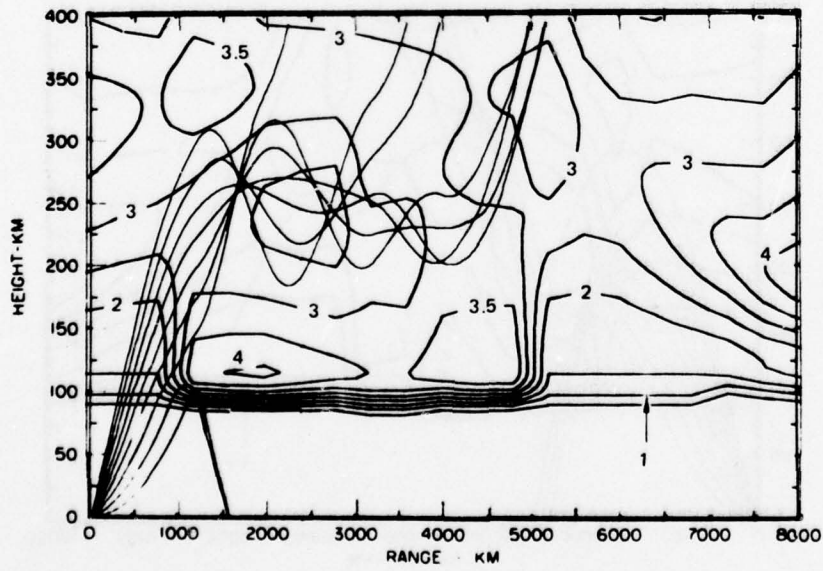


FIGURE 5-8 IONOSPHERIC CONTOURS OF LOCAL PLASMA FREQUENCY (MHz) GENERATED BY THE SRI MODEL FOR THE SELECTED PROPAGATION PATH AT 0600 UT, A SUNSPOT NUMBER OF 50, AND A K_p OF 4. Ray trajectories are indicated.

6. AURORAL ABSORPTION MODEL

As a separate and quite independent task, we have developed a new model of auroral absorption that has an explicit dependence on magnetic activity. Our objective was to employ the same frame of reference, and a comparable degree of averaging, as that used in the model of the E and F regions in order to ensure consistency between the computed raypaths and the corresponding absorption estimates. The rationale for development of such a model is discussed in this section, together with an analytic definition of the model itself.

6.1 Background

The model of the auroral ionosphere described in the preceding sections does not include the D region, where most of the absorption of HF signals occurs. Neither the vertical-incidence-ionosonde technique nor the Chathanika radar can provide the data needed to develop such a model, because the electron densities in the D region are normally too small to produce a measurable signal. Only in rare instances of extreme magnetic activity (such as the great magnetic storm of August 1972) can the radar measure D-region profiles. Such data are extremely valuable to aeronomers as a source of information on the physics and chemistry of the lower ionosphere, but they are clearly not sufficient for development of a synoptic model. Although other techniques have been used to measure D-region profiles under more normal conditions, these data are also too sparse for general model development.

On the other hand, the lack of a D-region model is not a serious deficiency in an ionospheric model intended for use in HF raytracing. Because of the relatively high collision frequency between electrons and neutral particles at these altitudes, the presence of free electrons in the D region affects only the strength of the signal, and not its direction of propagation. For this reason, absorption that occurs in the

D region is called "nondeviative." The customary procedure in HF raytracing calculations is first to determine the raypaths by using a model of the E and F regions, and then to estimate the absorption at the locations where the computed rays pass through the D region. By this procedure, a model of the spatial and temporal variations of absorption can be incorporated directly into the raytracing code, thereby eliminating the need for a D-region model.

In contrast to the difficulties inherent in measurement of D-region profiles, absorption is measured routinely at numerous locations by the relatively simple riometer technique. A riometer measures the variations in cosmic radio noise that has penetrated the ionosphere. Since the cosmic radio flux is constant over long periods of time, any changes in intensity from one day to another at the same sidereal time can be interpreted as variations in ionospheric absorption. After correction for antenna beamwidth and refractive effects, the result is a direct measure of one-way vertical absorption at the observing frequency. The values can be normalized to the frequency of interest through the inverse-frequency-squared dependence of nondeviative absorption.

Riometer measurements constitute a large data base from which a number of synoptic models of absorption have been developed. These models have proven quite adequate for predictions at low and midlatitudes, where absorption is under solar control. Two additional types of absorption occur at high latitudes: polar-cap absorption and auroral absorption. We are concerned here only with auroral absorption, which is caused by the precipitation of energetic electrons in and near the auroral oval.

A model of auroral absorption developed by Foppiano (1975) has recently been adopted (after some minor but significant modifications) by CCIR (1976). This is a model of monthly median absorption that combines the effects of substorms occurring over an entire month at a given hour of the day and for a given level of solar activity (specified by the 12-month running-average sunspot number). Although the median absorption is implicitly related to magnetic activity through its dependence on sunspot number, the model does not have an explicit

dependence on magnetic activity. Consequently, the large increases in auroral absorption associated with intense magnetic activity tend to be obscured in the averaging process. Conversely, a few large substorms may contaminate the quiet-day predictions. This model is, therefore, not appropriate for use with an HF raytracing code in which the structure of the refracting regions is defined as a function of magnetic activity in a three-hour time frame.

An auroral absorption model developed by Hargreaves (1966) has an explicit dependence on K_p . However, because Hargreaves was seeking a relationship between the solar wind and auroral absorption on a global scale, his data have been ordered according to universal time. That is, data from several time sectors have been combined, thereby obscuring diurnal effects, which are as important as magnetic effects for our purposes.

The auroral absorption model developed by SRI follows Foppiano's formulation closely, while incorporating an average magnetic dependence derived from Hargreaves' curves. The final calibration is made by matching the magnitude of the absorption to a third model given by Basler (1963). Because these three models are crucial to the development of the SRI model, their principal features are summarized below.

6.2 Review of Existing Models

The three auroral absorption models reviewed here are: the Foppiano model, the Hargreaves model, and the Basler model. They are all developed in terms of median absorption at approximately 30 MHz and are all empirical models based on riometer data.

6.2.1 The Foppiano Model

The description given below of the model developed by Foppiano is essentially that found in CCIR (1976).

Foppiano developed his model by fitting equations to published riometer data from 27 stations in the Northern hemisphere to indicate the spatial and temporal variations of the auroral absorption. Mapping is in terms of a coordinate system of corrected geomagnetic latitude

φ , corrected geomagnetic longitude, θ , and corrected geomagnetic local time, T . The percentage probability, Q_1 , that the absorption measured at 30 MHz exceeds 1 dB for a riometer with an antenna pointing at the zenith, is given as the sum of two separate terms, Q_{1d} and Q_{1s} . Those terms correspond, respectively, to absorption contributions that are assumed to arise from two different sorts of incident auroral particles, referred to as "drizzle" and "splash" (Hartz and Brice, 1967). Since the sources, energies, and incident directions of these particles differ, the two terms have different spatial and temporal statistics.

Empirical equations based in part on the known particle statistics and on riometer data give

$$Q_1 = Q_{1d} + Q_{1s} \quad (6-1)$$

with

$$Q_{1d} = 21 d_{\varphi} \cdot d_T \cdot d_R \cdot d_{\theta} \cdot d_M \quad (6-2)$$

and

$$Q_{1s} = 12 s_{\varphi} \cdot s_T \cdot s_R \cdot s_{\theta} \cdot s_M \quad (6-3)$$

The subscripts φ , T , R , θ and M relate to terms which have a principal dependence on latitude, time of day, solar activity, longitude and season, respectively. The terms are given in Eqs. (6-4) through (6-13):

$$d_{\varphi} = \exp \left[\frac{- (\varphi - \varphi_m)^2}{2 \sigma_{\varphi}^2} \right] \text{ with } \varphi \text{ in degrees} \quad (6-4)$$

where $\varphi_m = 68 (1 - 0.0004 R_{12})$, in degrees, and $\sigma_{\varphi} = 3 (1 + 0.004 R_{12})$, in degrees. R_{12} is the 12 month running mean sunspot number.

$$d_T = \exp \frac{- (t_1 - T_m)^2}{15.7} \quad (6-5)$$

where $T_m = 10 (1 - 0.002 R_{12})$, hours

T is in hours in the range 0 to 24 such that:

$$t_1 = T \text{ for } 0 \leq T \leq (12 + T_m)$$

$$t_1 = T - 24 \text{ for } (12 + T_m) < T < 24$$

$$d_R = 1 + 0.014 R_{12} \quad (6-6)$$

$$d_\theta = \begin{cases} 0.58 - 0.42 \sin [0.947 (\theta + 85^\circ)] & \text{for } 0 \leq \theta < 10 \\ 0.16 & \text{for } 10 < \theta < 80 \\ 0.58 + 0.42 \sin [1.80 (\theta - 130^\circ)] & \text{for } 80 \leq \theta < 180 \\ 0.58 - 0.42 \sin [0.947 (\theta - 275^\circ)] & \text{for } 180 \leq \theta < 360 \end{cases} \quad (6-7)$$

where θ is in degrees in the range 0-360.

$$d_m = 1 - 0.3 \sin 3.86 \delta \quad (6-8)$$

where δ is the mean solar declination for the month

$$s_\varphi = \exp \left[- \frac{(\varphi - \varphi'_m)^2}{2 \sigma_\varphi^2} \right] \quad (6-9)$$

where $\varphi'_m = 67 (1 - 0.0006 R_{12}) + 0.3 (1 + 0.012 R_{12}) |t|$, deg.

$$t = T - 3 \text{ for } 0 \leq T \leq 15$$

$$t = T - 27 \text{ for } 15 < T < 24 .$$

$$s_T = \exp \left[- \frac{t_2^2}{15.7} \right] \quad (6-10)$$

where $t_2 = T \text{ for } 0 \leq T \leq 12$

$$t_2 = T - 24 \text{ for } 12 < T < 24 .$$

$$s_R = 1 + 0.009 R_{12} . \quad (6-11)$$

$$s_\theta = d_\theta . \quad (6-12)$$

$$s_m = 1 . \quad (6-13)$$

Riometer data are found to follow approximately a fixed relationship between Q_1 and A_m , the median absorption. With Q_1 as a percentage and A_m in decibels

$$A_m = \begin{cases} \frac{Q_1 + 30}{80}^{1.54} & \text{for } Q_1 \geq 1 \\ 0.23 Q_1^{0.2} & \text{for } Q_1 < 1 \end{cases} \quad (6-14)$$

6.2.2 The Hargreaves Model

The data for the Hargreaves Model came from six stations during the period April 1963 through March 1964, as shown in Table 6-1.

Table 6-1
RIOMETER STATIONS FOR HARGREAVES' MODEL

Station	Geographic Position	Geomagnetic Latitude	Invariant Latitude	L-Value	Riometer Frequency (MHz)
South Pole	90°00'S, -	78.6°S			26.50
Frobisher Bay	63°48'N, 68°42'W	75.2°N	74.5°	14	29.85
Byrd	80°01'S, 119°32'W	70.6°S			29.85
Great Whale River	55°20'N, 77°50'W	66.6°N	67.8°	7	29.85
Eights	75°15'S, 77°10'W	63.9°S			29.85
Baie St. Paul	47°22'N, 70°33'W	58.8°N	60.0°	4	29.85

The median absorption is assumed to have a Gaussian distribution:

$$A_m = A_o \exp \left[- \frac{(\lambda - \lambda_o)^2}{2 \sigma_2^2} \right] \quad (6-15)$$

where the magnitude, A_o , the latitude of maximum absorption, λ_o , and the width of the absorbing region, σ_2 , are found from empirical curves that relate absorption to magnetic activity (K_p) and universal time.

Hargreaves gives the following formula for conversion between A_m and Q_1 (expressed as a percentage):

$$Q_1 = 2200 A_m^{3.5} \quad (6-16)$$

6.2.3 The Basler Model

The model developed by Basler (1963; private communication, 1977) is based on riometer data recorded at a chain of Alaskan observing stations over a five-year period (1957-1962) during a declining phase of solar activity--i.e., from sunspot maximum to sunspot minimum. Median absorption, A_m , in dB is determined from

$$A_m = A(\text{season, hour}) \cdot B(\text{geomagnetic latitude}).$$

The first coefficient, A , is found for a given season (i.e., winter, summer, and equinox) and local time from a table of values derived from measurements at College. The assumption is made that the maximum always occurs at 65° geomagnetic latitude (i.e., near College), and that auroral absorption occurs only in a region extending 10° on either side of the peak. The second coefficient, B , is a triangular function that approximates the geomagnetic latitude variation.

The median absorption values making up the table of coefficients, A , were derived from the College data (Basler, 1963). These values have had corrections applied that make them directly applicable for use in estimating one-way vertical absorption. The data have been corrected for the effect of the broad-beam riometer antenna assuming a uniform distribution of cosmic-noise intensity over the antenna pattern, a horizontally uniform and stratified absorbing layer, and a cosine-squared polar diagram for the three-element Yagi antenna. Corrections were also made to remove the small effect of spurious absorption produced when the cosmic noise is reflected from the F layer and sporadic-E ionization. These data will be used for calibrating A_m in our final model.

The composite ΣK_p for 1957-1962 was about 21 (average K_p of 2.6). Basler suggests providing a K_p dependence by multiplying A_m by the ratio of $\Sigma K_p/21$. We have estimated that the average sunspot number for this period was 120.

6.3 The SRI Model

The formulation of the model is accomplished in three distinct steps. First, we modify Foppiano's equations that define the spatial and temporal locations of the absorbing regions, converting their dependence on sunspot number to a dependence on K_p ; the magnitude of the maximum absorption is not altered in this step. Next, we convert Q_1 to A_m , where A_m continues to represent the monthly median value because the magnitude of Q_1 remains unchanged. A new conversion formula is derived that fits the data better than does Foppiano's. Finally, the magnitude of the absorption is expressed as a function of K_p by multiplying the monthly median, A_m , by a factor derived from Hargreaves' and Basler's data.

6.3.1 Definition of Absorbing Regions

The expression for Q_1 , Q_{1d} , and Q_{1s} [Eqs. (6-1) through (6-3)] from Foppiano's model are incorporated in the SRI model without change. However, the factors d_φ , s_φ , d_T , and s_T are redefined in the SRI model to reflect a dependence on K_p rather than on R_{12} . We first observe that these factors are Gaussian functions that have been normalized to their respective maxima so that the modification does not affect their maximum contributions to Q_1 .

In Eq. (6-4) (relating to d_φ), the latitude, φ_m , of maximum absorption and the latitudinal extent, σ_φ , of the absorbing region for drizzle precipitation are redefined as follows:

$$\varphi_m = \begin{cases} 67.864 - 0.6256 K_p, & K_p \leq 5 \\ 75.616 - 2.176 K_p, & K_p > 5 \end{cases} \quad (6-17)$$

$$\sigma_{\varphi} = \begin{cases} 3.06 + .276 K_p, & K_p \leq 5 \\ -.36 + .96 K_p, & K_p > 5 \end{cases} \quad (6-18)$$

Although Hartz (1972) states that there is no latitudinal shift with K_p in the drizzle zone, the above equations correspond to those given in Eq. (6-4).

For the splash zone, the corresponding modifications of s_{φ} [Eq. (6-9)] are:

$$\varphi'_m = \begin{cases} 66.799 - 0.9246 K_p + (0.318 + 0.0828 K_p) |t| & ; K_p \leq 5 \\ 78.256 - 3.216 K_p + (.288 K_p - .708) |t| & ; K_p > 5 \end{cases} \quad (6-19)$$

$t = T - 3$ for $0 \leq T \leq 15$

$t = T - 27$ for $15 < T < 24$

T = corrected geomagnetic local time (CGT).

Maximum absorption in the splash zone occurs at 2300 CGT. The width of the splash zone is defined by σ_{φ} [Eq. (6-18)], identical to that of the drizzle zone.

The only other factors of Eq. (6-1) that have been altered are d_T and s_T , the times of maximum drizzle and splash precipitation. For drizzle, the value of T_m in Eq. (6-5) is changed to

$$T_m = \begin{cases} 9.9 - 0.46 K_p & \text{for } K_p \leq 5 \\ 15.6 - 1.6 K_p & \text{for } K_p > 5. \end{cases} \quad (6-20)$$

For a K_p of 4 this zone is centered around 0800 as Hartz (1972) suggests. For lower K_p values this zone peaks later and for higher K_p it peaks earlier. The time of maximum splash precipitation has been changed to 2300 CGT, as recommended by Hartz. Equation (6-10) is modified as follows:

$$t_2 = \begin{cases} T + 1 & 0 \leq T \leq 11 \\ T - 24 & 11 < T < 24. \end{cases} \quad (6-21)$$

It should be noticed that the factors d_R and s_R , which express a direct dependence on solar activity, have not been altered.

6.3.2 Conversion from Q_1 to A_m

From the above expressions the value of Q_1 can be calculated. The conversion from Q_1 to the monthly median value of A_m remains to be explained. The conversion factors given by Foppiano and Hargreaves differ substantially, as shown in Figure 6-1. In addition to the curves of Q_1 versus A_m , the figure shows Hargreave's data and four additional points derived from Basler's data. Foppiano's values of A_m are larger than the data seem to imply. Hargreaves' curve matches the data quite well up to $Q = 10$, above which we had no data for comparison; however, the maximum value that A_m can attain is 0.41 dB (for $Q_1 = 100$), which is clearly not reasonable in view of the definition of Q_1 . (Hargreaves cautions against extrapolating his expression beyond its range of applicability.) Therefore, we have accepted Hargreaves' expression as the better fit to the data for $Q_1 \leq 10$. At that point, we have shifted Foppiano's curve to match Hargreaves', continuing thereafter with Foppiano's shifted curve.

The resulting conversion equations are:

$$A_m = \begin{cases} \left(\frac{Q_1}{2200} \right)^{\frac{1}{3.5}} & Q \leq 10 \\ \frac{1}{1.6057} \left(\frac{Q_1 + 30}{80} \right)^{1.54} & Q > 10. \end{cases} \quad (6-22)$$

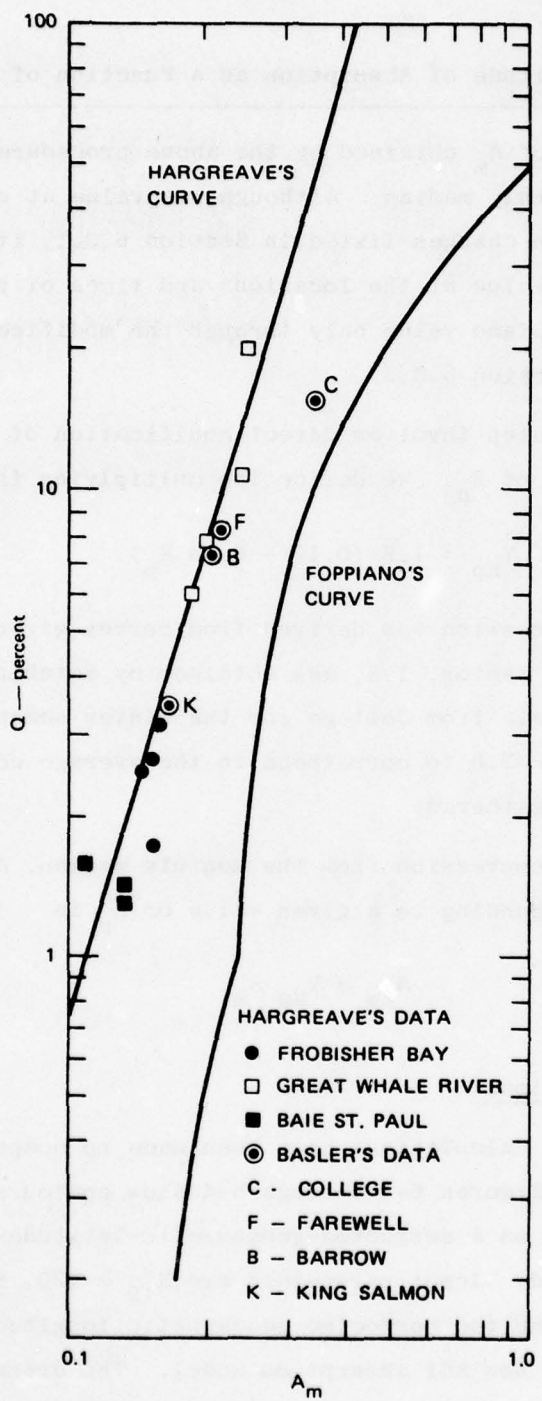


FIGURE 6-1 COMPARISON OF METHODS OF CONVERTING THE PROBABILITY, Q, THAT ABSORPTION MEASURED AT 30 MHz EXCEEDS 1 dB, TO MEDIAN ABSORPTION, A_m

6.3.3 The Magnitude of Absorption as a Function of K_p

The value of A_m obtained by the above procedure can still be interpreted as a monthly median. Although its value at a given location may be altered by the changes listed in Section 6.3.1, its maximum value--that is, its value at the locations and times of peak absorption--differs from the Foppiano value only through the modified conversion equation given in Section 6.3.2.

The final step involves direct modification of A_m by multiplication with a function of K_p . We define the multiplying factor as

$$Y_{Kp} = 1.8 (0.17 + 0.14 K_p). \quad (6-23)$$

The form of this expression was derived from curves given by Hargreaves (1966). The scaling factor, 1.8, was obtained by matching the computed values to Basler's data from College for the winter season, using values of $R_{12} = 120$ and $K_p = 2.6$ to correspond to the average conditions under which the data were gathered.

The final conversion from the monthly median, A_m , to the 3-hour median corresponding to a given value of K_p is

$$A_{Kp} = Y_{Kp} A_m. \quad (6-24)$$

6.4 Sample Calculations

Several sets of calculations have been made to compare the new model with other models. Figures 6-2 through 6-4 show contours of median absorption at 30 MHz on a corrected-geomagnetic-latitude/corrected-geomagnetic-time grid. Input parameters are $R_{12} = 120$, $K_p = 2.6$, the month of December, and the corrected geomagnetic longitude of College. Figure 6-2 shows the new SRI absorption model. The drizzle and splash peaks are both visible, having values of 0.59 and 0.27, respectively. The Basler model is shown in Figure 6-3. The peaks in this case are 0.6 and 0.3. In the Foppiano model (Figure 6-4), the peaks are 0.95 and 0.4. Foppiano's model also shows higher absorption in the polar-cap region in the afternoon sector.

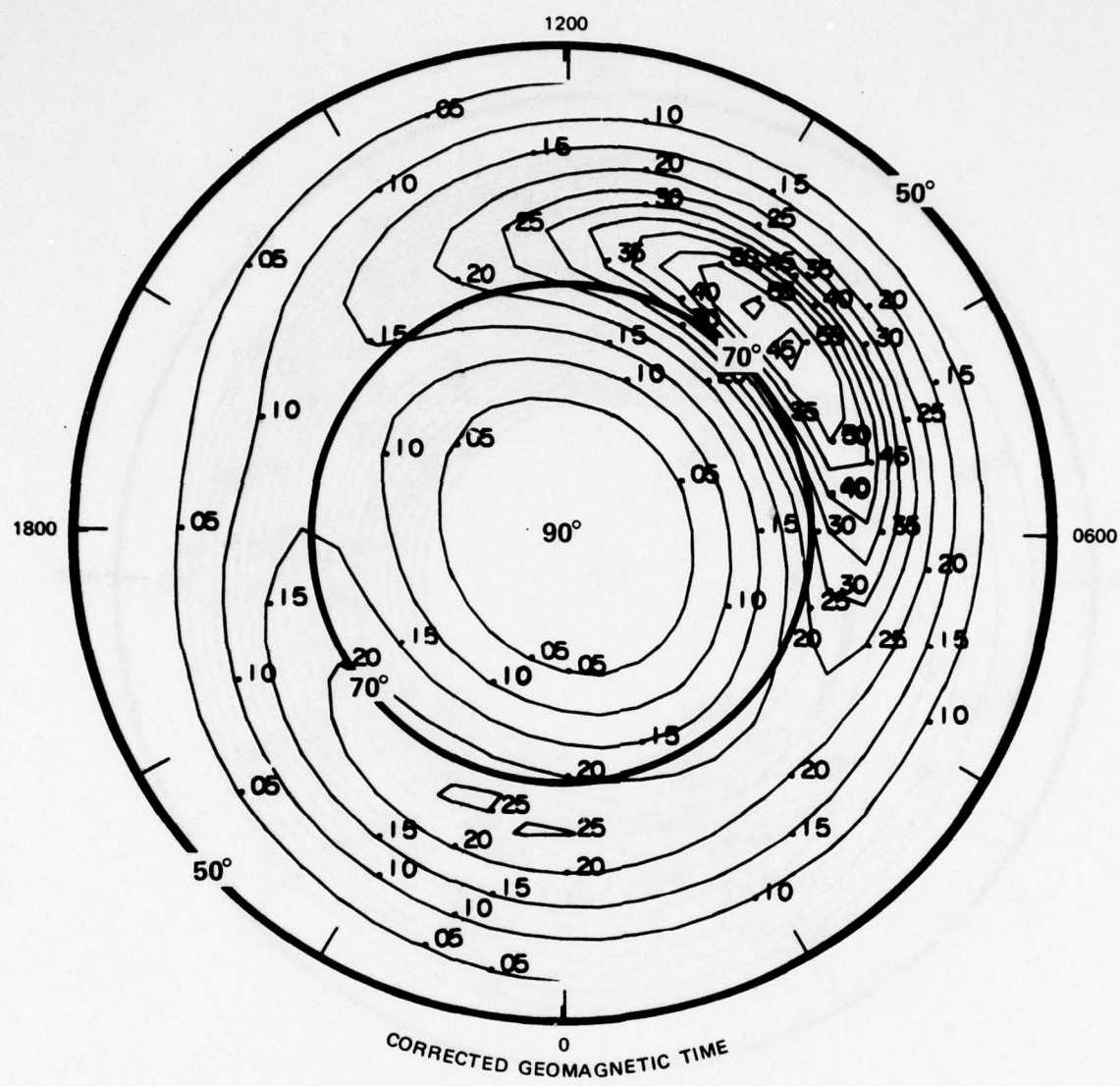


FIGURE 6-2 CONTOURS OF MEDIAN ONE-WAY VERTICAL ABSORPTION IN dB AT 30 MHz ON A PLOT OF CORRECTED GEOMAGNETIC LATITUDE vs CORRECTED GEOMAGNETIC TIME, USING THE SRI ABSORPTION MODEL. Corrected geomagnetic longitude, 260°; sunspot number, 120; month, 12; $K_p = 2.6$.

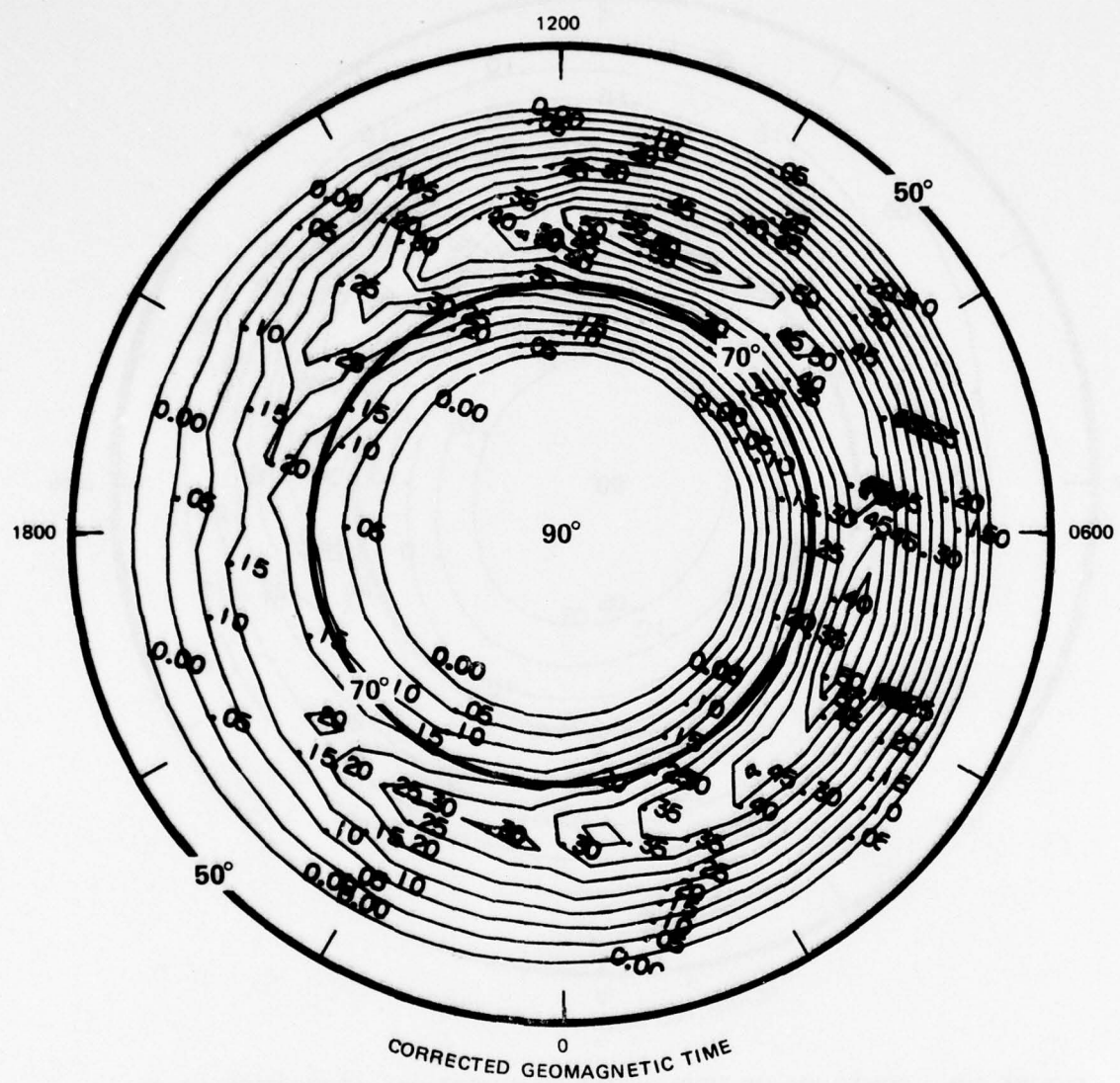


FIGURE 6-3 CONTOURS OF MEDIAN ONE-WAY VERTICAL ABSORPTION IN dB AT 30 MHz ON A CORRECTED GEOMAGNETIC LATITUDE-CORRECTED GEOMAGNETIC TIME GRID, USING THE BASLER MODEL. Corrected geomagnetic longitude, 260° ; sunspot number, 120; month, 12; $K_p = 2.6$.

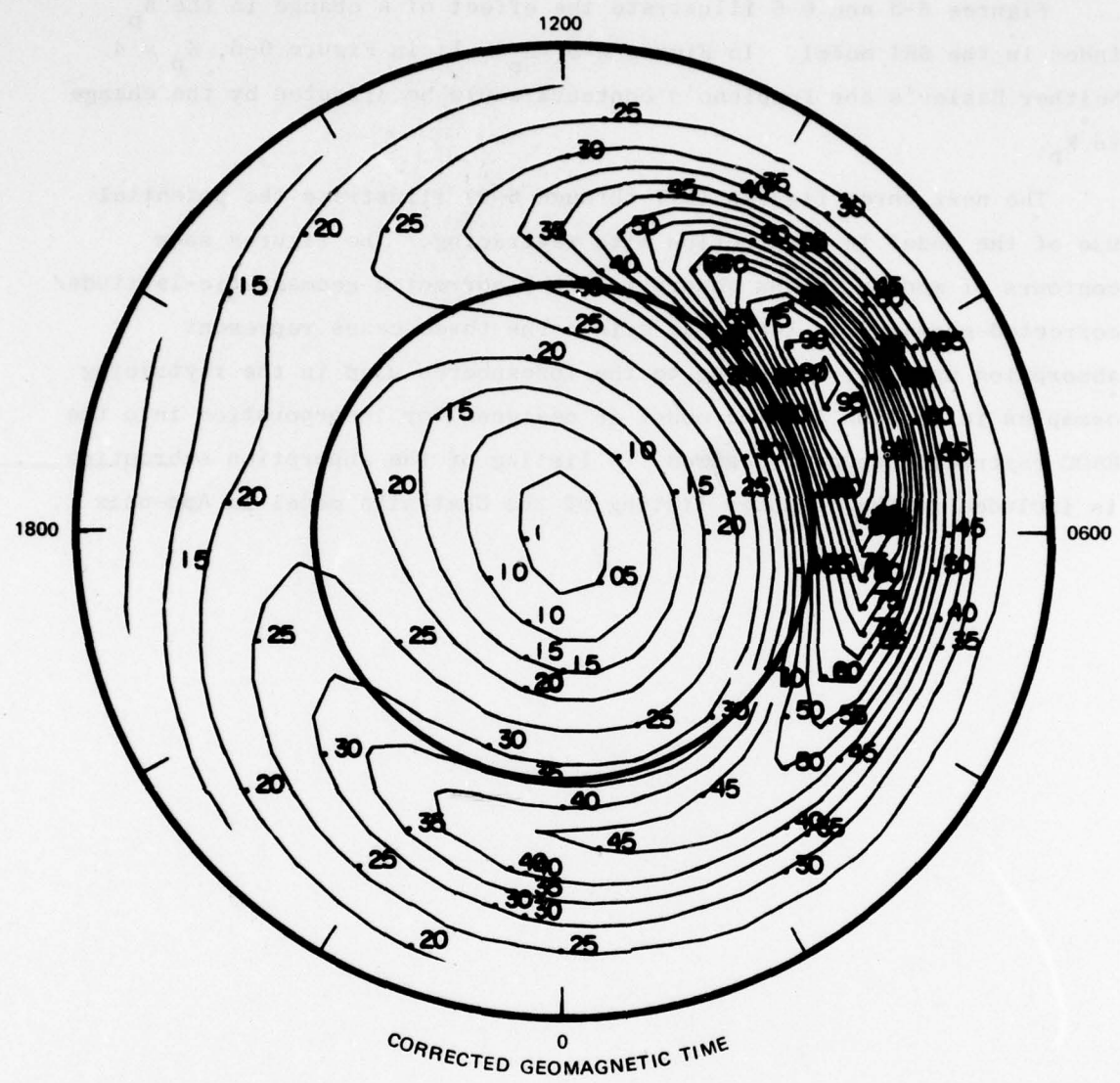


FIGURE 6-4 CONTOURS OF MEDIAN ONE-WAY VERTICAL ABSORPTION IN dB AT 30 MHz ON A CORRECTED GEOMAGNETIC LATITUDE-CORRECTED GEOMAGNETIC TIME GRID, USING THE FOPPIANO MODEL. Corrected geomagnetic longitude, 260° ; sunspot number, 120; month, 12; $K_p = 2.6$.

Figures 6-5 and 6-6 illustrate the effect of a change in the K_p index in the SRI model. In Figure 6-5, $K_p = 1$; in Figure 6-6, $K_p = 4$. Neither Basler's nor Foppiano's contours would be affected by the change in K_p .

The next three figures (6-7 through 6-9) illustrate the potential use of the model in conjunction with raytracing. The figures show contours of median 30-MHz absorption on a corrected-geomagnetic-latitude/corrected-geomagnetic-longitude grid. The three cases represent absorption maps corresponding to the ionospheres used in the raytracing examples in Section 5. The model is designed for incorporation into the RADC raytracing code if desired. A listing of the absorption subroutine is included in the computer listing of the Chatanika model in Appendix C.

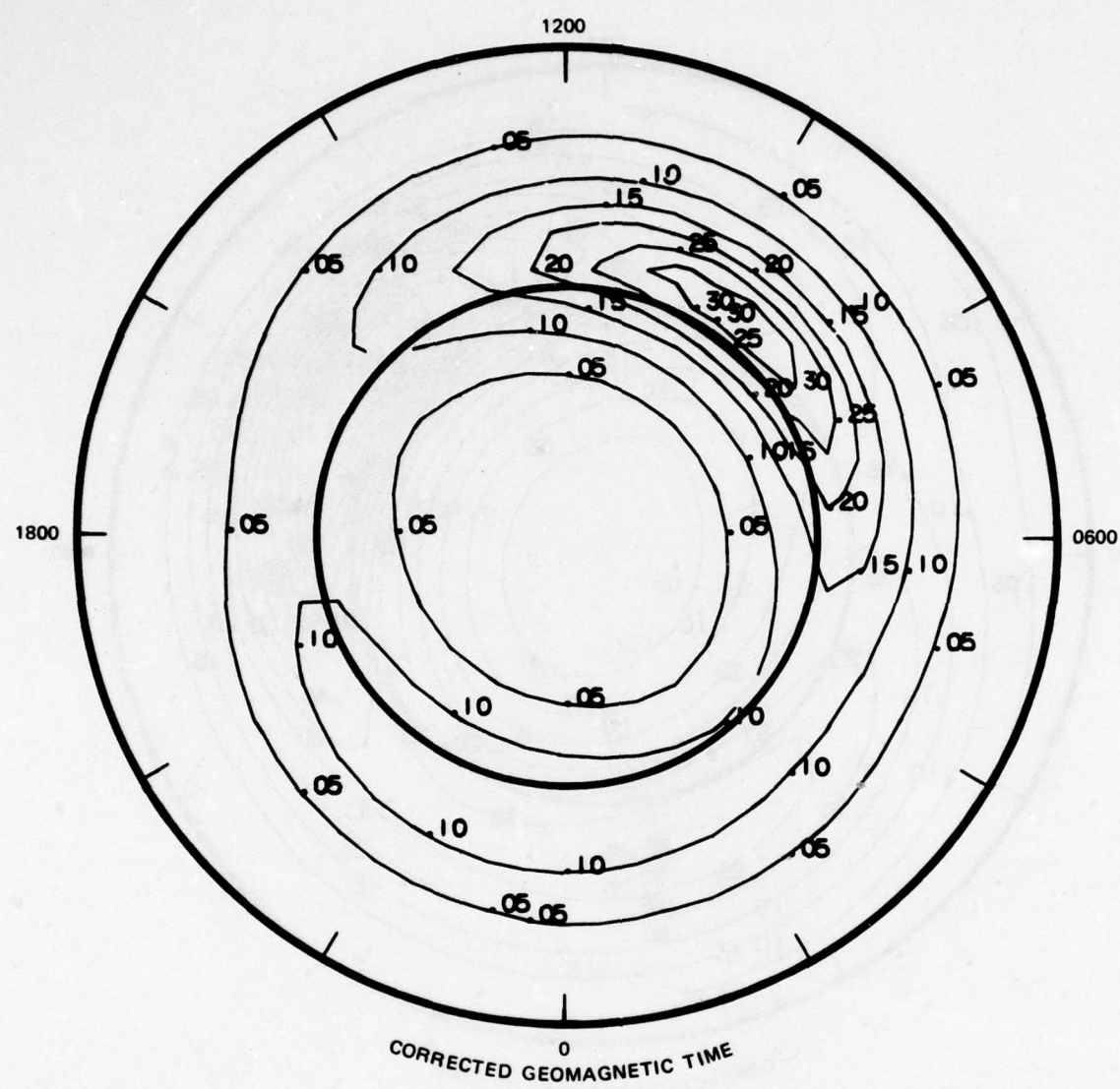


FIGURE 6-5 CONTOURS OF MEDIAN ONE-WAY VERTICAL ABSORPTION IN dB AT 30 MHz ON A CORRECTED GEOMAGNETIC LATITUDE-CORRECTED GEOMAGNETIC TIME GRID, USING A LOW K_p ($K_p = 1$). Corrected geomagnetic longitude, 260° ; sunspot number 120; month, 12; SRI absorption model.

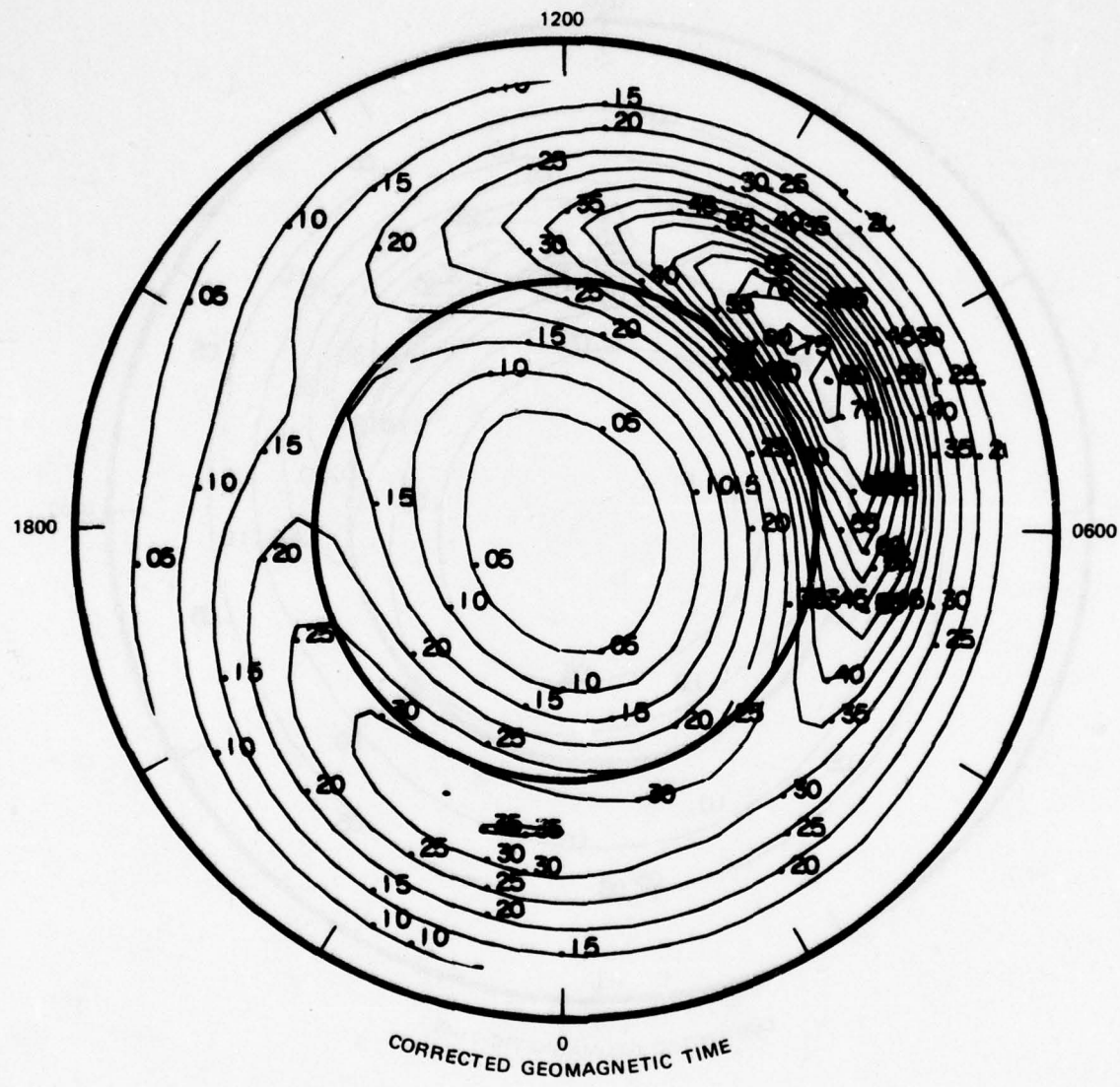


FIGURE 6-6 CONTOURS OF MEDIAN ONE-WAY VERTICAL ABSORPTION IN dB AT 30 MHz ON A CORRECTED GEOMAGNETIC LATITUDE-CORRECTED GEOMAGNETIC TIME GRID, USING A HIGH K_p ($K_p = 4$). Corrected geomagnetic longitude, 260°; sunspot number 120; month, 12; SRI absorption model.

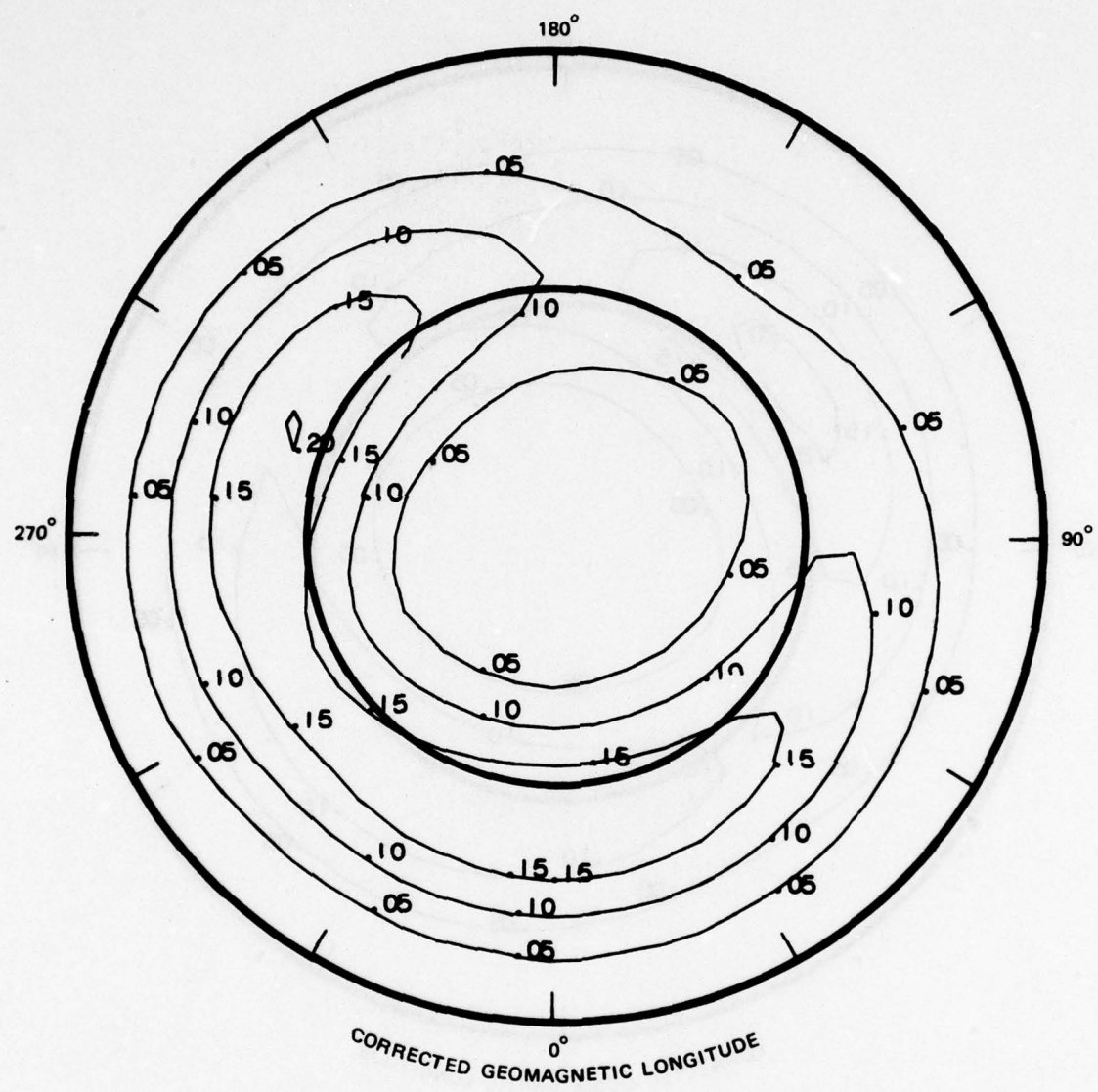


FIGURE 6-7 CONTOURS OF MEDIAN ONE-WAY VERTICAL ABSORPTION IN dB
 AT 30 MHz ON A CORRECTED GEOMAGNETIC LATITUDE-CORRECTED
 GEOMAGNETIC LONGITUDE GRID FOR THE DAYSIDE PATH, WITH
 $K_p = 2$. Sunspot number, 50; month, 4; 1800 UT.

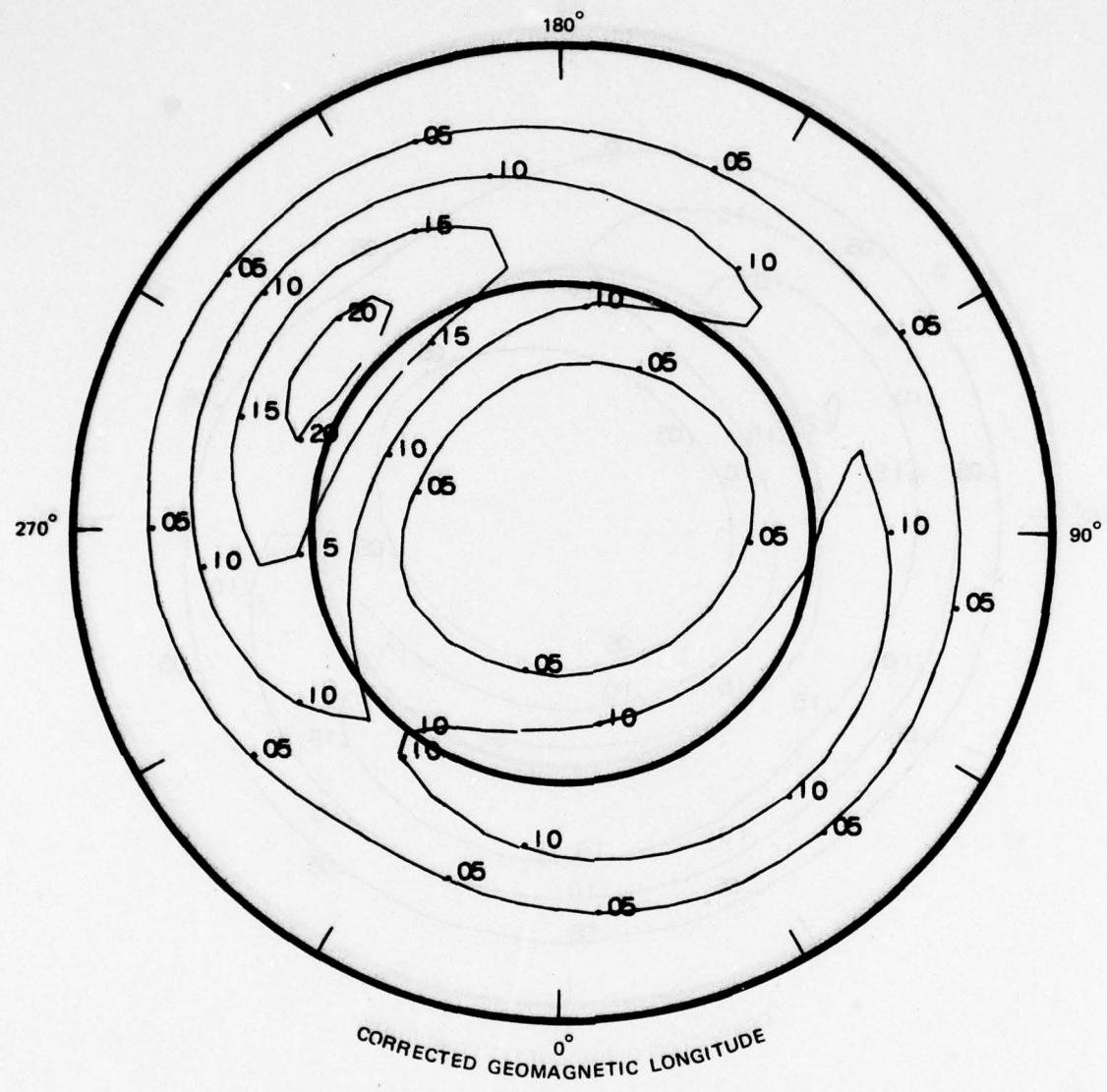


FIGURE 6-8 CONTOURS OF MEDIAN ONE-WAY VERTICAL ABSORPTION IN dB
AT 30 MHz ON A CORRECTED GEOMAGNETIC LATITUDE-CORRECTED
GEOMAGNETIC LONGITUDE GRID FOR THE NIGHTSIDE PATH, WITH
 $K_p = 2$. Sunspot number, 50; month, 4; 0600 UT.

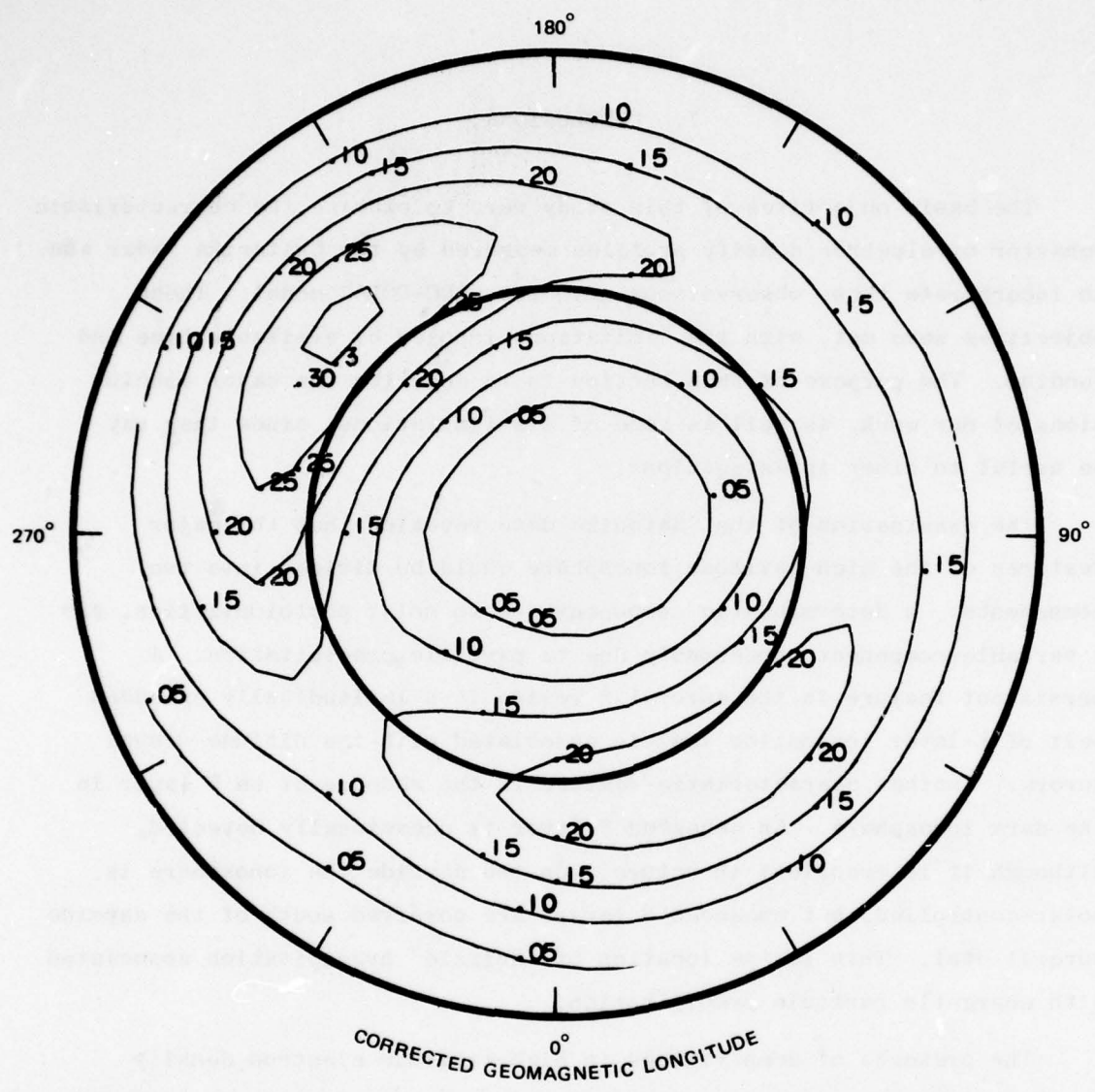


FIGURE 6-9 CONTOURS OF MEDIAN ONE-WAY VERTICAL ABSORPTION IN dB AT 30 MHz ON A CORRECTED GEOMAGNETIC LATITUDE-CORRECTED GEOMAGNETIC LONGITUDE GRID FOR THE NIGHTSIDE PATH, WITH $K_p = 4$. Sunspot number, 50; month, 3; 0600 UT.

7. CONCLUSIONS

The basic objectives of this study were to examine the characteristic behavior of electron density profiles measured by the Chatanika radar and to incorporate these observations into the RADC-POLAR model. These objectives were met, with the limitations imposed by available time and funding. The purpose of this section is to describe the major conclusions of our work, as well as some of its limitations, since they may be useful to other investigations.

The examination of the Chatanika data revealed that the major features of the high-latitude ionosphere could be divided into two components: a deterministic component due to solar photoionization, and a variable component, presumably due to particle precipitation. A persistent feature in the auroral E region is a latitudinally extended belt of E-layer ionization that is associated with the diffuse visual aurora. Another characteristic feature is the absence of an F layer in the dark ionosphere. An enhanced F layer is occasionally detected, although it is transient in nature. On the dayside the ionosphere is solar-controlled, but enhanced E layers are observed south of the dayside auroral oval. This is the location of "drizzle" precipitation associated with energetic particle precipitation.

The presence of deep valleys in high-latitude electron density profiles is expected in two circumstances. The first is in the dayside "drizzle" region and the second is the night sector during the summer. In both cases there would generally be a solar-illuminated F layer and a particle-produced E layer. Elevation-scan observations of the summer sunlit diffuse aurora would be of interest. Unfortunately, such measurements have not yet been attempted.

In our modifications of the RADC-POLAR model we left many of its major formulations unchanged. In particular we did not alter its specification of the F layer. This was because of the much larger data

base of F region measurements used in the RADC model and the use in this study of Chatanika data that were not temperature-corrected. The primary interest of our work was the valley and E-region where temperature corrections are relatively unimportant. If a more detailed study of the auroral F region is made with the Chatanika radar, then it would be advisable to include temperature corrections.

Another major feature of the RADC model that we did not change was the use of K_p as a determinant of magnetic activity. Our study found that local K is a better indicator of auroral E. However, there is a preference for K_p , because of its widespread use and general availability. We were able to maintain K_p as the determinant by establishing a relationship between K_p and high-latitude K by analysis of one year of geomagnetic data. Presumably, a direct relationship between K_p and auroral E could be established by analysis of a similarly large set of electron density data.

We also reduced the value of the midlatitude nightside "auroral" E from 3.0 MHz to 1.5 MHz. The accuracy of this revision should be verified. Also, the RADC specification of the polar cap and dayside auroral oval (cleft) warrant further study because additional measurements presumably have been made there since the original formulation of the model. None of those regions fell within the scope of this study.

Because of its altitude resolution of 6 to 10 km, the Chatanika radar is unable to detect structures of smaller scale size that may be responsible for sporadic E. Although sporadic E is important to HF propagation, we did not attempt to include it in the model.

Our analysis is similar to that used in the development of the RADC-POLAR model in that both produce statistical mean models. We did not model small-scale (< 100 km) structures or phenomena transient on a time-scale smaller than the 3-hour K_p index. As a result, the features in our model are characteristic of persistent, widespread phenomena, such as the diffuse aurora and the dayside "drizzle" zones. Features such as auroral arcs, the diffuse aurora "boundary feature," and auroral substorms

are not included. However, the use of a local K that varies with latitude and local time for a specified K did result in an auroral ionosphere with more structure than that in the original model, and presumably a more realistic one.

Another similarity between our model and the RADC model is that they are both empirical. A deterministic formulation of the auroral E may be possible and is worth pursuing. It would be necessary to determine the relevant ionospheric, magnetospheric, or interplanetary parameter that specifies the spatial characteristics of the auroral ionosphere. Because many of these parameters (e.g., electric fields, and incoming auroral energy distribution) can be inferred from the Chathanika measurements, the same data set used in this study could form the basis for the formulation of a deterministic model.

Finally, it seems appropriate to test the validity of the raytracing methods by conducting a propagation experiment in which transauroral transmission is measured through an ionosphere observed simultaneously by Chathanika elevation-scan measurements. Also, our model had a large spatial scale size ($\gtrsim 100$ km), similar to that used in conventional raytracing codes. It may be enlightening to examine simulated propagation through an ionosphere specified to the 10-km resolution of the radar measurements to ascertain the importance of discrete structures.

The primary end product of our work is the modified ionospheric model. The major components of it are listed in Appendix C, and a complete operating program is being sent to RADC separate from this report.

Appendix A

TEMPERATURE CORRECTIONS TO CHATANIKA MEASUREMENTS

Appendix A TEMPERATURE CORRECTIONS TO CHATANIKA MEASUREMENTS

As discussed in Section 2.1, the Chatanika measurements of electron density are normally processed under the assumption that the radar cross section is a constant. In fact, the radar cross section depends on the ratios of two ionospheric plasma parameters. The first is the temperature ratio, T_r , the ratio of electron temperature T_e to ion temperature T_i . The second is the Debye length parameter, α , a number linearly proportional to the ratio of the ionospheric Debye length to the transmitted radar wavelength. For the Chatanika radar, α^2 is equal to $13.9 T_e^2 / N$, where T_e is in K, and N is in units of cm^{-3} . The electron density, computed with a value of unity assumed for T_r and with zero assumed for α^2 , is referred to as the uncorrected density, N' . The relation between this density and the true electron density, N , is

$$N = N' (1 + T_r + \alpha^2) (1 + \alpha^2) / 2.$$

Because T_r is generally greater than 1, the uncorrected electron density is generally an underestimate of the true electron density.

In order to correct the measured electron density profiles, one needs altitude profiles of the electron temperatures and ion temperatures. These temperatures can be measured by a detailed analysis of the frequency spectrum of the received signal. Because such an analysis is time-consuming, it is not routinely performed and was not done for the data in this study. However, temperatures have been determined for other studies, and typical profiles are shown in Figure A-1. The correction factors in the E and F regions for these profiles are shown in Figure A-2. In the E region (below 120 km) the electrons and ions are isothermal and the needed correction is less than 20% for densities greater than $5 \times 10^4 \text{ cm}^{-3}$. At higher altitudes the electrons are generally hotter than the ions and the correction factor is larger.

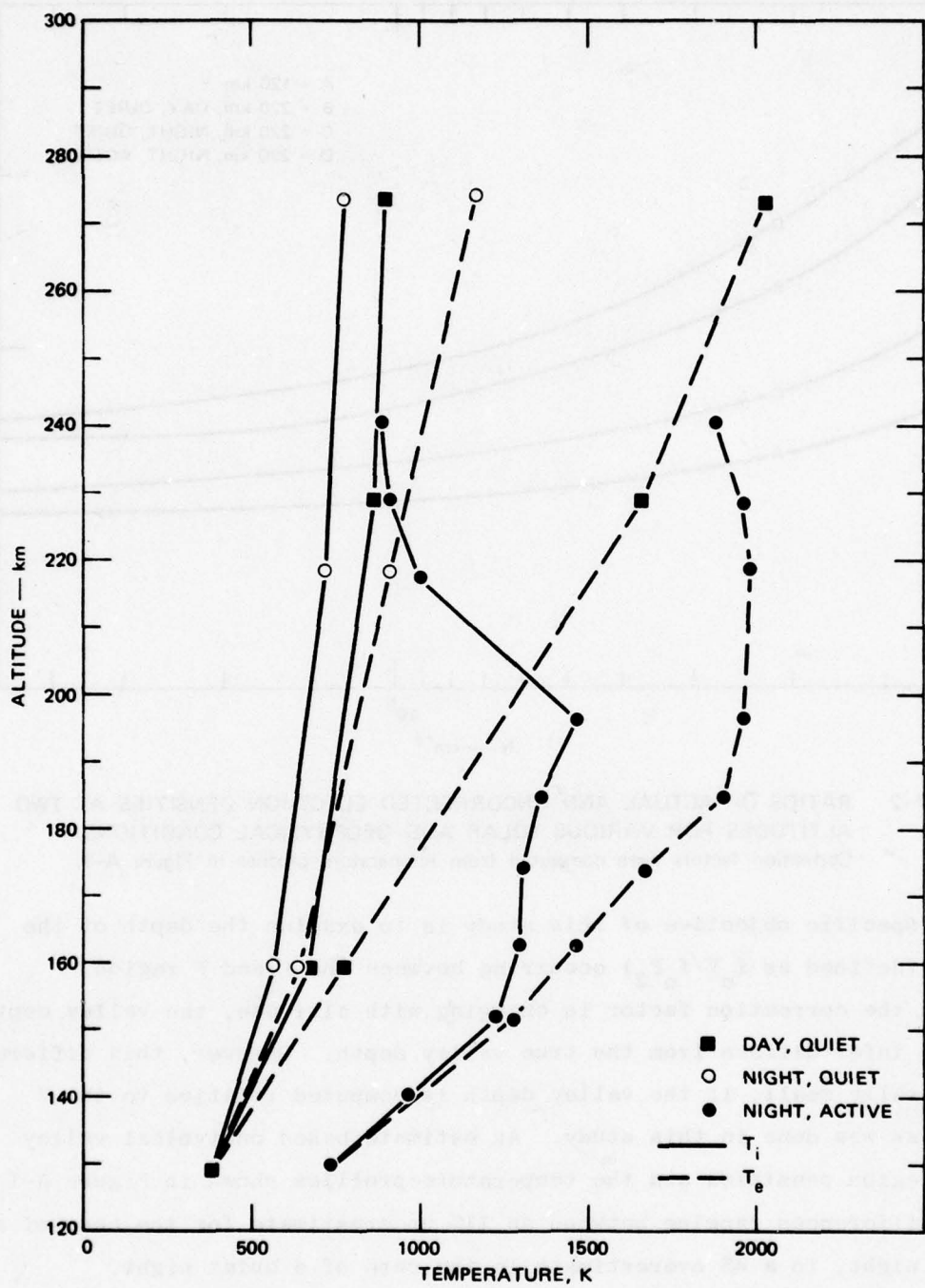


FIGURE A-1 ALTITUDE PROFILES OF ION AND ELECTRON TEMPERATURES FOR VARIOUS SOLAR AND AURORAL CONDITIONS. Data are from Kelly (1977).

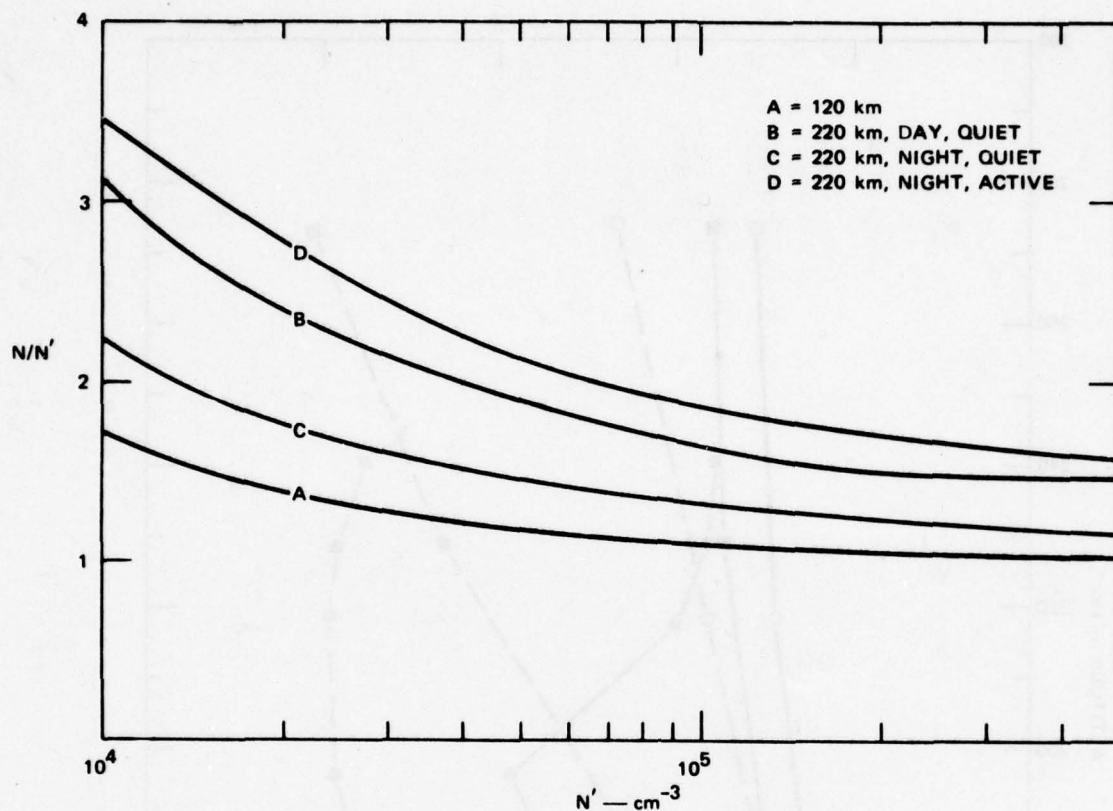


FIGURE A-2 RATIOS OF ACTUAL AND UNCORRECTED ELECTRON DENSITIES AT TWO ALTITUDES FOR VARIOUS SOLAR AND GEOPHYSICAL CONDITIONS.
Correction factors were computed from temperature profiles in Figure A-1.

A specific objective of this study is to examine the depth of the valley (defined as $f_0 V/f_0 F_2$) occurring between the E and F region. Because the correction factor is changing with altitude, the valley depth that we infer differs from the true valley depth. However, this difference is generally small, if the valley depth is computed relative to the F region as was done in this study. An estimate based on typical valley and F-region densities and the temperature profiles shown in Figure A-1 found differences ranging between an 11% underestimate for the case of an active night, to a 4% overestimate in the case of a quiet night.

Appendix B

DIURNAL VARIATION OF HIGH LATITUDE K FOR VARIOUS K_p RANGES

Appendix B

DIURNAL VARIATION OF HIGH-LATITUDE K FOR VARIOUS K_p RANGES

As discussed in Section 4.2, the Chatanika electron-density-profile parameters were found to be better correlated with the local magnetic index, K (College), than with the planetary magnetic index, K_p . In order to retain the use of K_p as the primary magnetic index, it became necessary to establish a relation between it and K at high latitudes. With such a relationship we were able to compute an expected value of K at any desired corrected geomagnetic time and corrected geomagnetic latitude for a given K_p .

Before describing the correlation that we determined, it may be useful to review the meanings of the K and K_p indices. The K index is an indication of the general level of local variation in the geomagnetic field during a 3-hour period. The K-indices are scaled from normal and storm magnetograms. The three component (H, D, Z) records at each station are examined for a 3-hour interval. For each trace an estimate is made of the range during the interval. The largest of the ranges in the H or D traces is taken as the basis for K. The Z component is no longer used. A quantization scale from 0 to 9 with unit intervals is used. The meaning of the scale depends on the latitude.

The K_p index is a measure intended to express the degree of magnetic activity over the whole earth. For this purpose, corrected or standardized values of K (K_s) are prepared from 12 observatories, northern and southern, in moderately high geomagnetic latitudes (see Table B-1). The mean of the K values from the 12 stations is K_p . It is a 3-hour index and is quantized from 0 to 9 in intervals of one-third. Because none of the stations used in compiling the K_p index are in the auroral zone, K_p is primarily a mid-latitude index. It is affected by both the intensity of the ring current and the intensity and location of the electrojet. For this reason K_p is

Table B-1
OBSERVATORIES WHOSE DATA ARE USED IN THE COMPUTATION OF K_p

Observatory	Geomagnetic North Latitude (deg)	Geomagnetic East Longitude (deg)	Comments
Sitka	60.0	275.3	
Meanook	61.8	301.0	
Agincourt	55.1	347.0	Up to 1969
Ottawa	57.0	351.5	Since 1969
Fredricksburg	49.6	349.8	
Hartland	54.6	79.0	
Eskdalemuir	58.5	82.9	
Lerwick	62.5	88.6	
Witteveen	54.1	91.2	
Wingst	54.6	94.1	
Rude Skov	55.9	98.5	
Lovo	58.1	105.8	Since 1954
Amberly	-47.7	252.5	
Toolangi	-46.7	220.8	Since 1972

not a good quantitative indicator of the level of auroral activity. Although it is a poor indicator, it does have some relationship to high-latitude magnetic activity. For example, Rostoker (1972) claims that a large value of K_p ($\geq 2+$) is generally an indicator of substorm activity, yet he also shows that auroral substorms can occur during periods of small K_p .

In order to investigate the relationship between K and K_p , we obtained individual K indices for high-latitude observatories from the World Data Center NOAA. We also obtained K_p indices for the same period of time. Data (both K and K_p) from 1969 to 1974 are available on

magnetic tapes, whereas more recent data is on microfilm and not as readily available for processing. Data from the year 1969 were used in this study.

In 1969 there were 16 stations north of 53° corrected geomagnetic latitude collecting data for K indices. Table B-2 lists the stations used with their code name, geographic coordinates, and corrected geomagnetic coordinates. The best coverage for this year was in the European Sector; the coverage in North America was rather sparse. The latitudinal coverage is sparse above 70° .

For each station the diurnal variation in K was determined in relation to specific ranges of K_p . The K_p ranges used were: $0 \leq K_p \leq 2$; $2 < K_p \leq 4$; $4 < K_p \leq 6$; $6 < K_p$. If the planetary index K_p fell within the range, the corresponding K for each station were accumulated to get a yearly average K for that station and for each of the 3-hour periods in the day.

All of the times were adjusted to corrected geomagnetic time. The assumption was then made that the magnetic activity measured by K is dependent only on corrected geomagnetic time and corrected geomagnetic latitude. If the assumptions were true, stations at the same latitude would have the same diurnal variation and level for times shifted to corrected geomagnetic time. We had two sets of stations that fell at the same latitude--College and Kiruna at 64.8° , and Tromso and Leirvogur at 66.8° . Comparisons of the average K's for both pairs showed similar diurnal variations that differed by less than 10%. The data for each of these pairs were then averaged together. A simple latitude-weighted (1-2-1) average was used for latitude smoothing. The final K time-latitude surface was then generated by linear interpolations.

Contour plots of these surfaces are shown in Figures B-1 through B-5 for each K_p range of 1, 2, 3, 4, and 5. Linear interpolation is used in the model for intermediate K_p . In each case the presence of the nightside auroral oval is clearly evident. The change in size and equatorward shift for increasing K_p is also apparent. For comparison, the latitudinal extent of the RADC auroral oval is indicated by the vertical bar at midnight in each figure.

Table B-2

STATIONS USED IN DERIVING THE TEMPORAL RELATIONSHIP OF K FOR A GIVEN K_P

Station	Code	Geographic North Latitude (deg)	Geographic East Longitude (deg)	Corrected Geomagnetic North Latitude (deg)	Corrected Geomagnetic East Longitude (deg)
Cape Chelyashin	CC	77.72	104.28	71.58	174.19
Dixon Island	DI	73.55	80.57	68.31	154.69
Tromso	TR	69.67	18.95	66.75	104.78
Godhavn	GO	69.23	306.48	77.62	41.58
Murmansk	MM	68.25	33.08	64.42	113.87
Kiruna	KI	67.83	20.42	64.80	104.27
Sodankyla	SO	67.37	26.63	63.90	108.47
College	CO	64.87	212.17	64.84	259.65
Leirvogur	RY	64.18	338.30	66.82	69.53
Yakuisk	YA	63.02	129.67	57.58	198.85
Dombas	DO	62.07	9.12	60.08	91.89
Nurmijarvi	NU	60.52	24.65	57.14	102.96
Magadan	MG	60.12	151.02	53.91	217.36
Leningrad	LN	59.95	30.70	56.22	107.44
Sitka	SI	57.07	224.67	59.89	275.95
Newport	NE	48.26	243.01	55.38	299.46

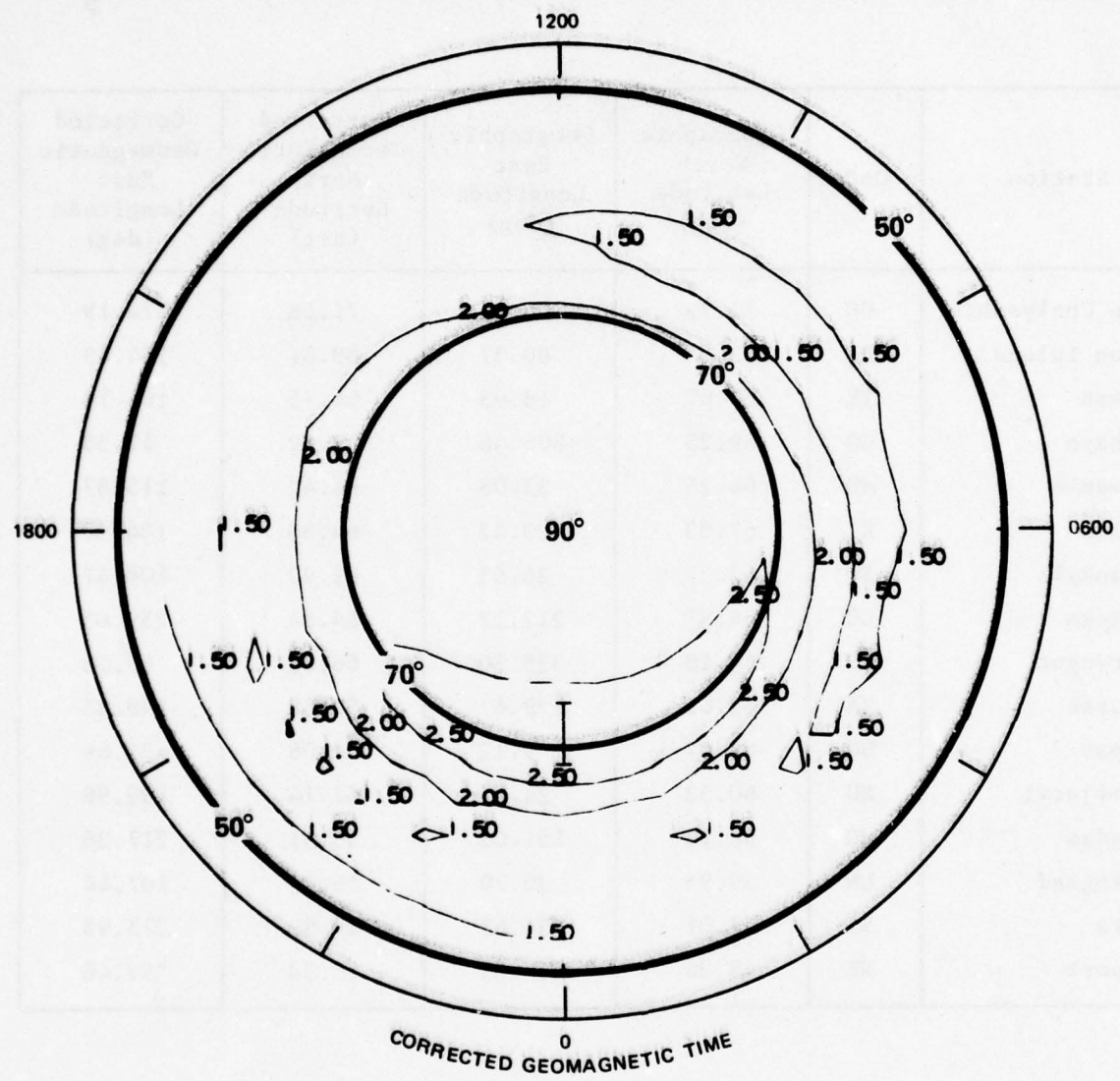


FIGURE B-1 VARIATION OF K WITH CORRECTED GEOMAGNETIC LATITUDE AND CORRECTED GEOMAGNETIC LOCAL TIME FOR A K_p OF 1. The boundaries of the RADC-POLAR specification of the auroral oval are also indicated.

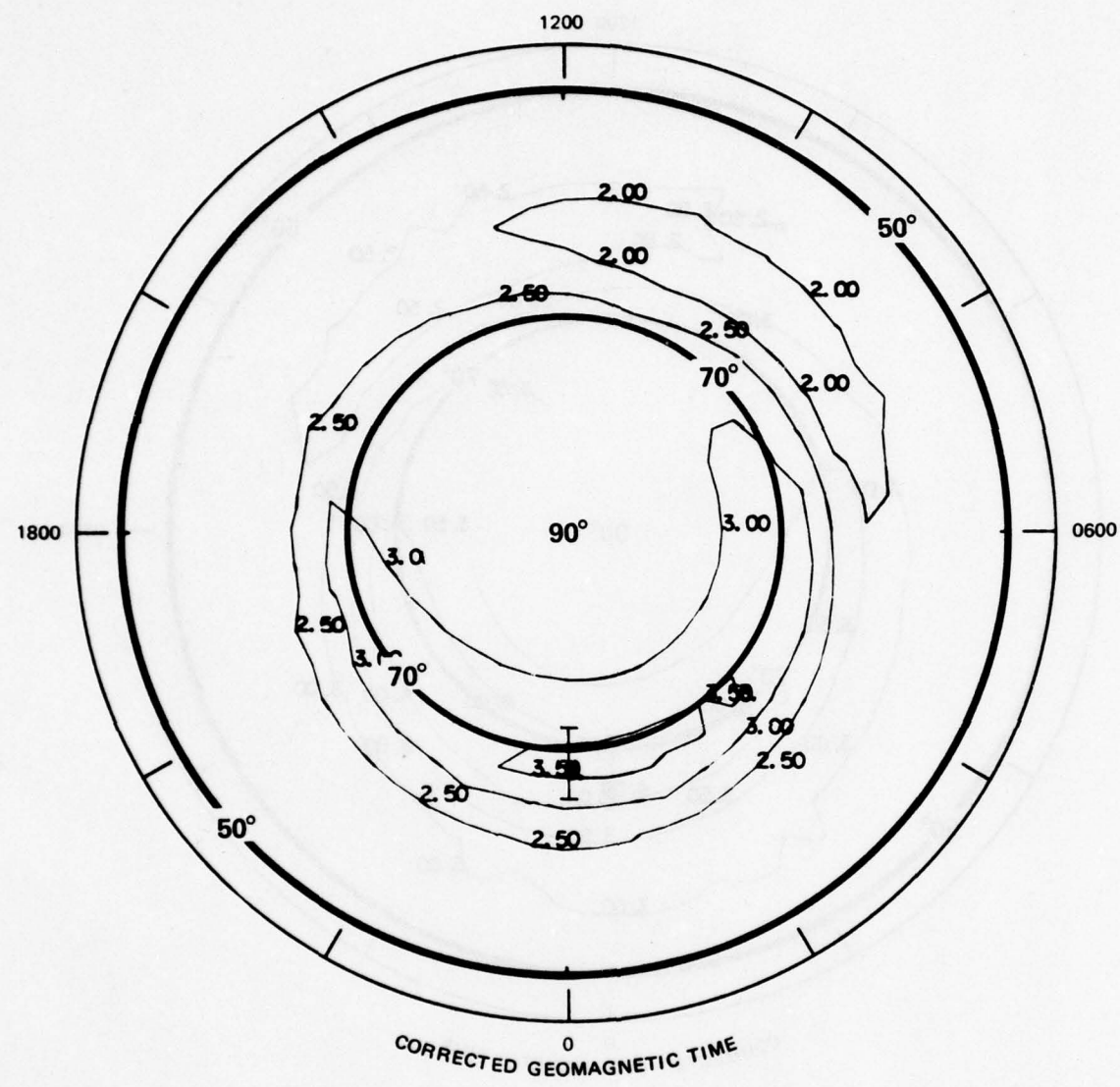


FIGURE B-2 VARIATION OF K WITH CORRECTED GEOMAGNETIC LATITUDE AND CORRECTED GEOMAGNETIC LOCAL TIME FOR A K_p OF 2. The boundaries of the RADC-POLAR specification of the auroral oval are also indicated.

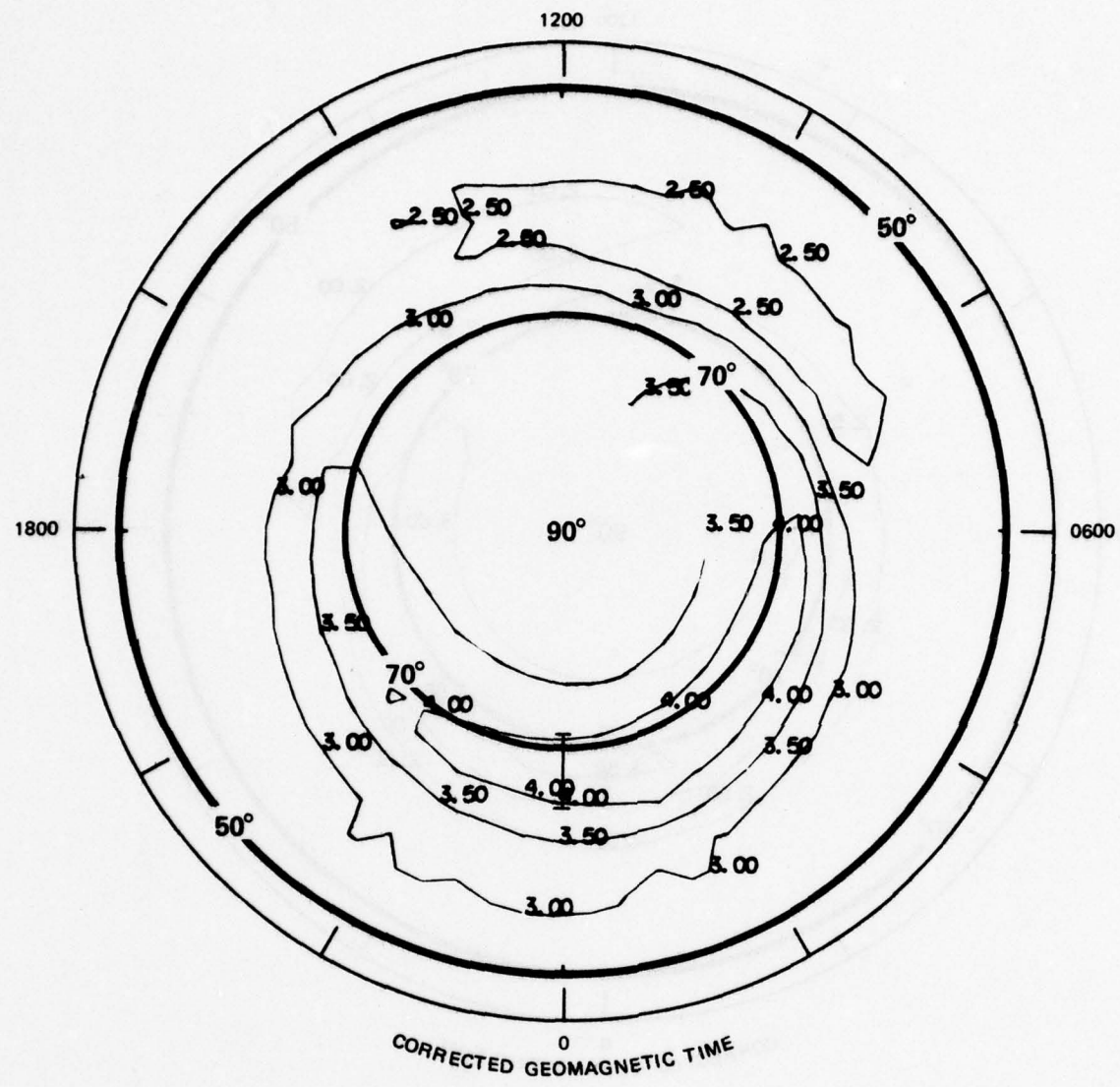


FIGURE B-3 VARIATION OF K WITH CORRECTED GEOMAGNETIC LATITUDE AND CORRECTED GEOMAGNETIC LOCAL TIME FOR A K_p OF 3. The boundaries of the RADC-POLAR specification of the auroral oval are also indicated.

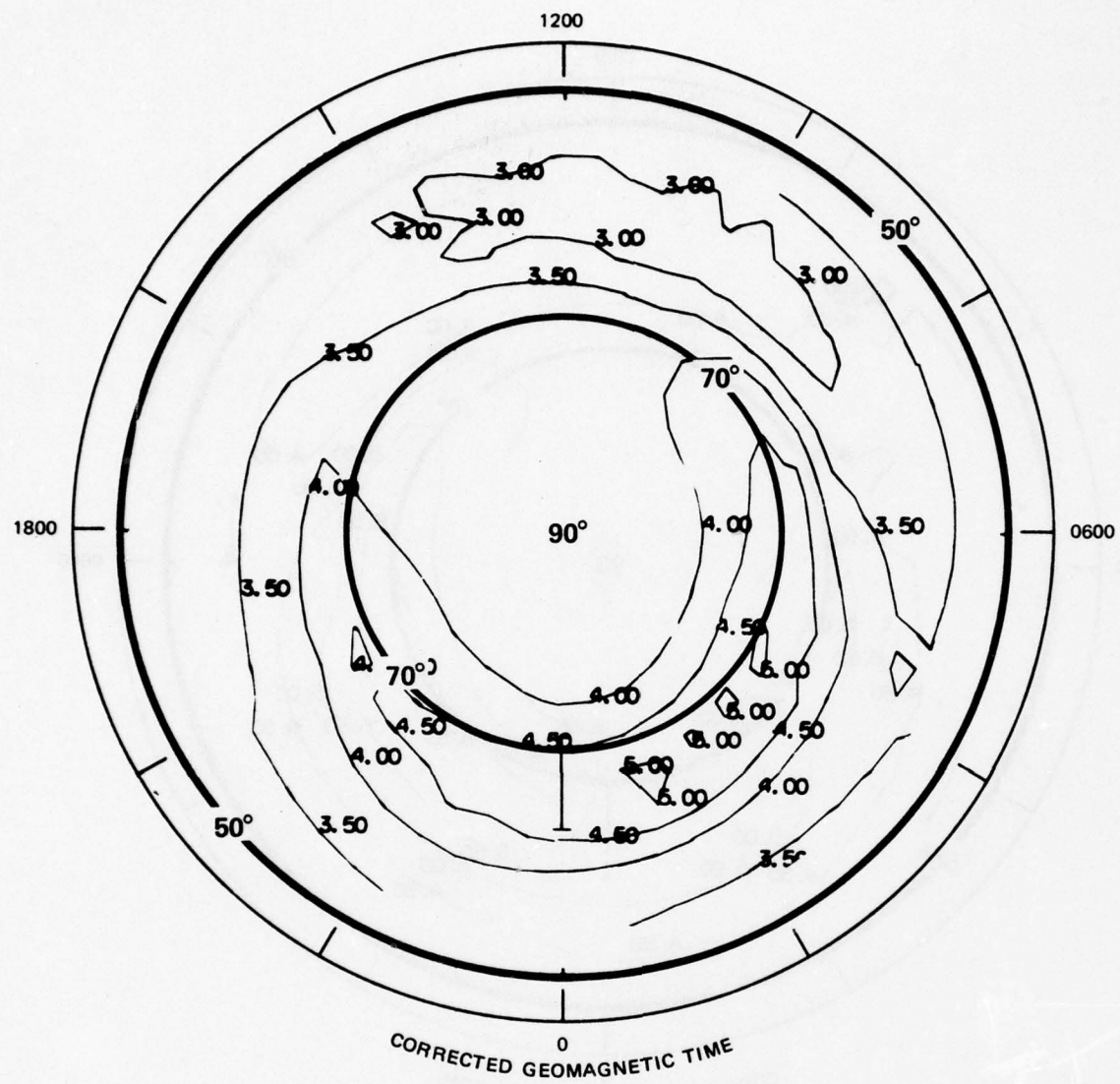


FIGURE B-4 VARIATION OF K WITH CORRECTED GEOMAGNETIC LATITUDE AND CORRECTED GEOMAGNETIC LOCAL TIME FOR A K_p OF 4. The boundaries of the RADC-POLAR specification of the auroral oval are also indicated.

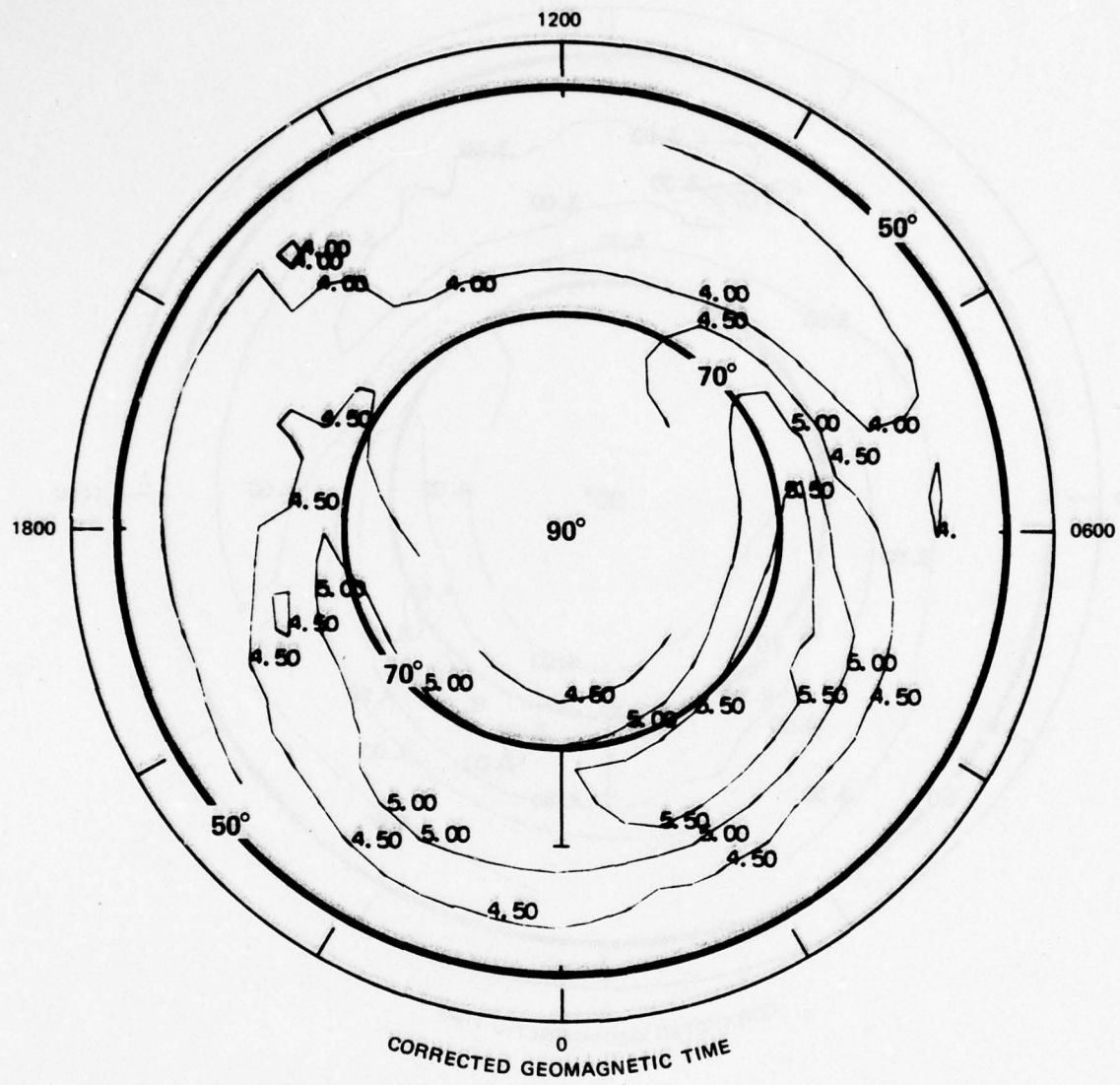


FIGURE B-5 VARIATION OF K WITH CORRECTED GEOMAGNETIC LATITUDE AND CORRECTED GEOMAGNETIC LOCAL TIME FOR A K_p OF 5. The boundaries of the RADC-POLAR specification of the auroral oval are also indicated.

Appendix C

DETAILED SPECIFICATION OF COMPUTER CODE FOR THE CHATANIKA MODEL

Appendix C

DETAILED SPECIFICATION OF COMPUTER CODE FOR THE CHATANIKA MODEL

The RADC-POLAR ionosphere generator, subroutine SUBPOLR, has been modified to incorporate the results of our study of electron density profiles observed by the Chatanika radar. A flowchart is shown in Figure C-1. The modifications were designed to leave as much of the program as possible unchanged, since a great deal of study and data analysis has gone into its development. As discussed in Section 4.1, we have modified the specification of the auroral E, and have added four new valley parameters. These parameters are generated in subroutine CHTNIK.

In addition we have modified the profile-generating routine PROFILE to incorporate the profile shapes that were observed in the Chatanika data. The new profile generator is called SRIPRO.

Four options have been provided. The first is ISRIMOD. If it is set to 1, SRI's modification will be applied; if it is zero, the original program will be executed. The next three options, INOP, INOG, INOT, allow the user to omit the printing, graphing, or tape output if they are set to 1; otherwise they are ignored.

A complete listing of the modified subroutines is given in Figure C-2. Also included is the listing of the absorption subroutine (SRISORP) described in Section 6.

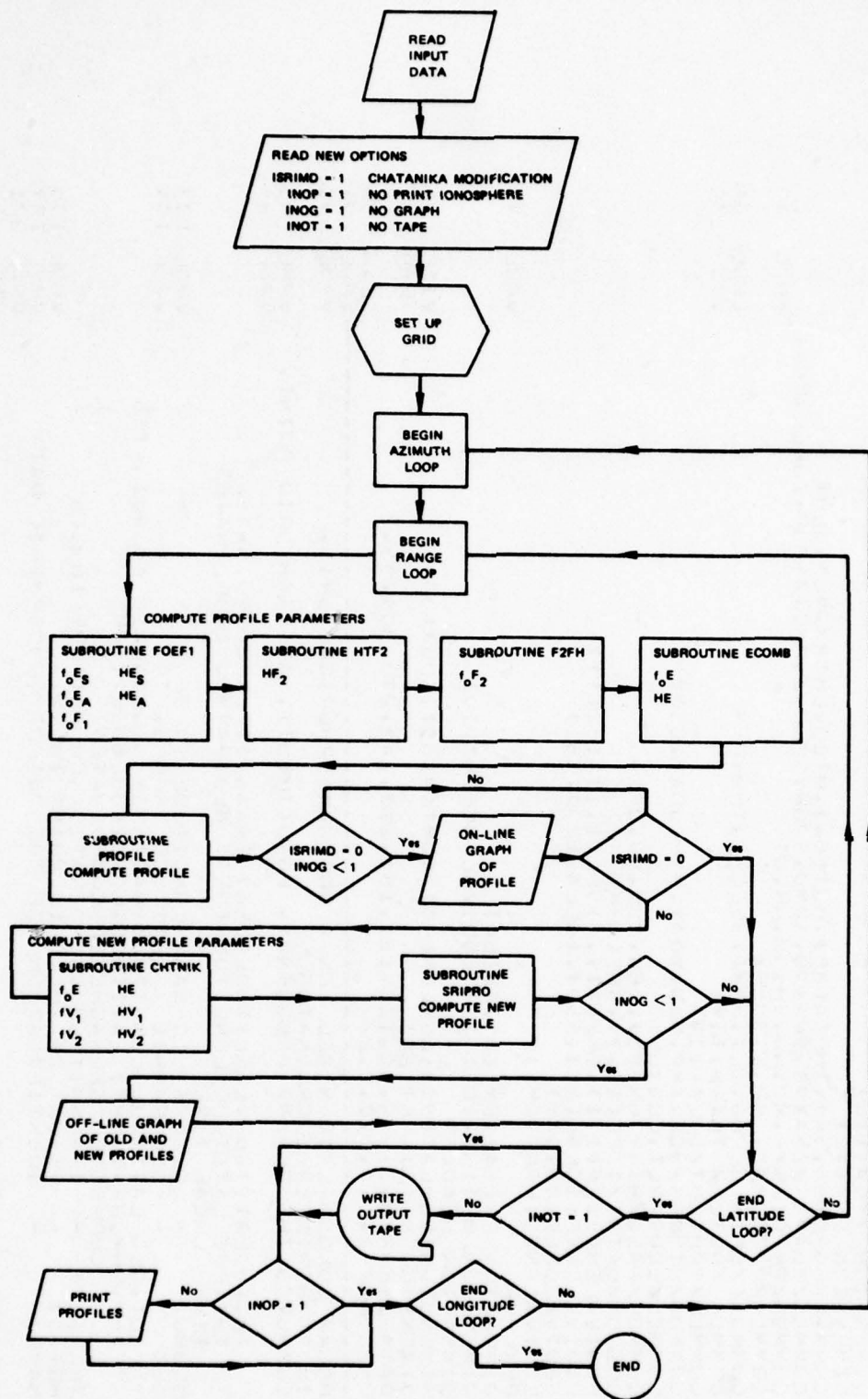


FIGURE C-1 FLOWCHART OF THE SRI MODIFICATIONS TO SUBPOLAR,
THE IONOSPHERE GENERATOR IN RADC-POLAR

SUBROUTINE SUCCESSFUL

15 SEP 1977 VERSION. MODIFIED BY ELAINE HATFIELD AT SRI
MODIFIED 4 FEB 1977 BY V. FRANK FOR INCREASED SIZE FILE
AND PRINTOUT OF REFLECTION DENSITY AT EACH OTHER POINT
9/12/77 HE MCC TO PASS GEOMAGNETIC COORDINATES
9/25/77 AND 10/7/77 FORMAT CHANGES

DIMENSION FP2(10),XF2(3,3),GOUT(24,3)

DIMENSION LYR(12)

DIMENSION ENK(4)

COMMON/LGRD/CG(30,24),THETA(30),HOT(54),HTZJ,LHTJ,X,MULTJ,OLHT

COMMON/VELAY/ER/2MAXWD,EMAXWD,SPMD,SPUP,SPD,LSMDO,ZSPUP,ZSPDU,FCFI1

COMMON/PREP1/NYR,MJ,ND,NM,NM,NS,UT

COMMON/PREP2/AP,KP,KR,SULFX

COMMON/ZEP1/ GLONG,CLT,HRMT,SECCHI,THM,PH

COMMON/ADLT/TH,PH,TIME

COMMON/EPHT/UT/SJLAR(28)

COMMON/MINDEX/XNGF,XRD,MUN,MDAY,MYR,JOAY,CSDY2

COMMON/CDOR/PLT,CLS,OM

COMMON/FREQ/HISY,UNE(3),DEG,SSN,EU,JFLAS

COMMON/DATA1/ISFE(10,3),SFF(98)

EQUIVALENCE(FF(1,1)*SF(1,1)),(ISFE(1,1)*FR2(1,1))

EQUIVALENCE(SCLAR(25),SSD),(SCLAR(29),SSL)

EQUIVALENCE(DJ,DAY)

REAL KP

DIMENSION FX(64),FY(64),FZ(64)

DIMENSION HD(15),ID(15),\$ EQUIVALENCE(HD, ID)

DIMENSION HEAD(6)

DIMENSION CGMLAT(40),CGMLON(80),CGMTIM(80),CGSX(80)

DIMENSION KC(7),KT(24)

DATA IYEAR/2*31*5*5*SC*120*151*181*212*243*273*304*334/

DATA KC/-2,0,C,0,C,2/-

POLAR TONGOSPHERIC MODEL ON A UNIFORM SPHERICAL GRID.

IN TRANSMITTER COORDINATES

COMPUTES THE PLASMA FREQUENCY, FGRT(TH,HT). AT EACH GRID POINT.

TH,PH LATITUDE,LONGITUDE(DEG) TRANSMITTER COORDINATES

TIME LOCAL TIME

GLONG - GEOGRAPHIC LATITUDE IN DEG.

CLT - GEOGRAPHIC LONGITUDE(RADIANS) GEOPHGRAPHIC COORDINATES

PLT,CLS LATITUDE,LONGITUDE(DEG).TIME

THM,PHM,HTMT(M) LATITUDE,LONGITUDE(DEG).TIME

THLTAT(1) - CORRECTED GEOMAGNETIC COORDINATES

HGT(1) - TRANSMITTER COORDINATES COLATITUDE IN KM.

NAME - HEIGHT OF THE GRID POINT IN KM.

NAME - IDENTIFICATION OF THE INPUT IONOSPHERIC DATA

3C FORMAT(15.0,(3X,12))

31 FORMAT(F10.5,315)

37 FORMAT(3F12.2)

ELAH 01
VICF 02
VICF 03
VICF 04

VICF 05
VICF 06
VICF 07
VICF 08

VPOL 09
VPOL 10
VPOL 11
VPOL 12
VPOL 13
VPOL 14
VPOL 15
VPOL 16
VPOL 17
VPOL 18
VPOL 19
VPOL 20
VPOL 21
VICI 12
VPOL 150

BEST AVAILABLE COPY

FIGURE C-2 LISTING OF SUBROUTINES USED IN SRI MODIFICATION OF THE RADCPOLAR IONOSPHERE GENERATOR

BEST AVAILABLE COPY

BEST AVAILABLE COPY

FIGURE C-2 (Continued)

```

IF((XKP•GE•2•3) NGE=NGP + 1
IF((XKP•GE•1•3) NGE=NGP + 1
IF((XKP•GE•2•3) NGE=NGP + 1
IF((XKP•GE•3•2) NGE=NGP + 1
IF((XKP•GE•4•2) NGE=NGP + 1
IF((XKP•GE•5•3) NGE=NGP + 1
DJE=(JULAY-15)*P12/365•0
IF((JUL.T<0) DJR=DJR + P12
FLUX=63•7494 + 0.7274*SSN + 0.0008695*SSN**2
READ(NTAPE) 1F2
READ(NTAPE)XF2
CALL COMPUT(FLUX,DJH,XF2,ANS)
FF(1)=ANS
DO 1C55 K=2• 399
READ(NTAPE)XF2
JJ=1C6HEC(INTAPE)
CALL COMPUT(FLUX,DJF,XF2,ANS)
1C55 FF(K)=ANS
PEIND NTAPE

C
      HD(1)=12HSH1PCLAJR
      HD(2)=1D•ELHTWX $ ID(3)=LATMX $ ID(4)=LUNMX
      HD(5)=HD•ELHTZC $ HD(6)=90•-THZC $ HD(7)=PHIZC
      HD(8)=DHF=DLHT $ HD(9)=DLTH $ HD(10)=DLPH
      HD(7)=180•C - PHIZC
      HD(11)=DLPH
      KYR=NYR/100
      KYR=NYR-100*KYR
      ENCODE(10•97,HD(11))KYR,MC,ND,NH,NM
      97 FORMAT(5I2)
      HD(12)=SOLFX $ HD(13)=R $ HD(14)=AP $ HD(15)=KP
      IF(INCT.LT.1) WRITE(4) HD

C.....SET UP THE GRID
C
      DO 54 I=1•LATMX
      54 THETA(I)=HTZC + FLOAT(I-1)*DLTH
      55 HGT(I) = HTZC + FLOAT(I-1)*DULH
C.....(LONGITUDE AND LATITUDE SPECIFICATION)
C
      DO 110 I=1•LONMX
      PH = PHIZC + FLCAT(I-1) * DLPH
      IF((PH•GE•360•) PH=PH-360•
      IF((PH•LT.0•0) PH=PH + 360•0
      SGMA=SIN(DEG*FH)
      CGMA=COS(DEG*FH)
      PRINT 2,NYR,MC,ND,UT
      PRINT 59
C
      DO 56 MLT=1•LATMX
      56 TH•PH IN TRANSITIVE COORDINATES
      TH=CJLAI

```

BEST AVAILABLE COPY

THE=THE.TA(CMLT)
 RG=111.12*TH
 STH=SIN(DEG*TR)
 CTH=CO(SDEG*TR)
 CTH=CTH*CTH + SST*STH*CGMA
 THW=PHN IN SELECTED MAGNETIC COORDINATES
 THI=CLAT
 THI=ACOS(CRHI)
 THI=90.0-THI
 SST=0.3*(TEM+THI/DEG+TH)
 S1=SIN(DEG*(SS-TEM))
 S2=SIN(DEG*(SS-TH))
 S3=SIN(DEG*(SS-THI))
 S4=SIN(DEG*(SS))
 SSK=S1*S2*S3/S4
 SK=SSK
 IF(SK.LT.0.0) SK=0.0
 SK=SQR(1.00)
 TDAZ=SK/S2
 PHI=2.0*ATAN(UTDAZ)/CEG + TCGD
 IF(PH+ST+180.0) PHI=-2.0*ATAN(UTDAZ)/CEG + TCGD
 C THI=LATITUDE
 THI=32.0 - THI/8.0
 C TH=LATITUDE
 TH=32.0 - TH
 IF(PHI+SL+360.0) PHI=PHI - 360.0
 IF(PHI.LT.3.0) PHI=PHI + 360.0
 C
 CLT=THI
 GLCNG=PHI
 CALL CGMCSC(CLTH, GLONG, THM, PHM)
 CMT=(PHM-SL)/15.0+2.
 IF(CMT.LT.0.0) CMT=CMT+24. \$ IF(CMT.GE.24.) CMT=CMT-24.
 C
 CALL Suntime(MYR, MO, ND, NH, NM, NS, CLT, GLONG)
 CALL FOEF1
 LOCAL TIME
 TIME=UT + GLONG/15.
 IF(TIME.GE.24.) TIME=TIME-24.
 C
 CALL HTF2(CLTH, THM, TIME, JDAY, SULFX, R, KP, HMF2, YM)
 PLT=CLT*DEG
 CLG=GLONG*DEG
 CALL F2FH(GCUT, 1, KLT, KUT, 1)
 FOE2=GDUT(KUT, 1)
 H1=ZMAXMD
 E1=EMAXMD
 H2=ZSPMD
 E2=SPMD
 CALL ECUNB(H1, E1, H2, E2, HME, FCE)
 DO 501 JP=1,64
 FX(JP)=C*0
 FY(JP)=C*0
 501 FZ(JP)=C*0

BEST AVAILABLE COPY

FIGURE C-2 (Continued)


```

C 2400 GO TO 2
C 120 CONTINUE
C CALL SPLIT
C END

```

BEST AVAILABLE COPY

```

FUNCTION CHAPMN(FN,HW,YM,ALPHA,H)
C SEP 1977 BY ELAINE PATFIELD. SRI INTERNATIONAL, MENLO PARK, CALIF
C THIS FUNCTION COMPUTES A CHAPMAN ELECTRON DENSITY PROFILE
C
S1=2.**(H-HW)/YM
EVAL=0.0
IF(S1.LT.-.89.) EVAL=EXP(-S1)
CHAPMN=FN*EXP(ALPHA*(1.-S1-EVAL))
C
RETURN
C END

```

FIGURE C-2 (Continued)

* HE, ET)
* SUBROUTINE CHNIK(CHI,AKF,R,HMF1,HMF2,FCF1,FCF2,FCF1=1,FCF2=1,CGAT,CGLAT,

C COMPUTES LONGSPHERIC PARAMETERS DERIVED FROM CHATNIKA REFLECTION
C DENSITY PROFILES
C 22 SEPT 1977 BY ELAINE HATFIELD, SRI INTERNATIONAL
C LAST MODIFICATION 1C/7/77

C DIMENSION ACHI(5),AEC1(5),AEC2(5),AEH1(5),AEH2(5),AFV11(5),
C AFV12(5),AFV21(5),AFV22(5),AHV11(5),AHV12(5),AHV21(5),AHV22(5)
C COMMON /CHAT/HVAL1,FVAL1,HVAL2,FVAL2,NOCHAT
C COMMON /EF1/ACUM(2),SECH1,CGLAT,PHM
C DATA(ACHI(1),1=1,5)/500.035.070.035.095.0105.0/
C PARAMETER 17*
C AURORAL CRIT
C DATA(AEC1(1),1=1,5)/1.68.01.67.0837.0477.0899/
C DATA(AEC2(1),1=1,5)/.0555.0377.0623.0629.0625/
C PARAMETER 8-A
C E-LAYER HEIGHT
C DATA(AEH1(1),1=1,5)/116.0110.0117.0114.0118.0/
C DATA(AEH2(1),1=1,5)/-541.0-681.0-261.0737.0-292/
C PARAMETER 13-A
C E-F1 VALLEY RATIO TO FOF2
C DATA(AFV11(1),1=1,5)/914.0577.0450.0302.0440/
C DATA(AFV12(1),1=1,5)/.0614.00957.0115.0108.0132/
C PARAMETER 14-A
C F1 F2 VALLEY RATIO TO FOF2
C DATA(AFV21(1),1=1,5)/742.0666.0755.0297.0474/
C DATA(AFV22(1),1=1,5)/-003333.0516.00321.00931.00644/
C PARAMETER 11-E
C VALLEY 1 HEIGHT RATIO -- (HV1-HE)/(HF2-HE)
C DATA(AHV11(1),1=1,5)/.591.00552.0163.0226.0347/
C DATA(AHV12(1),1=1,5)/-.115.00699.00643.00580.00421/
C PARAMETER 12-E
C VALLEY 2 HEIGHT RATIO -- (HV2-HE)/(HF2-HE)
C DATA(AHV21(1),1=1,5)/.795.0694.0606.0372.0533/
C DATA(AHV22(1),1=1,5)/-.0307.00196.00195.00553.00732/
C DATA RTD/57.2957795/
C DATA JCHI/2/
C DATA PI12/0.251799388/

C 105 PRINT 105,CHI,CGLAT,CGMT
C 105 FORMAT(5H CHI=,E10.2,7H CGLAT=,E10.3,5H CGMT=,E10.3)
C HVAL1=0.0
C FVAL1=0.0
C HVAL2=0.0
C FVAL2=0.0
C NOCHAT=1

C TEST FOR TWO LOW F1
C IF(FCF1.LT.FCF2/10.) FCF1=FCF2
C COMPUTE F1 HEIGHT IF F1 LAYER EXISTS
C HMF1=0.0
C IF(FCF1.GT.0.1)

FIGURE C-2 (Continued)

BEST AVAILABLE COPY

```

1HMFI=156.0+15*I2 + 4E.*ALCG(SECCHI)
C AURORAL OVAL LIMITATIONS
C IF(CGMAT.GT.5.0.AND.CGMAT.LT.1.0) GO TO 201
C IF(CGLAT.LT.-72.0) GO TO 202
PHI1=71.0-2.5*AKP*CGS(P112*(CGMT ))
IF(CGLAT.LT.P11) GO TO 203
C SOUTH OF OVAL
CONTINUE
C
E2=-1.0
H2=117.0-1.013*E2
H1=.00021
IF(SECCHI.GT.0.0) H1=100.*10.*ALB*(SECCHI)
CALL ECOMTE(H1,E1,12.02*HE.ET)
RETURN
C
202 CONTINUE
POLAR CAP
RETURN
C
201 CONTINUE
C DAY TIME
C IF(CGLAT.LT.51.0) GO TO 204
C SOUTH OF 51 DEGREES
C PHI1B2=78.0-2.5*AKP+4.*{1.0+25.*AKP }
C IF(CGLAT.LT.PHIB2) GO TO 203
C POLAR CAP
RETURN
C
203 CONTINUE
C
C COMPUTE LOCAL K AS FUNCTION OF CGMT.CGLAT AND KP
FK=FUNKP(AKP,CGMT.CGLAT)
IF(FK.LT.0.0. OR.FK.GE.100.) RETURN
N2CHATEU
C
C COMPUTE AURORAL E CRITICAL FREQUENCY
EC1=FGENRL( CHI.JCHI.ACHI.AE1.S)
EC2=FGENRL( CHI.JCHI.ACHI.AEC2.S)
E2=EC1+FK*EC2
C
HEH1
C COMPUTE COMBINED SCALAR AND AURORAL E CRITICAL FREQUENCY AND HEIGHT
CALL ECUMB(H1,E1,H2.02*HE.ET)
C
C COMPUTE VALLEY CRITICAL FREQUENCY RATIOS
C
C COMPUTE E-LAYER HEIGHT
EH1=FGENRL( CHI.JCHI.ACHI.AEH1.S)
EH2=FGENRL( CHI.JCHI.ACHI.AEH2.S)
HE=EH1+EH2*FK
C
C COMPUTE F VAL ! RATIO
FV11=FGENRL( CHI.JCHI.ACHI.AFV11.S)
FV12=FGENRL( CHI.JCHI.ACHI.AFV12.S)
FV1R=FV11+FK*FV12
C

```

BEST AVAILABLE COPY

FIGURE C-2 (Continued)

```

      COMPUTE FVAL2 RATIO
      FV21=FGENRL(CH1,JCH1,ACH1,AFV21,5)
      FV22=FGENRL(CH1,JCH1,ACH1,AFV22,5)
      FV21=FVAL1+FV22

      COMPUTE VALLEY FLIGHT RATIOS

      COMPUTE HVAL1 RATIO
      HV11=FGENRL(CH1,JCH1,ACH1,AHV11,5)
      HV12=FGENRL(CH1,JCH1,ACH1,AHV12,5)
      HV12=HV11+HV12*FK

      COMPUTE HVAL2 RATIO
      HV21=FGENRL(CH1,JCH1,ACH1,AHV21,5)
      HV22=FGENRL(CH1,JCH1,ACH1,AHV22,5)
      HV22=HV21+HV22*FK

      DELH=HMF2 - HF

      COMPUTE VALLEY PARAMETERS

      FVAL1=FV1R*FCF2
      HVAL1=HV1R*FCF2
      FVAL2=FV2R*FCF2
      HVAL2=HV2R*FCF2

      COMPUTE VALLEY PARAMETERS

      FVAL1=FV1R*FCF2
      HVAL1=HV1R*FCF2
      FVAL2=FV2R*FCF2
      HVAL2=HV2R*FCF2

      CHECK ON F1 HEIGHT
      IF(HMF2-HMF1.LT.4C.)HMF1=0.0
      IF(HMF1.LQ.0.C)FCF1=0.0
      IF(HMF1-HE.LT.20.)HMF1=0.0

      PRELIMINARY VALLEY TEST
      CHECK ON VALLEY HEIGHTS
      IF(HVAL1-HE.LT.20.)HVAL1=0.0
      IF(HVAL2-HE.LT.20.)HVAL2=0.0
      IF(HVAL1.LT.4C.)HVAL1=0.0
      IF(HVAL2.LT.4C.)HVAL2=0.0
      IF(HVAL1.EQ.0.C)FVAL1=0.0
      IF(HVAL2.EQ.0.C)FVAL2=0.0

      CHECK ON VALLEY CRITICAL FREQUENCIES
      IF(FOF1.GT.5.C)GO TO 23
      IF(FVAL1.LT.ET.CR.FVAL1.LT.FOF2)GO TO 20
      FVAL1=0.0
      HVAL1=0.0
      GO TO 20
      FVAL1=0.0
      HVAL1=0.0
      GO TO 20
      IF(FVAL1.LT.ET.CR.FVAL1.LT.FOF1)GO TO 20
      FVAL2=0.0
      HVAL2=0.0
      GO TO 20
      IF(FVAL2.LT.ET.CR.FVAL2.LT.FOF2)GO TO 21
      FVAL2=0.0
      HVAL2=0.0
      CONTINUE

```

FIGURE C-2 (Continued)

NOT AVAILABLE COPY

```

C CHECK FOR EXISTENCE OF VALLEYS
C IF (HVAL1.EQ.0.C AND HVAL2.EQ.0.C) GO TO 14
C
C CHECK F1 LAYER
C IF (HMF1.EQ.0.C) GO TO 10
C
C CHECK LOCATION OF VALLEYS
C IF ( HMF1.GT.HVAL1 .AND. HVAL2.GT.HMF1 ) GO TO 11
C
C HVAL1=(HVAL1+HMF1+HVAL2)/3.
C HVAL2=0.C
C HMF1=0.C
C FVAL1=(FVAL1+FVAL2+FVAL2)/2.
C FOF1=0.C
C GO TO 11
C
C 12 CONTINUE
C HVAL2=0.C
C FVAL2=0.C
C
C GO TO 13
C 14 CONTINUE
C IF (HVAL1.EQ.0.C AND HVAL2.EQ.0.C) GO TO 11
C IF (HVAL2.EQ.0.C) GU TU 15
C IF (HMF1.GT.0.C AND HVAL2.GT.HMF1 ) GO TO 11
C HVAL1=HVAL2
C HVAL1=FVAL2
C HVAL2=0.C
C FVAL2=0.C
C IF (HMF1.GT.0.C) HVAL1=(HVAL1+HMF1)/2.
C IF (HMF1.GT.0.C) FVAL1=(FVAL1+FOF1)/2.
C HMF1=0.C
C FOF1=0.C
C GO TO 11
C 15 IF (HMF1.EQ.0.C OR HMF1.GT.HVAL1 ) GO TO 11
C HVAL1=(HMF1+HVAL1)/2.
C FVAL1=(FOF1+FVAL1)/2.
C HMF1=0.C
C FOF1=0.C
C 11 CONTINUE
C
C FCF=FT
C TEST FOR TRUE VALLEYS
C IF (FVAL1.EQ.0.C) GU TU 25
C IF (FOF1.GT.0.C) GO TU 24
C FVTEST=ALUG(FCFCE)+(HVAL1-HE)/(HMF2-HE)*ALUG(FOF2/FOF1)
C 27 IF (ALUG(FVAL1).LT.FVTEST) GU TU 25
C FVAL1=0.C
C HVAL1=0.C
C GO TU 25
C FVTEST=ALUG(FOF1)+(HVAL1-HE)/(HMF1-HE)*ALUG(FCF1/FOF1)
C 24 GU TU 27

```

BEST AVAILABLE COPY

FIGURE C-2 (Continued)

```

45 IF (FVAL2>=0.0) GO TO 45
46 FVTEST=ALOG(FCF1)+(FVAL2-HMF1)/(H4F2-HMF1)*ALOG(FCF2/FCF1)
47 F(FALOG(FVAL2).LT.FVTEST) GO TO 26
48 FVAL2=0.0
49 HVAL2=0.0
50 CONTINUE
51 C
52 C 100 FORMAT(7H CHTRLK•3E10•3)
53 RETURN
54 END

```

```

C FUNCTION EXPON(FN,HW,YSC,H)
C SEP 1977 BY ELAINE HATFIELD, SRI INTERNATIONAL, MENLO PARK, CALIF
C THIS FUNCTION COMPUTES AN EXPONENTIAL PROFILE
C
C S1=(H-HM)/YSC
C EVAL=0.0
C IF(S1.LT.269.) EVAL=EXP(-S1)
C EXPON=FN*EVAL
C
C RETURN
C END

```

FIGURE C-2 (Continued)

1 BEST AVAILABLE COPY

```

C      SEP 1977 BY CLAINE PATFIELD. SRI INTERNATIONAL. MENLO PARK, CALIF
C      FUNCTION FGENRL(DIST,J,D,V,N)
C      DIMENSION V(1),D(1)
11      CONTINUE
C      IF(J.LE.1) 18,15
13      J=2
14      GO TO 16
15      IF(J.GT.N) 20,21
20      J=N
21      GO TO 16
21      CONTINUE
C      IF(DIST-D(J))13,14,15
14      FGENRL=V(J)
15      RETURN
16      IF(DIST.GT.D(J-1)) 16,17
17      CONTINUE
C      J=J-1
18      GO TO 11
19      J=J+1
20      GO TO 11
21      FGENRL=V(J-1)+(DIST-D(J-1))*(V(J)-V(J-1))/(D(J)-D(J-1))
22      PRINT 100,J,DIST,FGENRL,V(J),D(J),V(J-1),D(J-1)
23      FORMAT(7H FGENRL,15.6E10.3)
24      RETURN
C      END

```

BEST AVAILABLE COPY

FIGURE C-2 (Continued)

```

FUNCTION FUNKP(AKP,CCMT,CGLAT)
C
C   CSEFTES K AS A FUNCTION OF KP INDEX, CORRECTED GEOMAGNETIC LOCAL
C   TIME AND LATITUDE
C   THE RELATIONSHIP HAS BEEN ESTABLISHED ELECTRICALLY FOR 1963
C   COVERING THE YEARS 1963
C   22 SEPT 1977 BY ELAINE HATHFIELD. 581 INTERNATIONAL
C
C   DIMENSION ATIN(14), ALAT(14), ARKP(4), AK(12,14,4)
C
C   DATA INIT/1/
C
C   DATA(AK(1,1,1,1),1=1,1)
C   1/1.35*1.30*2.30*2.21*2.02*0.99,1.031,1.073,1.056,1.078,1.050/
C   DATA(AK(1,1,2),1=1,1)
C   1/2.73*2.74*2.82*3.06*2.79,2.052,2.053,2.069,2.074,2.071/
C   DATA(AK(1,1,3),1=1,1)
C   1/4.09*3.77*3.75*4.19*3.97,3.037,3.039,3.045,3.091,4.029/
C   DATA(AK(1,1,4),1=1,1)
C   1/5.92*5.67*5.74*6.22*5.66,5.021,5.032,5.013,5.067,5.021/
C   DATA(AK(1,2,1),1=1,1)
C   1/1.26*1.34*1.54*1.73*1.75,1.083,1.062,1.021,1.025/
C   DATA(AK(1,2,2),1=1,1)
C   1/2.53*2.54*2.40*2.48*2.39,2.073,2.063,2.050,2.053/
C   DATA(AK(1,2,3),1=1,1)
C   1/2.32*3.66*3.95*3.58*3.36,3.058,3.084,3.034,3.082,3.040/
C   DATA(AK(1,2,4),1=1,1)
C   1/6.21*5.41*5.55*5.30*5.28,5.073,6.010,5.087,6.067,6.021/
C   DATA(AK(1,3,1),1=1,1)
C   1/2.03*1.39*1.55*1.61*1.72,2.007,2.023,2.023,2.015,2.03/
C   DATA(AK(1,3,2),1=1,1)
C   1/3.07*3.03*2.63*2.40*2.39,2.070,2.085,2.099,3.004,3.077/
C   DATA(AK(1,3,3),1=1,1)
C   1/4.32*4.31*3.81*3.02*2.96,3.014,4.000,3.070,4.023,4.033/
C   DATA(AK(1,3,4),1=1,1)
C   1/6.77*7.10*6.32*5.43*5.05,5.053,5.053,5.053,5.053,5.053/
C   DATA(AK(1,4,1),1=1,1)
C   1/1.75*1.66*1.45*1.41*1.45,1.067,1.077,1.030,1.031,1.075/
C   DATA(AK(1,4,2),1=1,1)
C   1/2.84*2.80*2.47*2.12*2.12,2.047,2.063,2.071,2.073,2.034/
C   DATA(AK(1,4,3),1=1,1)
C   1/4.29*4.19*3.67*2.88*2.94,3.000,3.073,3.063,4.005,4.020/
C   DATA(AK(1,4,4),1=1,1)
C   1/6.66*6.61*5.88*5.29*4.74,5.043,6.021,5.026,5.041,5.055/
C   DATA(AK(1,5,1),1=1,1)
C   1/1.37*1.91*2.10*2.17*2.08,1.069,1.048,1.044,1.035,1.047/
C   DATA(AK(1,5,2),1=1,1)
C   1/2.10*2.41*2.01*3.01*2.71,2.025,2.016,2.059,2.080,2.030/
C   DATA(AK(1,5,3),1=1,1)
C   1/4.22*3.68*4.05*3.59,2.081,3.022,3.053,4.045,4.022/
C   DATA(AK(1,5,4),1=1,1)

```

FIGURE C-2 (Continued)

BEST AVAILABLE COPY

BEST AVAILABLE COPY

FIGURE C-2 (Continued)

```

14 PRINT(11,ARKP(K1),ATIM(11),(AK(11,1,K1),J1=1,14))
14:  FORMAT(4H KP=,F4.1,CH 11,14,11,14,11,14,11,14,11,14,11,14,11,14,11,14)
11 CONTINUE
12 CONTINUE
11 INIT=C
12 CONTINUE
C FUNKP=TRIP(CGNT,ATIN,11,10,CGLAT,ALAT,JJ,14,AKD,ARKP,CK,4,AK)
C
C RETURN
END

```

FIGURE C-2 (Continued)

NOT AVAILABLE COPY

FUNCTION PARA(FN, HM, YSC, H)
C SEP 1977 BY ELAINE PATFIELD. SKI INTERNATIONAL. VENICE PARK. CALIF
THIS FUNCTION COMPUTES A PARAPOLIC PROFILE
C
C S1=(H-HM)/YSC
C PARA8=FN*(1.0-S1**2)
C RETURN
C END

FIGURE C-2 (Continued)

BEST AVAILABLE COPY

```

FUNCTION TRITSO(XA,X1,I,N1,X3,X2,J,N2,XL,X3,K,N3,Y)
C 22 SEPT 1977 BY ELAINE MATEFIELD. SRI INTERNATIONAL
C
C DIMENSION X1(1),X2(1),X3(1)
C
C IND1=0
C IND2=0
C IND3=0
C IND4=0
C
C 10 CONTINUE
C 11 IF (I.LE.1) 10,12,13
C 12 GO TO 15
C 13 IF (I.GT.N1) 20,21
C 14 GO TO 16
C 15 CONTINUE
C 16 IF (XA-X1(I)) 13,14,15
C 17 CONTINUE
C 18 IF (J.LE.1) 16,17
C 19 GO TO 11
C 20 CONTINUE
C 21 IF (J.GT.N2) 24,25
C 22 GO TO 23
C 23 CONTINUE
C 24 IF (J.GT.N2) 26,27
C 25 GO TO 26
C 26 CONTINUE
C 27 IF (J.LE.1) 24,28
C 28 GO TO 29
C 29 CONTINUE
C 30 IF (X3-X2(J)) 31,32
C 31 GO TO 33
C 32 CONTINUE
C 33 IF (X3.GT.X2(J-1)) 34,35
C 34 GO TO 36
C 35 CONTINUE
C 36 IF (X3-X2(J)) 37,38
C 37 GO TO 39
C 38 CONTINUE
C 39 IF (X3.GT.X2(J-1)) 40,41
C 40 GO TO 41
C 41 CONTINUE
C 42 IF (K.LE.1) 42,43
C 43 GO TO 44
C 44 CONTINUE
C 45 IF (K.GT.N3) 46,47
C 46 GO TO 48
C 47 CONTINUE
C 48 IF (X3-X2(K)) 49,50
C 49 GO TO 51
C 50 CONTINUE
C 51 IF (X3.GT.X2(K-1)) 52,53
C 52 GO TO 54
C 53 CONTINUE
C 54 IF (X3-X2(K)) 55,56
C 55 GO TO 57
C 56 CONTINUE
C 57 IF (X3.GT.X2(K-1)) 58,59
C 58 GO TO 60
C 59 CONTINUE
C 60 IF (X3-X2(K)) 61,62
C 61 GO TO 63
C 62 CONTINUE
C 63 IF (X3.GT.X2(K-1)) 64,65
C 64 GO TO 66
C 65 CONTINUE
C 66 IF (X3-X2(K)) 67,68
C 67 GO TO 69
C 68 CONTINUE
C 69 IF (X3.GT.X2(K-1)) 70,71
C 70 GO TO 71
C 71 CONTINUE
C 72 IF (K.EQ.N3) 72,73
C 73 GO TO 74
C 74 CONTINUE
C 75 IF (X3-X2(K)) 76,77
C 76 GO TO 78
C 77 CONTINUE
C 78 IF (X3.GT.X2(K-1)) 79,80
C 79 GO TO 81
C 80 CONTINUE
C 81 IF (X3-X2(K)) 82,83
C 82 GO TO 84
C 83 CONTINUE
C 84 IF (X3.GT.X2(K-1)) 85,86
C 85 GO TO 87
C 86 CONTINUE
C 87 IF (X3-X2(K)) 88,89
C 88 GO TO 90
C 89 CONTINUE
C 90 IF (X3.GT.X2(K-1)) 91,92
C 91 GO TO 93
C 92 CONTINUE
C 93 IF (X3-X2(K)) 94,95
C 94 GO TO 96
C 95 CONTINUE
C 96 IF (X3.GT.X2(K-1)) 97,98
C 97 GO TO 99
C 98 CONTINUE
C 99 IF (X3-X2(K)) 100,101
C 100 GO TO 101
C 101 CONTINUE
C 102 IF (X3.GT.X2(K-1)) 102,103
C 103 GO TO 104
C 104 CONTINUE
C 105 IF (X3-X2(K)) 106,107
C 106 GO TO 108
C 107 CONTINUE
C 108 IF (X3.GT.X2(K-1)) 109,110
C 109 GO TO 111
C 110 CONTINUE
C 111 IF (X3-X2(K)) 112,113
C 112 GO TO 114
C 113 CONTINUE
C 114 IF (X3.GT.X2(K-1)) 115,116
C 115 GO TO 117
C 116 CONTINUE
C 117 IF (X3-X2(K)) 118,119
C 118 GO TO 120
C 119 CONTINUE
C 120 IF (X3.GT.X2(K-1)) 121,122
C 121 GO TO 123
C 122 CONTINUE
C 123 IF (X3-X2(K)) 124,125
C 124 GO TO 126
C 125 CONTINUE
C 126 IF (X3.GT.X2(K-1)) 127,128
C 127 GO TO 129
C 128 CONTINUE
C 129 IF (X3-X2(K)) 130,131
C 130 GO TO 132
C 131 CONTINUE
C 132 IF (X3.GT.X2(K-1)) 133,134
C 133 GO TO 135
C 134 CONTINUE
C 135 IF (X3-X2(K)) 136,137
C 136 GO TO 138
C 137 CONTINUE
C 138 IF (X3.GT.X2(K-1)) 139,140
C 139 GO TO 141
C 140 CONTINUE
C 141 IF (X3-X2(K)) 142,143
C 142 GO TO 144
C 143 CONTINUE
C 144 IF (X3.GT.X2(K-1)) 145,146
C 145 GO TO 147
C 146 CONTINUE
C 147 IF (X3-X2(K)) 148,149
C 148 GO TO 150
C 149 CONTINUE
C 150 IF (X3.GT.X2(K-1)) 151,152
C 151 GO TO 153
C 152 CONTINUE
C 153 IF (X3-X2(K)) 154,155
C 154 GO TO 156
C 155 CONTINUE
C 156 IF (X3.GT.X2(K-1)) 157,158
C 157 GO TO 159
C 158 CONTINUE
C 159 IF (X3-X2(K)) 160,161
C 160 GO TO 162
C 161 CONTINUE
C 162 IF (X3.GT.X2(K-1)) 163,164
C 163 GO TO 165
C 164 CONTINUE
C 165 IF (X3-X2(K)) 166,167
C 166 GO TO 168
C 167 CONTINUE
C 168 IF (X3.GT.X2(K-1)) 169,170
C 169 GO TO 171
C 170 CONTINUE
C 171 IF (X3-X2(K)) 172,173
C 172 GO TO 174
C 173 CONTINUE
C 174 IF (X3.GT.X2(K-1)) 175,176
C 175 GO TO 177
C 176 CONTINUE
C 177 IF (X3-X2(K)) 178,179
C 178 GO TO 180
C 179 CONTINUE
C 180 IF (X3.GT.X2(K-1)) 181,182
C 181 GO TO 183
C 182 CONTINUE
C 183 IF (X3-X2(K)) 184,185
C 184 GO TO 186
C 185 CONTINUE
C 186 IF (X3.GT.X2(K-1)) 187,188
C 187 GO TO 189
C 188 CONTINUE
C 189 IF (X3-X2(K)) 190,191
C 190 GO TO 192
C 191 CONTINUE
C 192 IF (X3.GT.X2(K-1)) 193,194
C 193 GO TO 195
C 194 CONTINUE
C 195 IF (X3-X2(K)) 196,197
C 196 GO TO 198
C 197 CONTINUE
C 198 IF (X3.GT.X2(K-1)) 199,200
C 199 GO TO 201
C 200 CONTINUE
C 201 IF (X3-X2(K)) 202,203
C 202 GO TO 204
C 203 CONTINUE
C 204 IF (X3.GT.X2(K-1)) 205,206
C 205 GO TO 207
C 206 CONTINUE
C 207 IF (X3-X2(K)) 208,209
C 208 GO TO 210
C 209 CONTINUE
C 210 IF (X3.GT.X2(K-1)) 211,212
C 211 GO TO 213
C 212 CONTINUE
C 213 IF (X3-X2(K)) 214,215
C 214 GO TO 216
C 215 CONTINUE
C 216 IF (X3.GT.X2(K-1)) 217,218
C 217 GO TO 219
C 218 CONTINUE
C 219 IF (X3-X2(K)) 220,221
C 220 GO TO 222
C 221 CONTINUE
C 222 IF (X3-X2(K)) 223,224
C 223 GO TO 225
C 224 CONTINUE
C 225 IF (X3.GT.X2(K-1)) 226,227
C 226 GO TO 228
C 227 CONTINUE
C 228 IF (X3-X2(K)) 229,230
C 229 GO TO 231
C 230 CONTINUE
C 231 IF (X3.GT.X2(K-1)) 232,233
C 232 GO TO 234
C 233 CONTINUE
C 234 IF (X3-X2(K)) 235,236
C 235 GO TO 237
C 236 CONTINUE
C 237 IF (X3.GT.X2(K-1)) 238,239
C 238 GO TO 240
C 239 CONTINUE
C 240 IF (X3-X2(K)) 241,242
C 241 GO TO 243
C 242 CONTINUE
C 243 IF (X3.GT.X2(K-1)) 244,245
C 244 GO TO 246
C 245 CONTINUE
C 246 IF (X3-X2(K)) 247,248
C 247 GO TO 249
C 248 CONTINUE
C 249 IF (X3.GT.X2(K-1)) 250,251
C 250 GO TO 252
C 251 CONTINUE
C 252 IF (X3-X2(K)) 253,254
C 253 GO TO 255
C 254 CONTINUE
C 255 IF (X3.GT.X2(K-1)) 256,257
C 256 GO TO 258
C 257 CONTINUE
C 258 IF (X3-X2(K)) 259,260
C 259 GO TO 261
C 260 CONTINUE
C 261 IF (X3.GT.X2(K-1)) 262,263
C 262 GO TO 264
C 263 CONTINUE
C 264 IF (X3-X2(K)) 265,266
C 265 GO TO 267
C 266 CONTINUE
C 267 IF (X3.GT.X2(K-1)) 268,269
C 268 GO TO 270
C 269 CONTINUE
C 270 IF (X3-X2(K)) 271,272
C 271 GO TO 273
C 272 CONTINUE
C 273 IF (X3.GT.X2(K-1)) 274,275
C 274 GO TO 276
C 275 CONTINUE
C 276 IF (X3-X2(K)) 277,278
C 277 GO TO 279
C 278 CONTINUE
C 279 IF (X3.GT.X2(K-1)) 280,281
C 280 GO TO 282
C 281 CONTINUE
C 282 IF (X3-X2(K)) 283,284
C 283 GO TO 285
C 284 CONTINUE
C 285 IF (X3.GT.X2(K-1)) 286,287
C 286 GO TO 288
C 287 CONTINUE
C 288 IF (X3-X2(K)) 289,290
C 289 GO TO 291
C 290 CONTINUE
C 291 IF (X3.GT.X2(K-1)) 292,293
C 292 GO TO 294
C 293 CONTINUE
C 294 IF (X3-X2(K)) 295,296
C 295 GO TO 297
C 296 CONTINUE
C 297 IF (X3.GT.X2(K-1)) 298,299
C 298 GO TO 300
C 299 CONTINUE
C 300 IF (X3-X2(K)) 301,302
C 301 GO TO 303
C 302 CONTINUE
C 303 IF (X3.GT.X2(K-1)) 304,305
C 304 GO TO 306
C 305 CONTINUE
C 306 IF (X3-X2(K)) 307,308
C 307 GO TO 309
C 308 CONTINUE
C 309 IF (X3.GT.X2(K-1)) 310,311
C 310 GO TO 312
C 311 CONTINUE
C 312 IF (X3-X2(K)) 313,314
C 313 GO TO 315
C 314 CONTINUE
C 315 IF (X3.GT.X2(K-1)) 316,317
C 316 GO TO 318
C 317 CONTINUE
C 318 IF (X3-X2(K)) 319,320
C 319 GO TO 321
C 320 CONTINUE
C 321 IF (X3.GT.X2(K-1)) 322,323
C 322 GO TO 324
C 323 CONTINUE
C 324 IF (X3-X2(K)) 325,326
C 325 GO TO 327
C 326 CONTINUE
C 327 IF (X3.GT.X2(K-1)) 328,329
C 328 GO TO 330
C 329 CONTINUE
C 330 IF (X3-X2(K)) 331,332
C 331 GO TO 333
C 332 CONTINUE
C 333 IF (X3.GT.X2(K-1)) 334,335
C 334 GO TO 336
C 335 CONTINUE
C 336 IF (X3-X2(K)) 337,338
C 337 GO TO 339
C 338 CONTINUE
C 339 IF (X3.GT.X2(K-1)) 340,341
C 340 GO TO 342
C 341 CONTINUE
C 342 IF (X3-X2(K)) 343,344
C 343 GO TO 345
C 344 CONTINUE
C 345 IF (X3.GT.X2(K-1)) 346,347
C 346 GO TO 348
C 347 CONTINUE
C 348 IF (X3-X2(K)) 349,350
C 349 GO TO 351
C 350 CONTINUE
C 351 IF (X3.GT.X2(K-1)) 352,353
C 352 GO TO 354
C 353 CONTINUE
C 354 IF (X3-X2(K)) 355,356
C 355 GO TO 357
C 356 CONTINUE
C 357 IF (X3.GT.X2(K-1)) 358,359
C 358 GO TO 360
C 359 CONTINUE
C 360 IF (X3-X2(K)) 361,362
C 361 GO TO 363
C 362 CONTINUE
C 363 IF (X3.GT.X2(K-1)) 364,365
C 364 GO TO 366
C 365 CONTINUE
C 366 IF (X3-X2(K)) 367,368
C 367 GO TO 369
C 368 CONTINUE
C 369 IF (X3.GT.X2(K-1)) 370,371
C 370 GO TO 372
C 371 CONTINUE
C 372 IF (X3-X2(K)) 373,374
C 373 GO TO 375
C 374 CONTINUE
C 375 IF (X3.GT.X2(K-1)) 376,377
C 376 GO TO 378
C 377 CONTINUE
C 378 IF (X3-X2(K)) 379,380
C 379 GO TO 381
C 380 CONTINUE
C 381 IF (X3.GT.X2(K-1)) 382,383
C 382 GO TO 384
C 383 CONTINUE
C 384 IF (X3-X2(K)) 385,386
C 385 GO TO 387
C 386 CONTINUE
C 387 IF (X3.GT.X2(K-1)) 388,389
C 388 GO TO 390
C 389 CONTINUE
C 390 IF (X3-X2(K)) 391,392
C 391 GO TO 393
C 392 CONTINUE
C 393 IF (X3.GT.X2(K-1)) 394,395
C 394 GO TO 396
C 395 CONTINUE
C 396 IF (X3-X2(K)) 397,398
C 397 GO TO 399
C 398 CONTINUE
C 399 IF (X3.GT.X2(K-1)) 400,401
C 400 GO TO 402
C 401 CONTINUE
C 402 IF (X3-X2(K)) 403,404
C 403 GO TO 405
C 404 CONTINUE
C 405 IF (X3.GT.X2(K-1)) 406,407
C 406 GO TO 408
C 407 CONTINUE
C 408 IF (X3-X2(K)) 409,410
C 409 GO TO 411
C 410 CONTINUE
C 411 IF (X3.GT.X2(K-1)) 412,413
C 412 GO TO 414
C 413 CONTINUE
C 414 IF (X3-X2(K)) 415,416
C 415 GO TO 417
C 416 CONTINUE
C 417 IF (X3.GT.X2(K-1)) 418,419
C 418 GO TO 420
C 419 CONTINUE
C 420 IF (X3-X2(K)) 421,422
C 421 GO TO 423
C 422 CONTINUE
C 423 IF (X3.GT.X2(K-1)) 424,425
C 424 GO TO 426
C 425 CONTINUE
C 426 IF (X3-X2(K)) 427,428
C 427 GO TO 429
C 428 CONTINUE
C 429 IF (X3.GT.X2(K-1)) 430,431
C 430 GO TO 432
C 431 CONTINUE
C 432 IF (X3-X2(K)) 433,434
C 433 GO TO 435
C 434 CONTINUE
C 435 IF (X3.GT.X2(K-1)) 436,437
C 436 GO TO 438
C 437 CONTINUE
C 438 IF (X3-X2(K)) 439,440
C 439 GO TO 441
C 440 CONTINUE
C 441 IF (X3.GT.X2(K-1)) 442,443
C 442 GO TO 444
C 443 CONTINUE
C 444 IF (X3-X2(K)) 445,446
C 445 GO TO 447
C 446 CONTINUE
C 447 IF (X3.GT.X2(K-1)) 448,449
C 448 GO TO 450
C 449 CONTINUE
C 450 IF (X3-X2(K)) 451,452
C 451 GO TO 453
C 452 CONTINUE
C 453 IF (X3.GT.X2(K-1)) 454,455
C 454 GO TO 456
C 455 CONTINUE
C 456 IF (X3-X2(K)) 457,458
C 457 GO TO 459
C 458 CONTINUE
C 459 IF (X3.GT.X2(K-1)) 460,461
C 460 GO TO 462
C 461 CONTINUE
C 462 IF (X3-X2(K)) 463,464
C 463 GO TO 465
C 464 CONTINUE
C 465 IF (X3.GT.X2(K-1)) 466,467
C 466 GO TO 468
C 467 CONTINUE
C 468 IF (X3-X2(K)) 469,470
C 469 GO TO 471
C 470 CONTINUE
C 471 IF (X3.GT.X2(K-1)) 472,473
C 472 GO TO 474
C 473 CONTINUE
C 474 IF (X3-X2(K)) 475,476
C 475 GO TO 477
C 476 CONTINUE
C 477 IF (X3.GT.X2(K-1)) 478,479
C 478 GO TO 480
C 479 CONTINUE
C 480 IF (X3-X2(K)) 481,482
C 481 GO TO 483
C 482 CONTINUE
C 483 IF (X3.GT.X2(K-1)) 484,485
C 484 GO TO 486
C 485 CONTINUE
C 486 IF (X3-X2(K)) 487,488
C 487 GO TO 489
C 488 CONTINUE
C 489 IF (X3.GT.X2(K-1)) 490,491
C 490 GO TO 492
C 491 CONTINUE
C 492 IF (X3-X2(K)) 493,494
C 493 GO TO 495
C 494 CONTINUE
C 495 IF (X3.GT.X2(K-1)) 496,497
C 496 GO TO 498
C 497 CONTINUE
C 498 IF (X3-X2(K)) 499,500
C 499 GO TO 501
C 500 CONTINUE
C 501 IF (X3.GT.X2(K-1)) 502,503
C 502 GO TO 504
C 503 CONTINUE
C 504 IF (X3-X2(K)) 505,506
C 505 GO TO 507
C 506 CONTINUE
C 507 IF (X3.GT.X2(K-1)) 508,509
C 508 GO TO 510
C 509 CONTINUE
C 510 IF (X3-X2(K)) 511,512
C 511 GO TO 513
C 512 CONTINUE
C 513 IF (X3.GT.X2(K-1)) 514,515
C 514 GO TO 516
C 515 CONTINUE
C 516 IF (X3-X2(K)) 517,518
C 517 GO TO 519
C 518 CONTINUE
C 519 IF (X3.GT.X2(K-1)) 520,521
C 520 GO TO 522
C 521 CONTINUE
C 522 IF (X3-X2(K)) 523,524
C 523 GO TO 525
C 524 CONTINUE
C 525 IF (X3.GT.X2(K-1)) 526,527
C 526 GO TO 528
C 527 CONTINUE
C 528 IF (X3-X2(K)) 529,530
C 529 GO TO 531
C 530 CONTINUE
C 531 IF (X3.GT.X2(K-1)) 532,533
C 532 GO TO 534
C 533 CONTINUE
C 534 IF (X3-X2(K)) 535,536
C 535 GO TO 537
C 536 CONTINUE
C 537 IF (X3.GT.X2(K-1)) 538,539
C 538 GO TO 540
C 539 CONTINUE
C 540 IF (X3-X2(K)) 541,542
C 541 GO TO 543
C 542 CONTINUE
C 543 IF (X3.GT.X2(K-1)) 544,545
C 544 GO TO 546
C 545 CONTINUE
C 546 IF (X3-X2(K)) 547,548
C 547 GO TO 549
C 548 CONTINUE
C 549 IF (X3.GT.X2(K-1)) 550,551
C 550 GO TO 552
C 551 CONTINUE
C 552 IF (X3-X2(K)) 553,554
C 553 GO TO 555
C 554 CONTINUE
C 555 IF (X3.GT.X2(K-1)) 556,557
C 556 GO TO 558
C 557 CONTINUE
C 558 IF (X3-X2(K)) 559,560
C 559 GO TO 561
C 560 CONTINUE
C 561 IF (X3.GT.X2(K-1)) 562,563
C 562 GO TO 564
C 563 CONTINUE
C 564 IF (X3-X2(K)) 565,566
C 565 GO TO 567
C 566 CONTINUE
C 567 IF (X3.GT.X2(K-1)) 568,569
C 568 GO TO 570
C 569 CONTINUE
C 570 IF (X3-X2(K)) 571,572
C 571 GO TO 573
C 572 CONTINUE
C 573 IF (X3.GT.X2(K-1)) 574,575
C 574 GO TO 576
C 575 CONTINUE
C 576 IF (X3-X2(K)) 577,578
C 577 GO TO 579
C 578 CONTINUE
C 579 IF (X3.GT.X2(K-1)) 580,581
C 580 GO TO 582
C 581 CONTINUE
C 582 IF (X3-X2(K)) 583,584
C 583 GO TO 585
C 584 CONTINUE
C 585 IF (X3.GT.X2(K-1)) 586,587
C 586 GO TO 588
C 587 CONTINUE
C 588 IF (X3-X2(K)) 589,590
C 589 GO TO 591
C 590 CONTINUE
C 591 IF (X3.GT.X2(K-1)) 592,593
C 592 GO TO 594
C 593 CONTINUE
C 594 IF (X3-X2(K)) 595,596
C 595 GO TO 597
C 596 CONTINUE
C 597 IF (X3.GT.X2(K-1)) 598,599
C 598 GO TO 600
C 599 CONTINUE
C 600 IF (X3-X2(K)) 601,602
C 601 GO TO 603
C 602 CONTINUE
C 603 IF (X3.GT.X2(K-1)) 604,605
C 604 GO TO 606
C 605 CONTINUE
C 606 IF (X3-X2(K)) 607,608
C 607 GO TO 609
C 608 CONTINUE
C 609 IF (X3.GT.X2(K-1)) 610,611
C 610 GO TO 612
C 611 CONTINUE
C 612 IF (X3-X2(K)) 613,614
C 613 GO TO 615
C 614 CONTINUE
C 615 IF (X3.GT.X2(K-1)) 616,617
C 616 GO TO 618
C 617 CONTINUE
C 618 IF (X3-X2(K)) 619,620
C 619 GO TO 621
C 620 CONTINUE
C 621 IF (X3.GT.X2(K-1)) 622,623
C 622 GO TO 624
C 623 CONTINUE
C 624 IF (X3-X2(K)) 625,626
C 625 GO TO 627
C 626 CONTINUE
C 627 IF (X3.GT.X2(K-1)) 628,629
C 628 GO TO 630
C 629 CONTINUE
C 630 IF (X3-X2(K)) 631,632
C 631 GO TO 633
C 632 CONTINUE
C 633 IF (X3.GT.X2(K-1)) 634,635
C 634 GO TO 636
C 635 CONTINUE
C 636 IF (X3-X2(K)) 637,638
C 637 GO TO 639
C 638 CONTINUE
C 639 IF (X3.GT.X2(K-1)) 640,641
C 640 GO TO 642
C 641 CONTINUE
C 642 IF (X3-X2(K)) 643,644
C 643 GO TO 645
C 644 CONTINUE
C 645 IF (X3.GT.X2(K-1)) 646,647
C 646 GO TO 648
C 647 CONTINUE
C 648 IF (X3-X2(K)) 649,650
C 649 GO TO 651
C 650 CONTINUE
C 651 IF (X3.GT.X2(K-1)) 652,653
C 652 GO TO 654
C 653 CONTINUE
C 654 IF (X3-X2(K)) 655,656
C 655 GO TO 657
C 656 CONTINUE
C 657 IF (X3.GT.X2(K-1)) 658,659
C 658 GO TO 660
C 659 CONTINUE
C 660 IF (X3-X2(K)) 661,662
C 661 GO TO 663
C 662 CONTINUE
C 663 IF (X3.GT.X2(K-1)) 664,665
C 664 GO TO 666
C 665 CONTINUE
C 666 IF (X3-X2(K)) 667,668
C 667 GO TO 669
C 668 CONTINUE
C 669 IF (X3.GT.X2(K-1)) 670,671
C 670 GO TO 672
C 671 CONTINUE
C 672 IF (X3-X2(K)) 673,674
C 673 GO TO 675
C 674 CONTINUE
C 675 IF (X3.GT.X2(K-1)) 676,677
C 676 GO TO 678
C 677 CONTINUE
C 678 IF (X3-X2(K)) 679,680
C 679 GO TO 681
C 680 CONTINUE
C 681 IF (X3.GT.X2(K-1)) 682,683
C 682 GO TO 684
C 683 CONTINUE
C 684 IF (X3-X2(K)) 685,686
C 685 GO TO 687
C 686 CONTINUE
C 687 IF (X3.GT.X2(K-1)) 688,689
C 688 GO TO 690
C 689 CONTINUE
C 690 IF (X3-X2(K)) 691,692
C 691 GO TO 693
C 692 CONTINUE
C 693 IF (X3.GT.X2(K-1)) 694,695
C 694 GO TO 696
C 695 CONTINUE
C 696 IF (X3-X2(K)) 697,698
C 697 GO TO 699
C 698 CONTINUE
C 699 IF (X3.GT.X2(K-1)) 700,701
C 700 GO TO 702
C 701 CONTINUE
C 702 IF (X3-X2(K)) 703,704
C 703 GO TO 705
C 704 CONTINUE
C 705 IF (X3.GT.X2(K-1)) 706,707
C 706 GO TO 708
C 707 CONTINUE
C 708 IF (X3-X2(K)) 709,710
C 709 GO TO 711
C 710 CONTINUE
C 711 IF (X3.GT.X2(K-1)) 712,713
C 712 GO TO 714
C 713 CONTINUE
C 714 IF (X3-X2(K)) 715,716
C 715 GO TO 717
C 716 CONTINUE
C 717 IF (X3.GT.X2(K-1)) 718,719
C 718 GO TO 720
C 719 CONTINUE
C 720 IF (X3-X2(K)) 721,722
C 721 GO TO 723
C 722 CONTINUE
C 723 IF (X3.GT.X2(K-1)) 724,725
C 724 GO TO 726
C 725 CONTINUE
C 726 IF (X3-X2(K)) 727,728
C 727 GO TO 729
C 728 CONTINUE
C 729 IF (X3.GT.X2(K-1)) 730,731
C 730 GO TO 732
C 731 CONTINUE
C 732 IF (X3-X2(K)) 733,734
C 733 GO TO 735
C 734 CONTINUE
C 735 IF (X3.GT.X2(K-1)) 736,737
C 736 GO TO 738
C 737 CONTINUE
C 738 IF (X3-X2(K)) 739,740
C 739 GO TO 741
C 740 CONTINUE
C 741 IF (X3.GT.X2(K-1)) 742,743
C 742 GO TO 744
C 743 CONTINUE
C 744 IF (X3-X2(K)) 745,746
C 745 GO TO 747
C 746 CONTINUE
C 747 IF (X3.GT.X2(K-1)) 748,749
C 748 GO TO 750
C 749 CONTINUE
C 750 IF (X3-X2(K)) 751,752
C 751 GO TO 753
C 752 CONTINUE
C 753 IF (X3.GT.X2(K-1)) 754,755
C 754 GO TO 756
C 755 CONTINUE
C 756 IF (X3-X2(K)) 757,758
C 757 GO TO 759
C 758 CONTINUE
C 759 IF (X3.GT.X2(K-1)) 760,761
C 760 GO TO 762
C 761 CONTINUE
C 762 IF (X3-X2(K)) 763,764
C 763 GO TO 765
C 764 CONTINUE
C 765 IF (X3.GT.X2(K-1)) 766,767
C 766 GO TO 768
C 767 CONTINUE
C 768 IF (X3-X2(K)) 769,770
C 769 GO TO 771
C 770 CONTINUE
C 771 IF (X3.GT.X2(K-1)) 772,773
C 772 GO TO 774
C 773 CONTINUE
C 774 IF (X3-X2(K)) 775,776
C 775 GO TO 777
C 776 CONTINUE
C 777 IF (X3.GT.X2(K-1)) 778,779
C 778 GO TO 780
C 779 CONTINUE
C 780 IF (X3-X2(K)) 781,782
C 781 GO TO 783
C 782 CONTINUE
C 783 IF (X3.GT.X2(K-1)) 784,785
C 784 GO TO 786
C 785 CONTINUE
C 786 IF (X3-X2(K)) 787,788
C 787 GO TO 789
C 788 CONTINUE
C 789 IF (X3.GT.X2(K-1)) 790,791
C 790 GO TO 792
C 7
```

```

315 GO TO 314
      K=K+1
      GO TO 311
C 316 CONTINUE
      IF (IND1*EQ.1*CR*IND2*EC.1*GR*IND3*EQ.1) GO TO 414
      CCOEF1=(XA-XA(1-1))/((X1(1)-X1(1-1))
      VP=Y(1-1,J,K)+(Y(1,J,K)-Y(1-1,J,K))*CCOEF1
      VMPE=Y(1-1,J-1,K)+(Y(1,J-1,K)-Y(1-1,J-1,K))*CCOEF1
      VNM=Y(1-1,J,K-1)+(Y(1,J,K-1)-Y(1-1,J,K-1))*CCOEF1
      VMV=Y(1-1,J-1,K-1)+(Y(1,J-1,K-1)-Y(1-1,J-1,K-1))*CCOEF1
C 51 COEF2=(X2-X2(1-1))/(X2(1)-X2(1-1))
      VP=VMF+(VP-VNM)*CCOEF2
      VN=VM+(VM-VNM)*CCOEF2
C 52 COEF3=(X3-X3(1-1))/(X3(1)-X3(1-1))
      TRITRP=VM+(VM-VM)*CCOEF3
      RETURN
C 14 IND1=1
      GO TO 316
214 IND2=1
      GO TO 216
314 IND3=1
      GO TO 316
414 CONTINUE
      PRINT 100,IND1,IND2,IND3
100 FORMAT(7H TRITRP,3I10)
      IF (IND1*EC.0) GC TO 50
      IF (IND2*EQ.0) GO TO 51
      IF (IND3*EQ.0) GO TO 52
      IND1=1,IND2=1,IND3=1
      TRITRP=Y(1,J,K)
      RETURN
C 52 CONTINUE
C  IND1=1, IND2=1, IND3=0
      VP=Y(1,J,K)
      VM=Y(1,J,K-1)
      GO TO 62
52 IF (IND3*EC.0) GO TO 53
      IND1=1, IND2=1, IND3=1
      CCOEF2=(X3-X2(1-1))/(X2(1)-X2(1-1))
      VP=Y(1,J,K)
      VM=Y(1,J-1,K)
      TRITRP=VM+(VP-VNM)*CCOEF2
      RETURN
52 CONTINUE
C  IND1=1, IND2=2, IND3=0
      VP=Y(1,J,K)
      VM=Y(1,J-1,K)
      VM=VM+(Y(1,J,K-1)-Y(1,J-1,K-1))
      VM=Y(1,J-1,K-1)
      GO TO 61

```

BEST AVAILABLE COPY

```

50  IF(IND2•E2•2) GO TO 54
C  IND1=0,IND2=1,IND3=0
C  IF(IND3•E2•0) GO TO 55
C  COEF1=(XA-X2)(I-1)/(X1(I)-X1(I-1))
VM = Y(I-1,J,K)
VP = Y(I,J,K)
TRITRP=VM+(VP-VM) * COEF1
RETURN
55  CUNTINUE
C  IND1=0,IND2=1,IND3=0
COEF1=(XA-X1(I-1))/(X1(I)-X1(I-1))
VP = Y(I-1,J,K)+(Y(I,J,K)-Y(I-1,J,K))* COEF1
VM = Y(I-1,J,K-1)+(Y(I,J,K-1)-Y(I-1,J,K-1))* COEF1
GO TO 62
54  IF(IND3•E2•2) GO TO 63
C  IND1=0,IND2=0,IND3=1
COEF1=(XA-X1(I-1))/(X1(I)-X1(I-1))
VP = Y(I-1,J,K)+(Y(I,J,K)-Y(I-1,J,K))* COEF1
VM = Y(I-1,J-1,K)+(Y(I,J-1,K)-Y(I-1,J-1,K))* COEF1
COEF2=(X2-X2(J-1))/(X2(J)-X2(J-1))
TRITRP=VM+(VP-VM) * COEF2
C
RETURN
END

```

FIGURE C-2 (Continued)

PCT AVAILABLE COPY

```

SUBROUTINE SR1250(HMF1,HMF2,FOE,FOT1,FOT2,YA,FF,HTLHTW)
C
C 131 VERSION OF FACEFILE PROGRAM BY ELAINE MATFIELD. 13 SEP 1977
C COMPUTES THE VERTICAL ELECTION DENSITY(PLAGMA FREQUENCY) PROFILE.
C AT EACH STATION (TH,PH) UPTO A MAX. SPECIFIED HEIGHT + AT
C UNIFORM INCREMENTS.
C LAST MODIFICATION 1C/2E/77
C
C
C 14 CONTINUE
FNE=1.24*1000C.*FOE**2
YMF2=YM**2.
YEUP=C.0
ENF1=1.24*1000C.*FCF1**2
ENF2=1.24*1000C.*FCF2**2
FVAL1=1.24*10000.*FOV1**2
FVAL2=1.24*10000.*FOV2**2
C
C***** TOPSIDE
CALL TOPSID(YM,HMF2,ZCHT,A2S2,AT/C,S2,EDZC,FNF2)
C
C
HMN=0.0
YE=25.
YE2=YE*1.4142
YC=1.4142*YM
HMIN=14C.C
IF(FOE.GT.C.1) GO TO 110
SINGLE F2 LAYER
IF((HMF2-1.3*YM).LT.HMIN) YC=0.91925*(HMF2-HMIN)
NPROF=1
GU=1.250
C
C 110 CONTINUE
C
C CHECK FOR VALLEY PREDICTIONS
IF(HVAL1.LT.1.0) GO TO 111
COMPUTE SCALE FOR CHAPMAN LAYER ABOVE E MAX
H=HVAL1
FN=FNF2
H=HMF2
AH=1.
Y=YM2
IF(FOE.1.EQ.0.0) GO TO 12

```

BEST AVAILABLE COPY

FIGURE C-2 (Continued)

```

12 CONTINUE
E1=VAL1-CHAPMN(FN,HH,YH,AH,VAL1) /2.
Y1=(E1-LT.C.2) E1=5.CE+3
HME=HME
EM=FNE
YEUP=(H1-HM)/ALOG(CL/EL)
CONTINUE
13 IF(HVAL2.LT.1.AND.CF1.EQ.0.) GO TO 400
C TWO VALLEY 11
C NPROF=5
GO TO 200
CONTINUE
C ONE VALLEY
C NPROF=5
GO TO 200
112 CONTINUE
C EXPONENTIAL PROFILE
C NPROF=7
H1=4*MF2-YMF2/2.
E1=MF2-CHAPMN(FMF2,HMF2,YMF2,1.0*H1)
HME=HME
EM=FNE
YEUP=(H1-HM)/ALOG(EM/E1)
GO TO 200
CONTINUE
15
C EXPONENTIAL PROFILE WITH F1 LAYER
C NPROF=9
C CHANGED FROM 4. TU 3. TO ELIMINATE UN-PREDICTED VALLEY
C H1=HMF1-(HMF1-HME)/4.
C H1=HMF1-(HMF1-HME)/3.
C E1=FNF1-C, AND FN(FN1,HMF1-(HMF1-HME)/2000.5,H1)
HME=HME
EM=FNE
YEUP=(H1-HM)/ALOG(EM/F1)
201 CONTINUE
1F(FOF1.GT.3.1) GO TO 160
111 CONTINUE
C NU F1 LAYER
C IF(FOF2.LT.FOE) GO TO 112
C IF(FOE.LT.FOF2) GO TO 120
C IF(HME.LT.(1MF2-YC)) GO TO 140
C FEP=PROF3(1.0*0.2*HMF2,HME,YC)
C FEP=SQRT(FEP)*FOF2
C IF(FEP.LT.F2E) GO TO 140
C CONTINUE
120
C TWO LAYER PROFILE
C NPROF=2
YC1=HMF2 - HME

```

BEST AVAILABLE COPY

FIGURE C-2 (Continued)

14C CONTINUE
 C THREE LAYER HCN-CONTINUE PRHF 1L-
 C NPFUF=3
 14C CONTINUE
 YC=1.4142*YM
 IF(FNF1.LT.FNF2)
 1AA=SQRT(1.0-FNE*FNF2)
 IF(FNF2.LT.FNE) 301 307
 GG=AA
 HFE=HMF2-AA*YC
 YC1=HFF-HMF
 AA=2.0*FNF2*AA*YC
 FNE=FE-4.0*AA*YC1/27.0
 HMN=HMF+2.0*HFE)/3.0
 IF(HMN-HME.LT.10.0.AND.FCF1.LT.0.1) GO TO 120
 IF(FNM.GE.0.0) GU TU 150
 FNET=FNE
 FNE=0.35004392*FNE
 YP=9.0*C*FNF2*GC*(HMF2-HME)/(27.0*FNE+4.0*GG*GG*FNF2)
 YCEYS
 FNE=FFNET
 Y4=YC/1.0+14.2
 GU TU 145
 GO TU 200
 160 CONTINUE
 IF(FNE.GT.FNF2.AND.FNE.GT.FNF1) GO TO 15
 C THREE LAYER CCFFILE E.F1.F2
 NPFUF=4
 YC=HMF2-HMF1
 YC1=HNF1-HME
 IF(FNF1.GT.FNE.AND.FNF1.GT.FNF2) GO TO 200
 C IF CHATINIKA VALLEYS ARE NOT USED USE CHATNIKA VALLEY
 IF(NUCHAT.EQ.1.AND.FOF1.LT.FOE.AND.YC.LT.YM) GU TO 140
 C IF F1 IS TOO HIGH IGNORE IT
 C USE 2.0 LAYER CCFFILE
 C IF(YC.LT.YM) GU TO 120
 C IF((HVAL2.GT.C.0.YR.YC1.GT.3.*YE).AND.FNF1.LT.FNE.AND.NOCHAT.EQ.0)
 1 GO TO 15
 IF(FNF1.LT.5.0E+3) FNF1=5.0E+3
 C 200 CONTINUE
 PRINT 1,FCV1,F0V2,F0E,F0F1,F0F2,YM,HME,IMF1,HMF2,YE,NPFUF,PHM,THM.
 1 HMT,HVAL1,HVAL2
 1 FDMAT(1X,2F6.1,3F9.0,2,14,4X,2F7.1,3F5.0,1)
 1 DD 95 1=1,LHTMX
 H=GT(I)
 C ABOVE F2 MAX
 IF(H.GT.HMF2) GU TO 42

FIGURE C-2 (Continued)

BEST AVAILABLE COPY

ELAH 341

ELAH 341

```

C      SELVA E LAYER
C      !F(H•GT•(HME-YE2)) GU TO 201
C      FD=5•C
C
C      201 CONTINUE
C
C      JEL JNE MAX
C      IF(H•GT•HME) GO TU 202
C      IF(NPROF•TU•1) GO TU 202
C      ED=CHARPN(FNE•HME•YE••5•H)
C      GO TU 90
C
C      202 CONTINUE
C
C      GO TU (21C•26C•31C•36C •41C•42C•43C•44C)•NPROF
C
C      NPROF=1
C
C      21C CONTINUE
C      IF(H•GT•(HMF2-YC)) GC TC 22C
C      ED=0•C
C      GO TU 90
C
C      22C CONTINUE
C      ED=FNF2*PROF3(1.0•3•C,HMF2•H,YC)
C      GJ TU 90
C
C      NPROF=2
C
C      26C CONTINUE
C      ED=PROF3(FNF2•FNE•HMF2•H,YC1)
C      GO TU 90
C
C      NPROF=3
C
C      31C CONTINUE
C      IF(H•LT•HFE) GC TC 33C
C      ED=PARAB(FNF2•HMF2•YC•H)
C      GO TU 90
C
C      33C CONTINUE
C      HP=H - HME
C      ED=FNE + AA*HP**3/YC1**2 - AA*HP*HP/YC1
C      IF(ED•LT•0•C) ED=124•C
C      GO TU 90
C
C      NPROF=4
C
C      36C CONTINUE
C      IF(H•GT•HMF1) GU TC 39C
C      ED=PROF3(FNF1•FNE•HMF1•H,YC1)
C      GO TU 90
C
C      39C IF(HVAL2•GT•0•0) GC TU 424
C      ED=PROF3(FNF2•FNF1•HMF2•H,YC)
C      GO TU 90
C
C      NPROF=5
C
C      41C CONTINUE
C      IF(H•GT•HVAL1•AND•HMF2-HVAL1•GT•YMF2) GU TO 411
C      WT=(HMF2-H)/(YMF2-H1)
C      IF(WT•GT•1.) WT=1.

```

FIGURE C-2 (Continued)

ELAH 451
ELAH 453

```

ED=EXPUN(FNE,FMF,YEU,WT+CHAPMN(FNF2,1MF2,100H)*(10-NT/2))
50 TO 50
50 ED=PROF3(FNF2,FVAL1,HMF2,WT+HVAL1)
50 TO 90

C 411 NPQDF=5
      CONTINUE
      IF(H,GT,HMF1) GO TO 424
      WT=(HMF1-H)/(HMF1-H1)
      IF(T,GT,1) WT=1
      ED=EXPUN(FNE,WT+YEU,WT+CHAPMN(FNF1,HMF1,(HMF1-HAE)/2000.5,WT))
      1*(1-WT/2.)
      GO TO 90

424 IF(HVAL2,GT,2) GO TO 390
      IF(H,GT,HVAL2) GO TO 425
      ED=PROF3(FVAL2,FNF1,HVAL2,WT+HVAL2-HMF1)
      50 TO 50
      ED=PROF3(FNF2,FVAL2,HMF2,WT+HVAL2)
      GO TO 90

C 425 NPQDF=7
      CONTINUE
      WT=(HMF2-H)/(HMF2-H1)
      IF(WT,GT,1) WT=1
      ED=EXPUN(FNE,WT+YEU,WT+CHAPMN(FNF2,HMF2,100H))
      GO TO 90

C 430 NPQDF=6
      CONTINUE
      IF(H,GT,HMF1) GO TO 443
      WT=(HMF1-H)/(HMF1-H1)
      IF(WT,GT,1) WT=1
      ED=EXPUN(FNE,WT+YEU,WT+CHAPMN(FNF1,HMF1,(HMF1-HAE)/2000.5,WT))
      GO TO 90

443 CONTINUE
      VALLEY BETWEEN F1 AND F2 ONLY
      IF(HVAL2,GT,2) GO TO 424
      ED=PROF3(FNF2,FNF1,HMF2,WT+HMF1)
      GO TO 90

C 450 NPQDF=7
      CONTINUE
      IF(ZCHT,GT,HMF2) GO TO 50
      PRINT 45, ZCHT,HMF2
      FORMAT(7*,ND) TOPSIDE PROFILE ZCHT = *,F11.3,* HMF2 = *,F11.3,*
      GO TO 96

C 50 TOPSIDE CHAPMAN FIT.
      IF(H,GT,ZCHT) GO TO 55
      ED=CHAPMN(FNF2,HMF2,WT*200.1,WT)
      GO TO 90
      55 CONTINUE
      62 CONTINUE
      C*** TOPSIDE MODEL

```

BEST AVAILABLE COPY

FIGURE C-2 (Continued)

```

AT1=ATAN (A232*H)
AT2=ATAN (-S2*(AT1-AT2C))
C
C 90 CONTINUE
C
C 91 IF (ED.GT.C.) GO TO 91
C
C 97 CONTINUE
C
C FQ=0.
C
C ED=C.C
C
C 92 FQ=0.0C9998C255*SQRT(ED)
C
C 93 FGRD IS PLASMA FREQUENCY
C
C 94 FGRD(MLT,I)=FG
C
C 95 FF IS ELECTRON DENSITY
C
C 96 FOR IAT(7H) SRFRC,10E1C,10E1C,3)
C
C 97 FF(1)=ED
C
C 98 CONTINUE
C
C 99 RETURN
C
C END

```

FIGURE C-2 (Continued)

BEST AVAILABLE COPY

```

SUBROUTINE SHISCRP ( TT,ELAMDA,TH,AM,Q1,QID,Q1S )
C
C   T = CORRECTED GEOMAGNETIC TIME ( HOURS )
C   ELAMDA = CORRECTED GEOMAGNETIC LATITUDE ( DEGREES )
C   TH = CORRECTED GEOMAGNETIC LONGITUDE ( DEGREES )
C   RSN = SUN SPOT NUMBER
C   MU = MONTH
C   AKP=KP INDEX

C
C   DIMENSION SDEC(112)
C   COMMON/ABSRB/RSN,MO,FREQ,AKP
C   DATA R2D,D2R/57.2957796,0.0174532925/
C   DATA SDEC/-21.0,-13.0,-2.0,18.0,23.0,22.0,14.0,3.0,-3.0,-18.0,-23.0/
C   IF(C10C.LE.0.02) C10=0.02
C   IF(KP=12C.-23.0)*(5.0.-AKP)
C   IF(AKP.GT.5.0) RKP=200.-80.0*(6.0.-AKP)
C   ELAMSM=68.0*(1.0-C.0004*RKP)
C   1.870823=SQRT(3.5)
C   SIGLAM=3.0*C*(1.0+0.004*RKP)
C   DL=EXP(-(ELAMDA-ELAMSM)*(ELAMDA-ELAMSM)/2.0/SIGLAM/SIGLAM)
C   TM=10.0*(1.0-0.002*RKP)
C   T1=T
C   IF(T.GT.TM+12.0)T1=T-24.0
C   DSCALE=21.
C   DT=EXP(-(T1-TM)*(T1-TM)/15.7)
C   DTH=0.16
C   IF(TH.LT.10.0) DTH=C.58-0.42*SIN(0.947*D2R*(TH+85.0))
C   IF(TH.GT.80.0) AND(TH.LT.180.0) DTH=0.53+0.42*SIN(1.8*D2R*(TH-130.0))
C   IF(TH.GE.180.0) DTH=0.58-0.42*SIN(0.947*D2R*(TH-275.0))
C   DR=1.0+0.014*RSN
C   DN=1.0-0.3*SIN(3.86*D2R*SDEC(MO))
C   ADSKP=.174*14*AKP
C   Q1D=DL*DT*DR*DTH*DMSCALE
C   TT=T-3.0
C   IF(T.GT.15.0) TT=T-27.0
C   ELAMSP=67.0*(1.0-0.0006*RKP)+0.3*(1.0+0.0112*RKP)*ABS(TT)
C   SSCALE=12.
C   SL=EXP(-(ELAMDA-ELAMSP)*(ELAMDA-ELAMSP)/2.0/SIGLAM/SIGLAM)
C   SR=1.0+0.009*RSN
C   T2=T+1.
C   IF(T.GT.11.0) T2=T-23.
C   ST=EXP(-T2*T2/15.7)
C   Q1S=SL*ST*SR*DTH*SSCALE
C   Q1=Q1D+Q1S
C
C   HARGREAVES TRANSFORMATION Q TO AM
C   IF(Q1.LE.10.)AM=(Q1/2200.)*((1./3.5)
C   IF(Q1.GT.10.)AM=((Q1+30.)/80.)*1.54/1.6057
C   1.6057 REPRESENTS A SHIFT OF FOPPIANOS CURVE TO THE LEFT TO
C   MATCH HARGREAVES RELATION
C   SCALED TO A PEAK FOR KP=2.6 SSN=120. WINTER 1.0765=.6/.34
C   FROM BASLER
C   SCALEKP=1.765
C   AM=SCALEKP*ADSKP*AM
C   ONE WAY VERTICAL ABSORPTION -- MEDIAN
C   VL30=AM

```

BEST AVAILABLE COPY

FIGURE C-2 (Continued)

```

C FV=FRE0*C100
C ELMANDREELAMDA/B20
C DIP=ATAN((2.0*TAN(ELMAMDA)))
C FL=GF*SIN(DIP)

C PHIN SET AT .33 BECAUSE E LAYER ABSORPTION IS CALCULATED ELSEWHERE
C SEE REFERENCE GEURGE AND BRADLEY TELECOMMUNICATIONS JOURNAL VOL 41 74
C REFERENCE .38
C PHIN=.38

C VLFF=VVL30*((30.0+FL)/(FV+FL))**2*PHIN
C DBA=VLFV/C100*((FV+FL)/(FREQ+FL))**2
C PRINT 100,DIST,TH,T,ELAMDA,FV,FL,AM,JI
C 10C FORMAT(7H,AURORA,E10.3,BH,6M4S,3E10.3,6H,FREQS,2E10.3,4H,AME,
C 10C 1E10.3,4H,Q1,E10.3)
C RETURN
C END

```

FIGURE C-2 (Continued)

BEST AVAILABLE COPY

```

C 2010, ELAINE HATFIELD, V.1.1, F.2, ZCHT, A2S2, ATZC, SZC, FDZC, FNFC2
C COMPUTE'S PARAMETERS NEEDED FOR THE TOPSIDE PROFILE
C 15 SEP 1977 BY ELAINE HATFIELD, SH I

COMMON/PRLP2/ AP, KP, R, SOLFX
COMMON/ZEF1/ GLONG, CLT, HRMT, SECCHI, THM
COMMON/MINDEX/NGP, XKP, MON, MDAY, MYR, JDAY, CGUY2
DIMENSION A(4), XR(3)

REAL KP
DATA PI/3.1415926536/

C DAY=JDAY

C..... TOPSIDE
C..... A2 = 3.14 * 1.0E-4
C..... S2 = 5.89 - 0.015 * THM / SECCHI
C..... 1 + 0.41 * CGUY2 * PI * (DAY+11.0) / 365.0 * SIN(CLT) - 0.14 * KP
C..... A2S2=A2*S2
C..... BETAA=1.0/A2S2
C..... GAMMA = BETA**2
C..... YB = 1.0E5*YM
C..... A(1) = 1.0
C..... A(2) = .25/A2
C..... A(3) = GAMMA
C..... A(4) = -0.025 * S2*BETA*YM**2
C..... CALL CUBIC(A, XR, X1)
C..... XR(3)
C..... ZCHT = ZC + HMF2
C..... SZC = (ZCHT - HNF2) / YM
C..... FDZC = FNFC2 * EXP((1.0 - ZC - EXP(-SZC)))
C..... ATZC=ATAN(A2S2*ZCHT)

C RETURN
C END

```

BEST AVAILABLE COPY

FIGURE C-2 (Concluded)

REFERENCES

Akasofu, S.-I. (1977), Physics of Magnetospheric Substorms, Reidel Publishing Co., Dordrecht, Holland.

Baron, M. J. (1974), "Electron Densities Within Aurorae and Other Auroral E-Region Characteristics," Radio Sci., Vol. 9, pp. 341-348.

Baron, M. J. (1977), "The Chatanika Radar System," in Radar Probing of the Auroral Plasma, p. 103, A. Brekke, ed., Scandinavian University Books, Oslo, Norway.

Basler, R. (1963), "Radio Wave Absorption in the Auroral Ionosphere," J. Geophys. Res., Vol. 68, No. 16, pp. 4665-4681.

CCIR, (1976), "Conclusions of the Interim Meeting of Study Group 6 (Ionospheric Propagation)," Doc. 6/177-E, Geneva, pp. 193-197 (16 February to 3 March 1976).

Cage, A. L. and E. J. Zawalick (1972), "A Discussion of the Geomagnetic Indices K_p and a_p , 1932 to 1971," AFCRL-72-0693, Air Force Cambridge Research Laboratories, L. G. Hanscom Field, Bedford, Massachusetts.

Davis, T. N. (1962), "The Morphology of the Auroral Displays of 1957-1958-2. Detailed analyses of Alaska data and analyses of high-latitude data," J. Geophys. Res., Vol. 67, p. 75.

Elkins, T. and C. Rush (1973), "A Statistical Predictive Model of the Polar Ionosphere," in An Empirical Model of the Polar Ionosphere, T. Elkins, ed., AFCRL-TR-73-0331, Air Force Cambridge Research Laboratories, L. G. Hanscom Field, Bedford, Massachusetts.

Evans, J. V. (1969), "Theory and Practice of Ionosphere Study by Thomson Scatter Radar," Proc. IEEE, Vol. 57, p. 496.

Foppiano, A. (1975), "A New Method for Predicting the Auroral Absorption of HF Sky Waves," CCIR, IWP 6/1, Docs. 3 and 10.

Hargreaves, J. (1966), "On the Variation of Auroral Absorption with Geomagnetic Activity," Planet Space Sci., Vol. 14, pp. 991-1006.

Hartz, T. (1972), "Morphology of Radio-Radar Polar Propagation Effects," AGARD Conference Proceedings No. 97 on Radar Absorption in the Arctic, pp. 1-18.

Hartz, T. R., and N. M. Brice (1967), "The General Pattern of Auroral Particle Precipitation," Planet Space Sci., Vol. 15, p. 301.

Leadabrand, R. L., M. J. Baron, J. Petriceks, and H. F. Bates (1972), "Chatanika, Alaska, Auroral-Zone Incoherent-Scatter Facility," Radio Sci., Vol. 7, pp. 747-756.

Liu, A. T. Y., P. Perreault, and S.-I. Akasofu (1973), "The Diffuse Aurora," Planet Space Sci., Vol. 21, p. 857.

Murphree, J. S. and C. D. Anger (1977), "Calculation of the Instantaneous Boundary of Auroral Emissions," EOS Trans. AGU, Vol. 58, p. 712.

Page, D. and M. Shaw (1972), "Diurnal, Seasonal, and K_p Variations in the Position of the High Latitude Electron Trapping Boundary," Space-Research XII, p. 1471, Akademie-Verlag, Berlin.

Piddington, J. H. (1965), "The Morphology of Auroral Precipitation," Planet Space Sci., Vol. 13, 565.

Rostoker, G. (1972), "Geomagnetic Indices," Rev. Geophys. Space Phys., Vol. 10, p. 935.

Toman, K. and D. Miller (1977a), "Computational Study of Long-Range High-Frequency Ionospheric Ducting," Radio Science, Vol. 12, p. 467.

Toman, K. and D. Miller (1977b), "On the Relative Efficiency and Stability of Ionospheric Ducting Channels," paper presented at URSI meeting, Stanford University, Stanford, California, 20-24 June 1977.

Vondrak, R. R. and M. J. Baron (1976), "Radar Measurements of the Latitudinal Variations of Auroral Ionization," Radio Sci., Vol. 11, p. 939.

Watt, T. M. (1973), "Incoherent Scatter Observations of the Ionosphere over Chatanika, Alaska," J. Geophys. Res., Vol. 78, p. 2992.

Wickwar, V. B. (1975), "Chatanika Radar Measurements," in Atmospheres of the Earth and the Planets, B. M. McCormac, ed., Reidel Publishing Co., Dordrecht, Holland.

MISSION
of
Rome Air Development Center

RADC plans and conducts research, exploratory and advanced development programs in command, control, and communications (C³) activities, and in the C³ areas of information sciences and intelligence. The principal technical mission areas are communications, electromagnetic guidance and control, surveillance of ground and aerospace objects, intelligence data collection and handling, information system technology, ionospheric propagation, solid state sciences, microwave physics and electronic reliability, maintainability and compatibility.